Physics of Particle Detection

Narongrit Ritjoho

School of Physics, Institute of Science,
Suranaree University of Technology

29.04.2023

Picture: https://home.cern/science/experiments/atlas

CERN-CMS

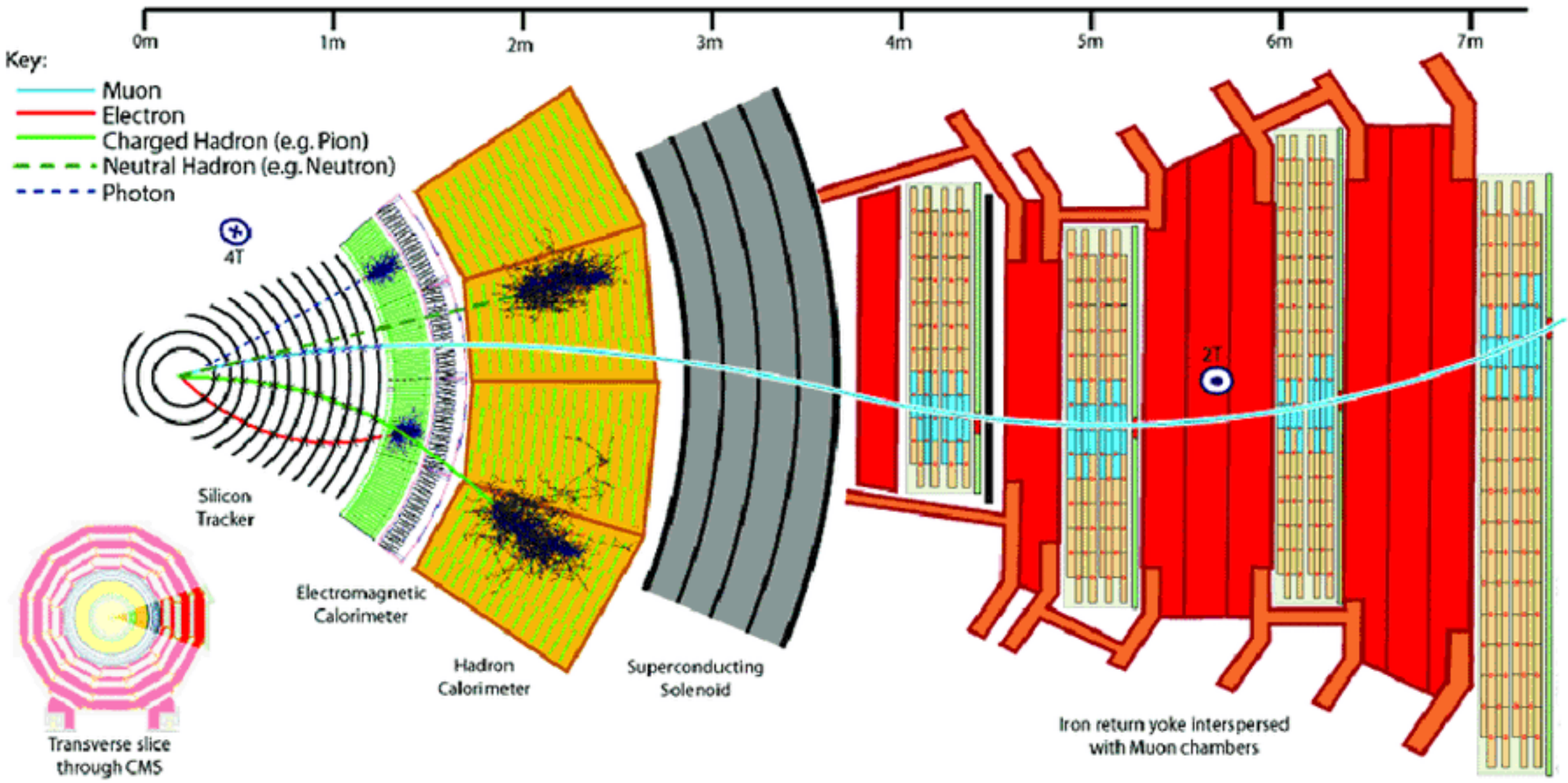
0m
1m
2m
3m
4m
5m
6m
7m
Key:
Muon
Electron
Charged Hadron (e.g. Pion)
Neutral Hadron (e.g. Neutron)
Photon
4T
2T
Silicon Tracker
Electromagnetic Calorimeter
Hadron Calorimeter
Superconducting Solenoid
Iron return yoke interspersed with Muon chambers
Transverse slice through CMS

CERN-ALICE

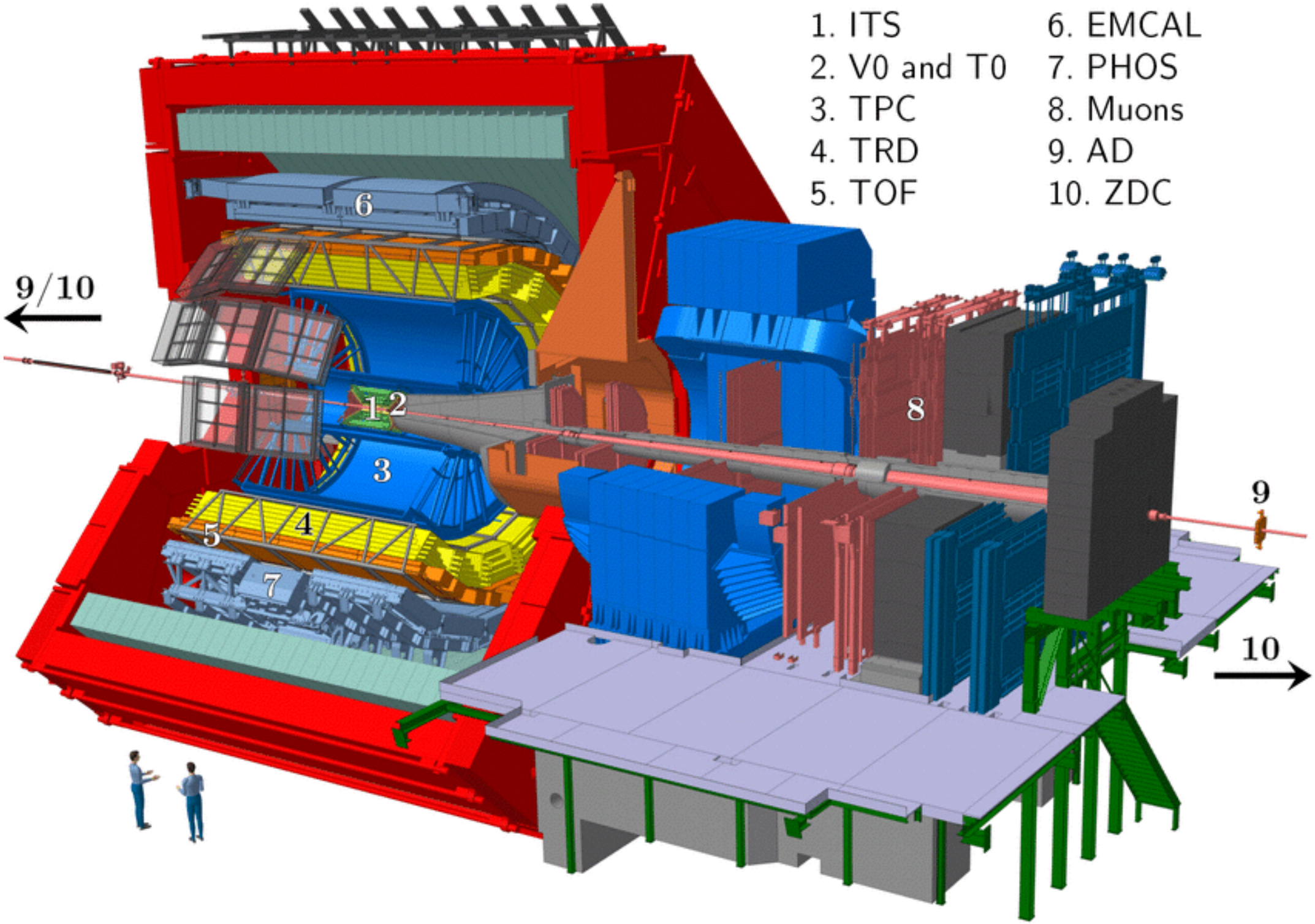
1. ITS
2. V0 and T0
3. TPC
4. TRD
5. TOF
6. EMCAL
7. PHOS
8. Muons
9. AD
10. ZDC
9/10
6
1
2
3
4
5
7
8
9
10

CERN-ALICE-ITS

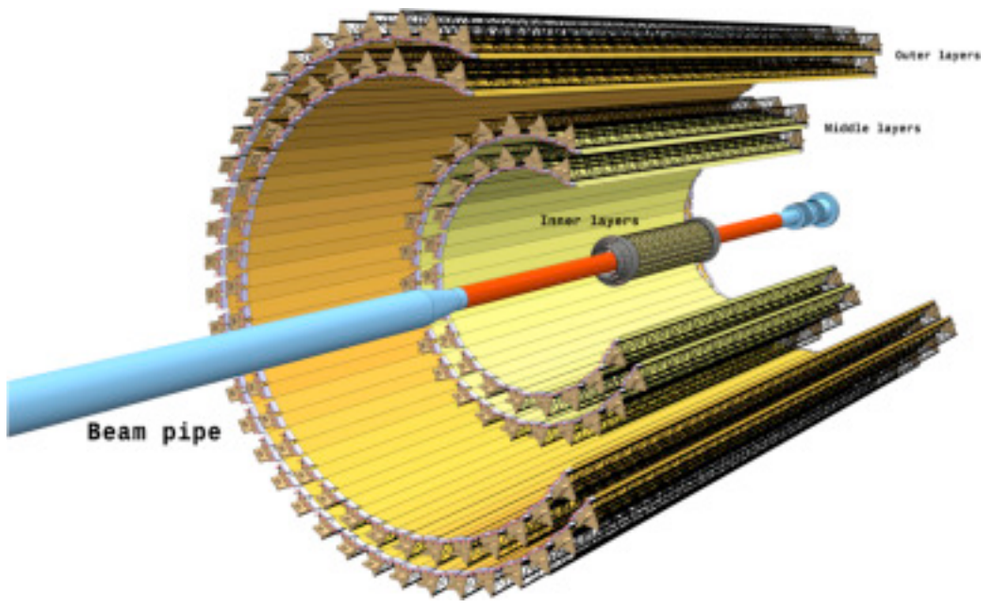

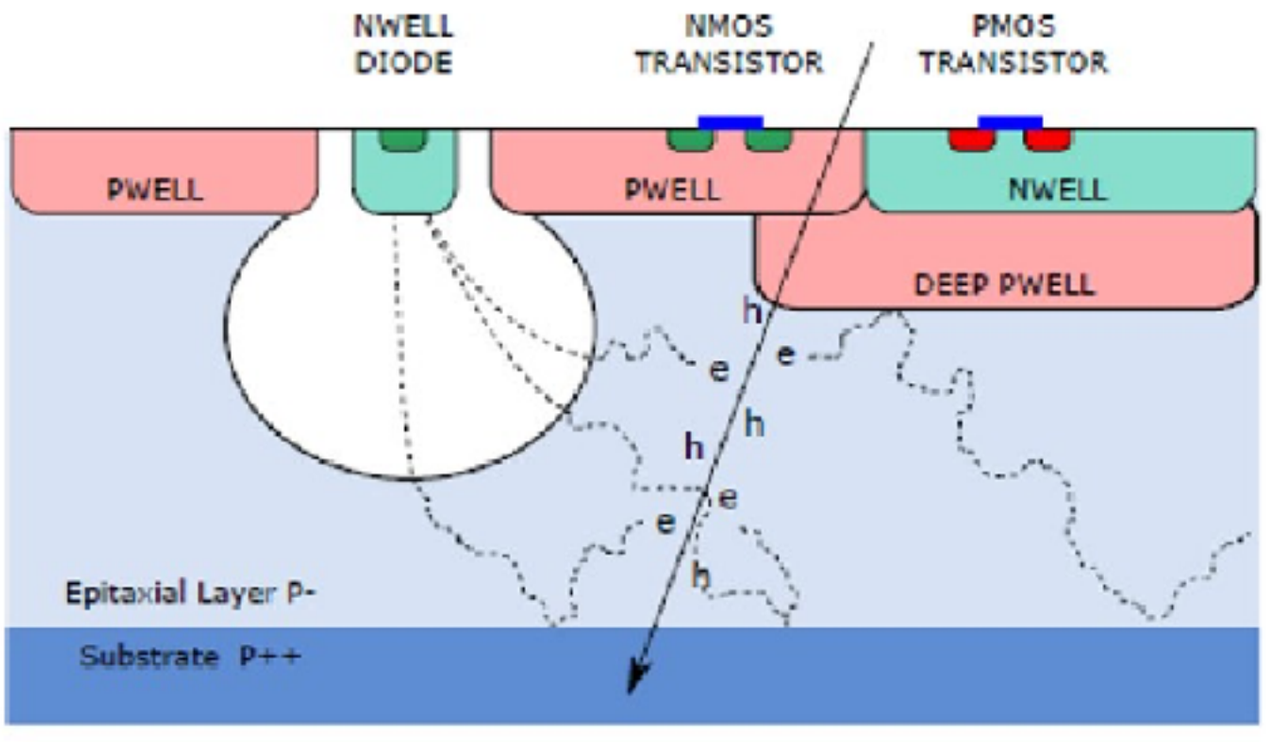

CERN-ATLAS

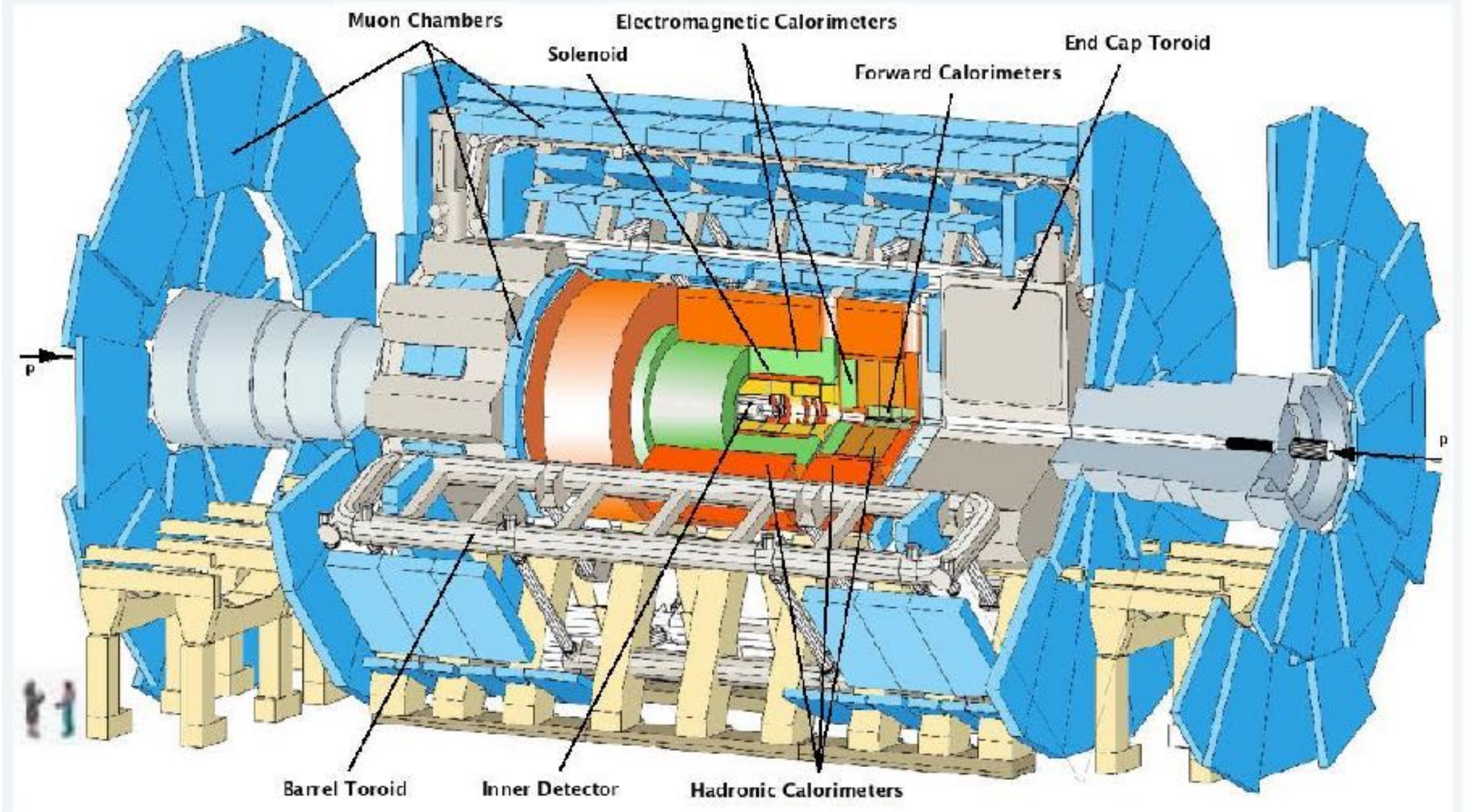
Muon Chambers
Electromagnetic Calorimeters
Solenoid
End Cap Toroid
Forward Calorimeters
p
p
Barrel Toroid
Inner Detector
Hadronic Calorimeters

IceCube Detector

Aims

1. Source of high energy neutrinos
2. Indirect dark matter
3. Neutrino oscillation
4. Galactic supernovae
5. Sterline neutrino

IceCube Detector

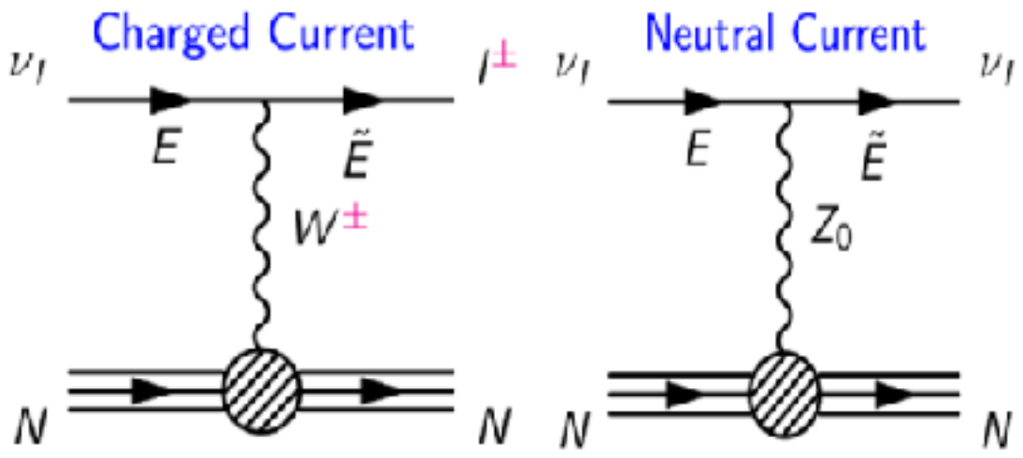

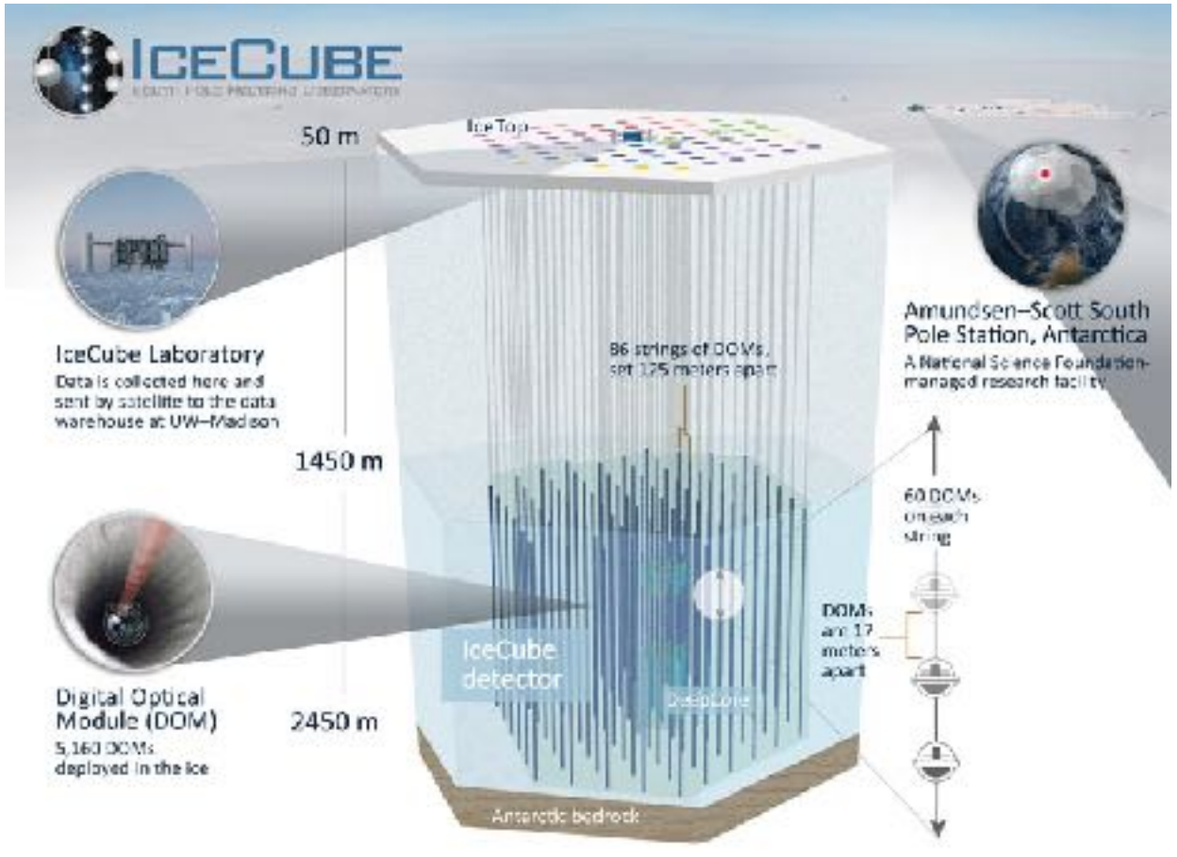

IceCube Detector

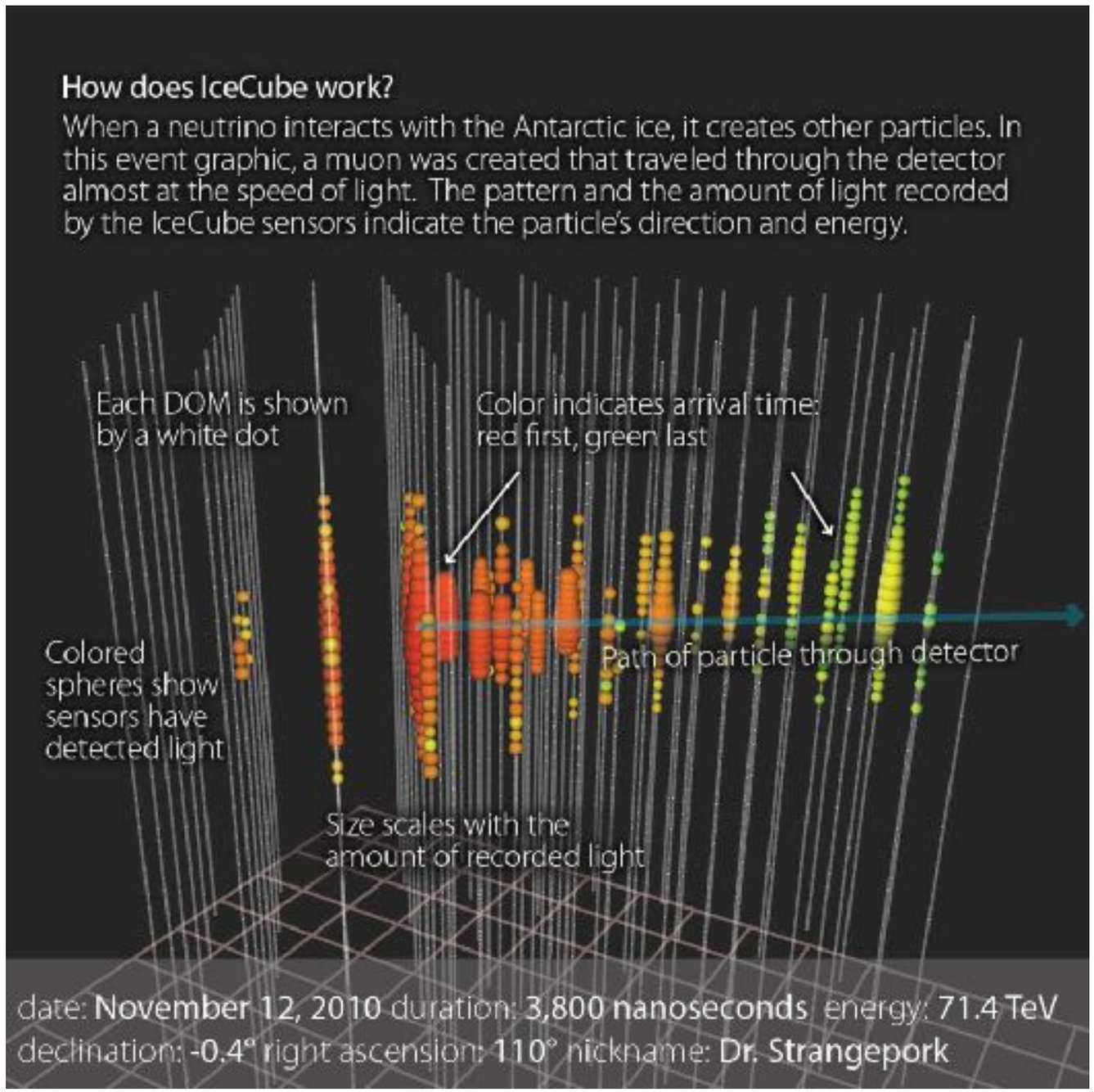

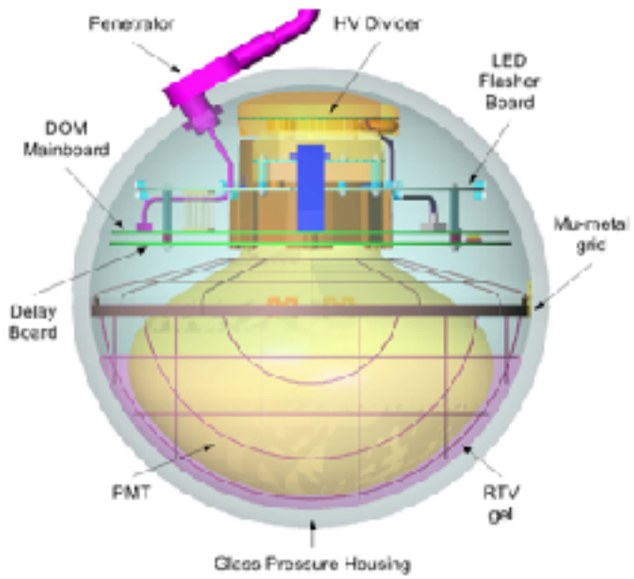

Reference

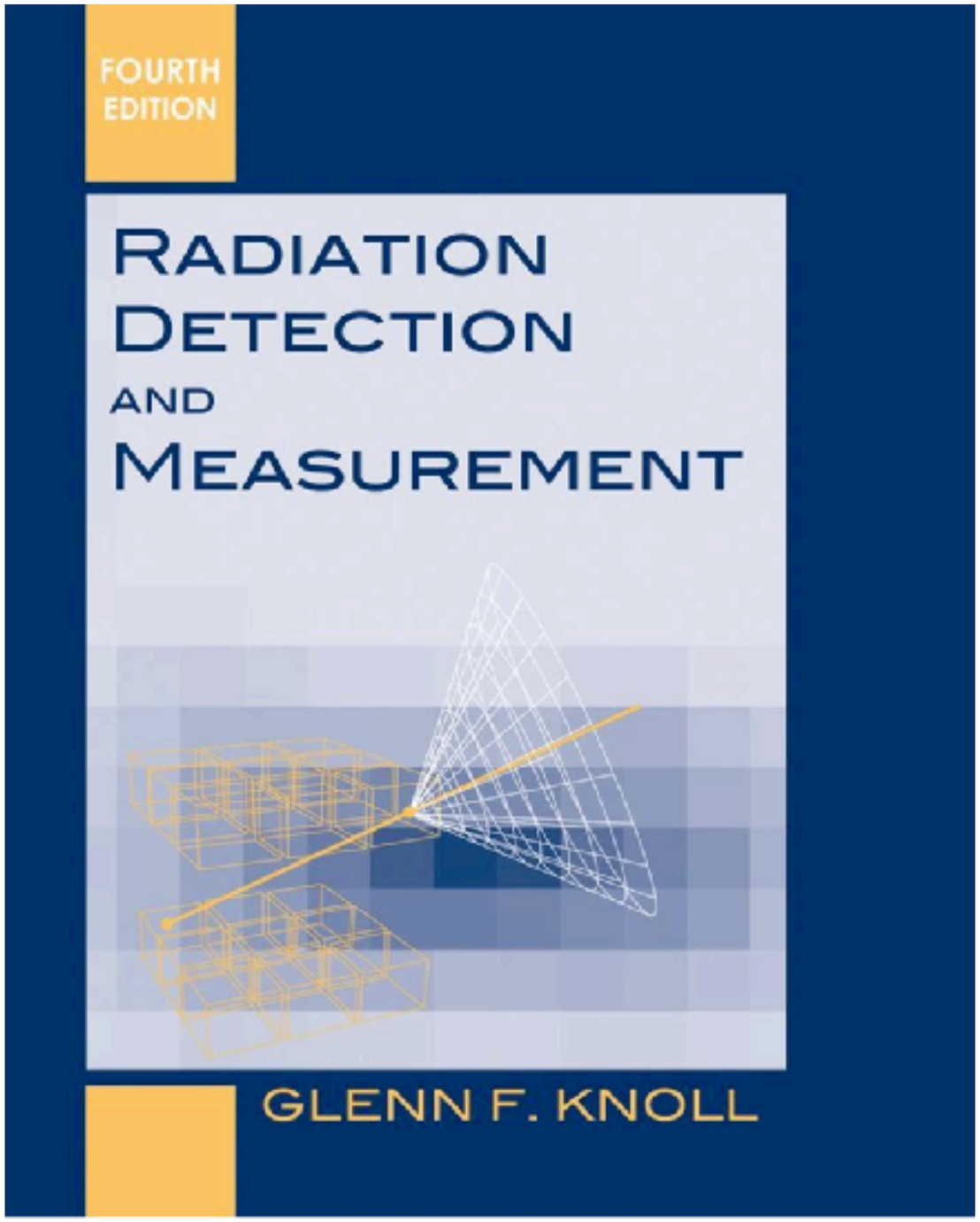
FOURTH
EDITION
RADIATION
DETECTION
AND
MEASUREMENT
GLENN F. KNOLL

Contents

Radiation Sources

Radiation Sources

Categories

Charged particulate radiation	Fast electrons Heavy charged particles
Uncharged radiation	Electromagnetic radiation Neutrons

1. **Fast electrons** : beta+/-
2. **Heavy charged particles** : alpha, proton, ions, fission products, nuclear reaction products
3. **Electromagnetic radiations** : gamma rays, X-rays
4. **Neutrons** : slow/fast neutron

Radiation Sources

Specific activity

$$\text{specific activity} \equiv \frac{\text{activity}}{\text{mass}} = \frac{\lambda N}{NM/A_v} = \frac{\lambda A_v}{M}$$

M = molecular weight of sample

A_v = Avogadro's number $(= 6.02 \times 10^{23}$ nuclei/mole$)$

λ = radioisotope decay constant $(= \ln 2/\text{half-life})$

Radiation Sources

Fast electron source : Beta Decay

$$^{A}_{Z}X \rightarrow {}^{A}_{Z+1}Y + \beta^{-} + \overline{\nu}$$

Table 1.1 Some "Pure" Beta-Minus Sources

Nuclide	Half-Life	Endpoint Energy (MeV)
^{3}H	12.26 y	0.0186
^{14}C	5730 y	0.156
^{32}P	14.28 d	1.710
^{33}P	24.4 d	0.248
^{35}S	87.9 d	0.167
^{36}Cl	3.08×10^{5} y	0.714
^{45}Ca	165 d	0.252
^{63}Ni	92 y	0.067
$^{90}Sr/^{90}Y$	27.7 y/64 h	0.546/2.27
^{99}Tc	2.12×10^{5} y	0.292
^{147}Pm	2.62 y	0.224
^{204}Tl	3.81 y	0.766

Data from Lederer and Shirley.[1]

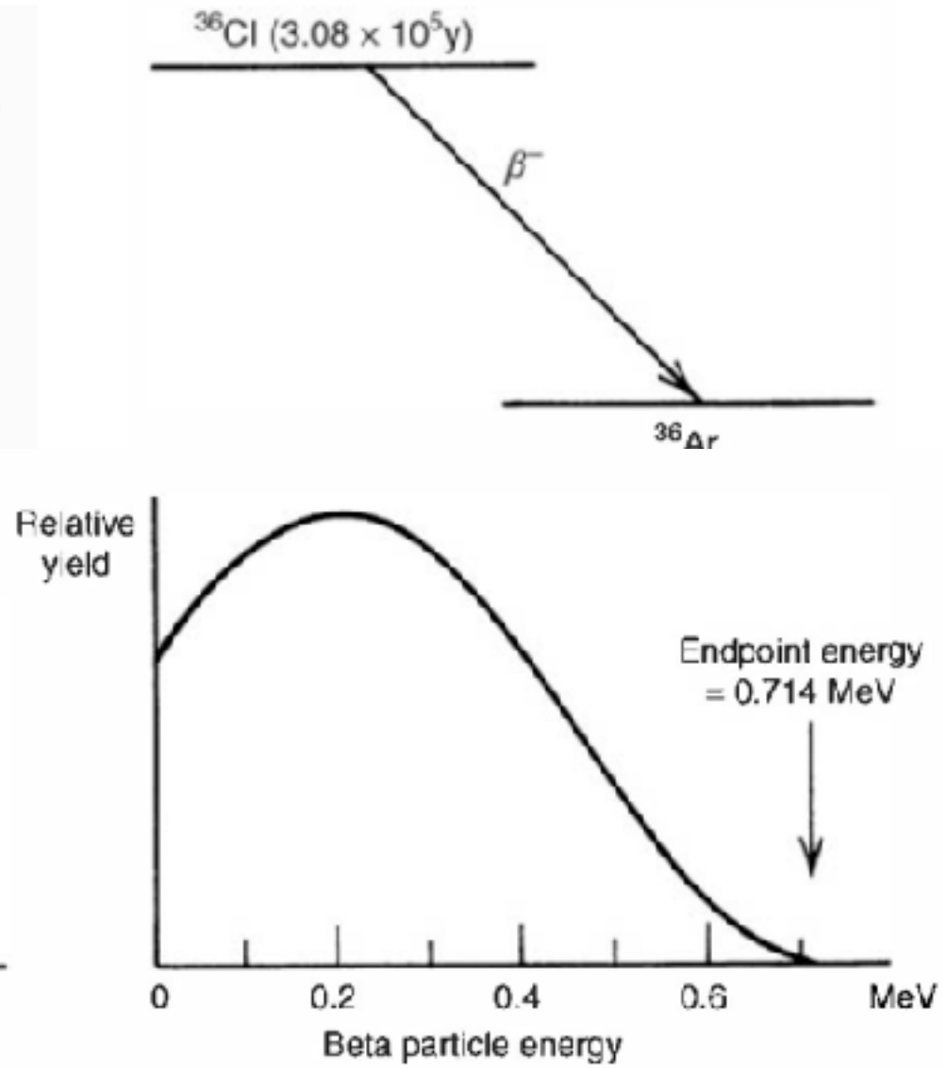

Radiation Sources

Fast electron source : Internal Conversion

The internal conversion process begins with an excited nuclear state, which may be formed by a preceding process—often beta decay of a parent species. The common method of de-excitation is through emission of a gamma-ray photon. For some excited states, gamma emission may be somewhat inhibited and the alternative of internal conversion can become significant. Here the nuclear excitation energy E_{ex} is transferred directly to one of the orbital electrons of the atom. This electron then appears with an energy given by

$$E_{e^-} = E_{ex} - E_b \tag{1.5}$$

where E_b is its binding energy in the original electron shell.

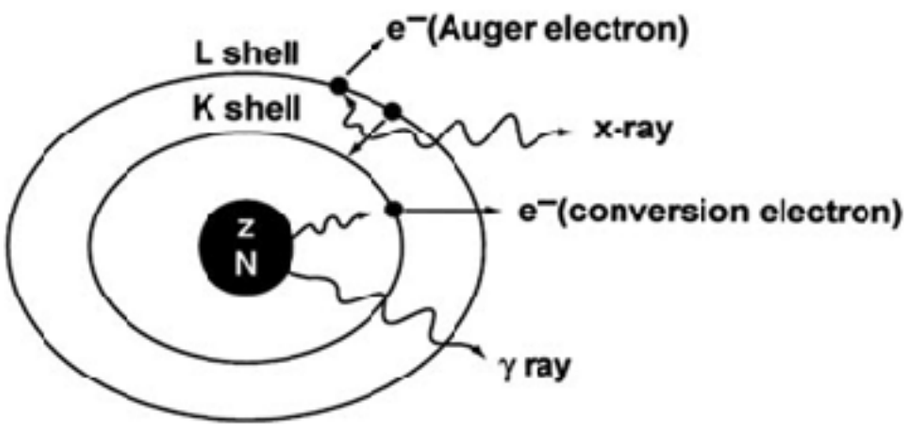

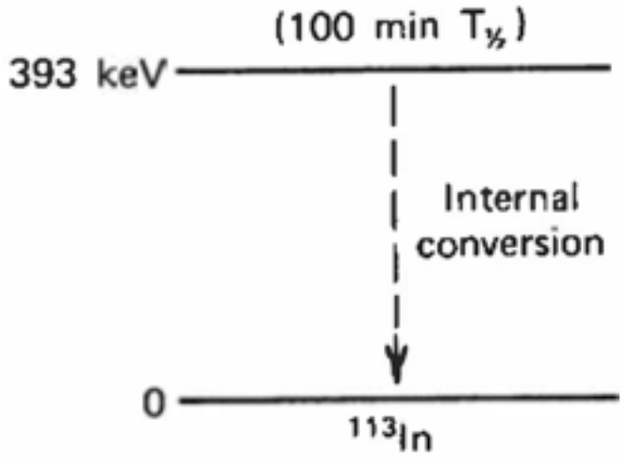

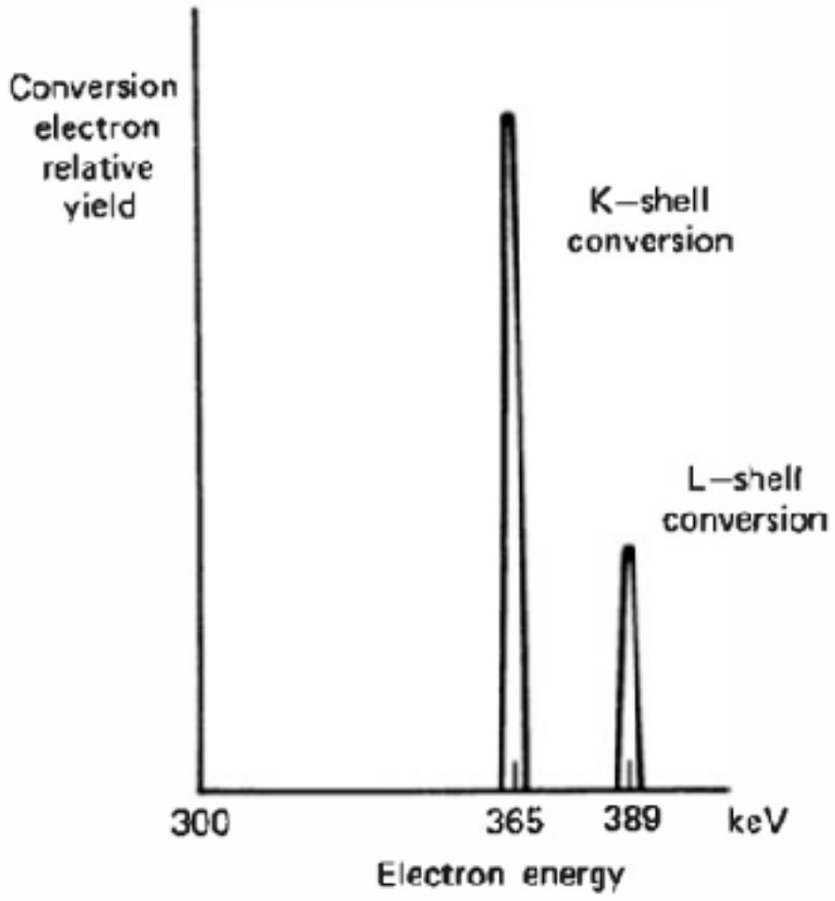

Radiation Sources

Fast electron source : Internal Conversion

Table 1.2 Some Common Conversion Electron Sources

Parent Nuclide	Parent Half-Life	Decay Mode	Decay Product	Transition Energy of Decay Product (keV)	Conversion Electron Energy (keV)
^{109}Cd	453 d	EC	^{109m}Ag	88	62 84
^{113}Sn	115 d	EC	^{113m}In	393	365 389
^{137}Cs	30.2 y	β^-	^{137m}Ba	662	624 656
^{139}Ce	137 d	EC	^{139m}La	166	126 159
^{207}Bi	38 y	EC	^{207m}Pb	570 1064	482 554 976 1048

Data from Lederer and Shirley.[1]

Radiation Sources

Heavy Charged Particle Sources : Alpha Decay

$$^{A}_{Z}X \rightarrow ^{A-4}_{Z-2}Y + ^{4}_{2}\alpha$$

Table 1.3 Common Alpha-Emitting Radioisotope Sources

Source	Half-Life	Alpha Particle Kinetic Energy (with Uncertainty) in MeV		Percent Branching
^{148}Gd	93 y	3.182787	±0.000024	100
^{232}Th	1.4×10^{10} y	4.012	±0.005	77
		3.953	±0.008	23
^{238}U	4.5×10^{9} y	4.196	±0.004	77
		4.149	±0.005	23
^{235}U	7.1×10^{8} y	4.598	±0.002	4.6
		4.401	±0.002	56
		4.374	±0.002	6
		4.365	±0.002	12
		4.219	±0.002	6
^{236}U	2.4×10^{7} y	4.494	±0.003	74
		4.445	±0.005	26
^{230}Th	7.7×10^{4} y	4.6875	±0.0015	76.3
		4.6210	±0.0015	23.4
^{234}U	2.5×10^{5} y	4.7739	±0.0009	72
		4.7220	±0.0009	28
^{231}Pa	3.2×10^{4} y	5.0590	±0.0008	11
		5.0297	±0.0008	20
		5.0141	±0.0008	25.4
		4.9517	±0.0008	22.8
^{239}Pu	2.4×10^{4} y	5.1554	±0.0007	73.3
		5.1429	±0.0008	15.1
		5.1046	±0.0008	11.5

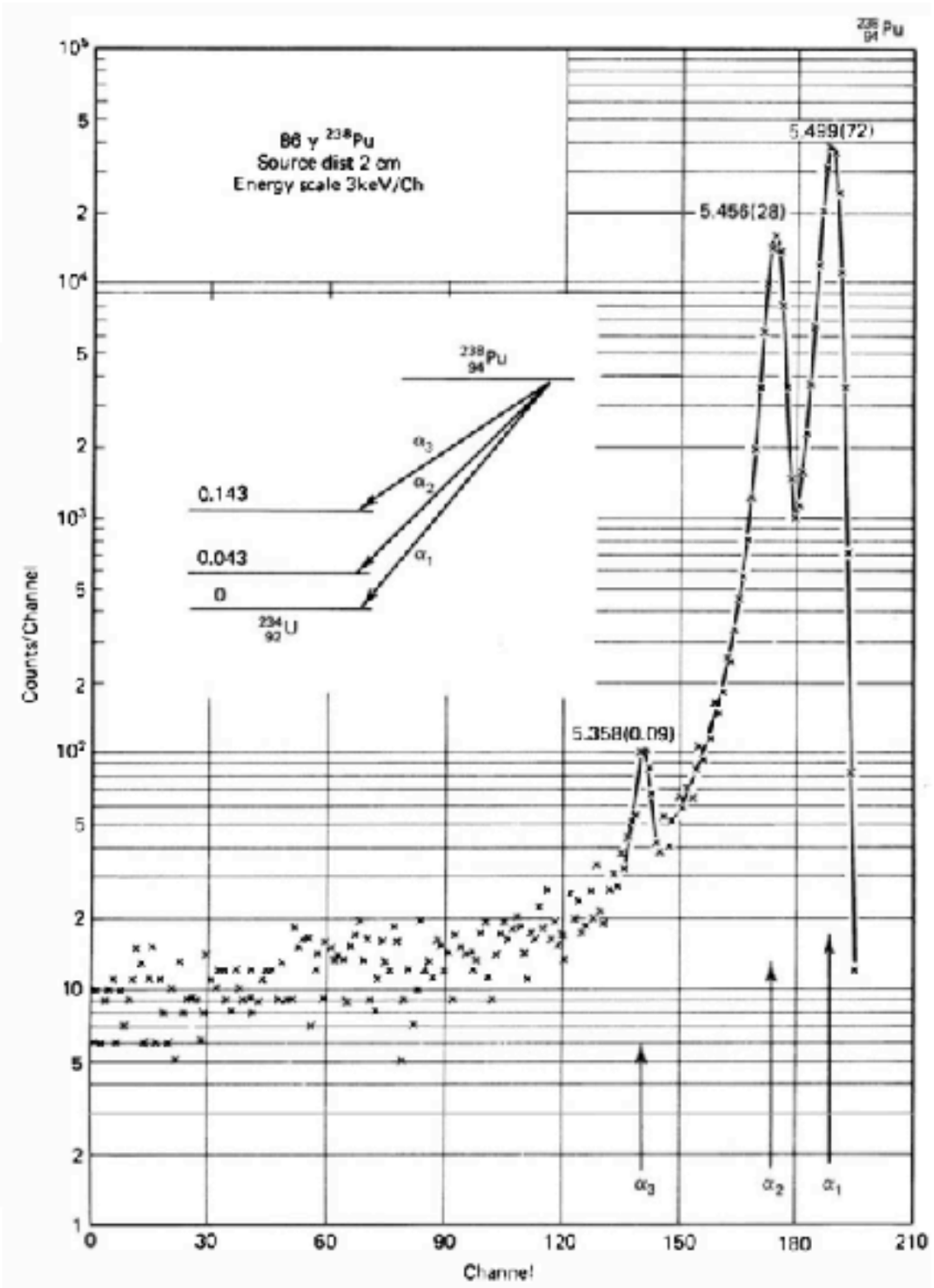

Radiation Sources

Heavy Charged Particle Sources : Spontaneous Fission

All heavy nuclei are, in principle, unstable against spontaneous fission into two lighter fragments. For all but the extremely heavy nuclei, however, the process is inhibited by the large potential barrier that must be overcome in the distortion of the nucleus from its original near-spherical shape. Spontaneous fission is therefore not a significant process except for some transuranic isotopes of very large mass number. The most widely used example is

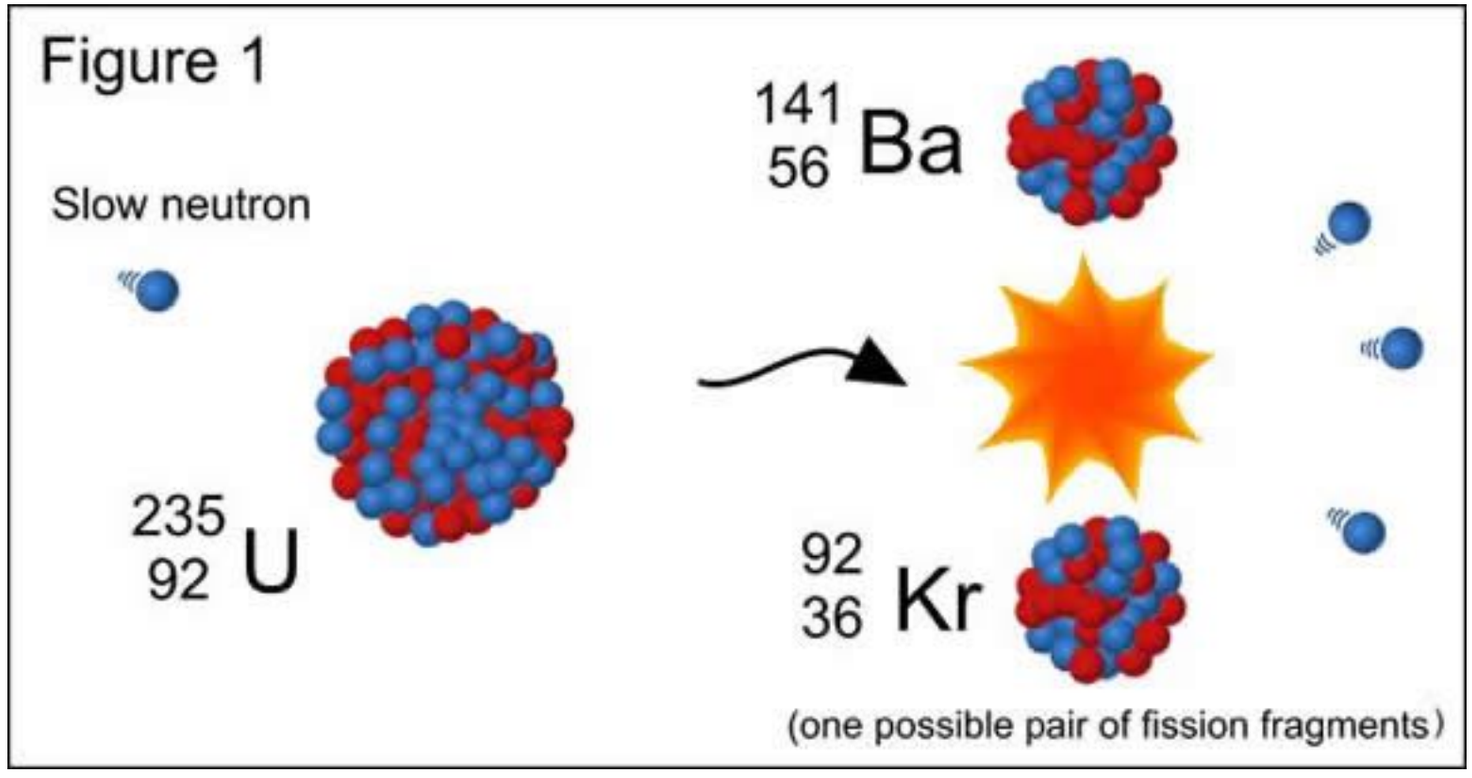

Picture: https://www.arpansa.gov.au/understanding-radiation/what-is-radiation/ionising-radiation/radiation-decay

Radiation Sources

Electromagnetic Radiation : Gamma rays/X-rays

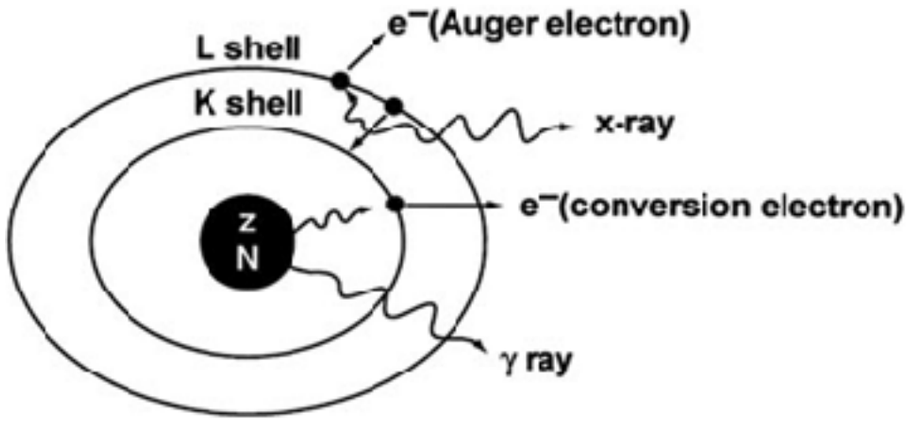

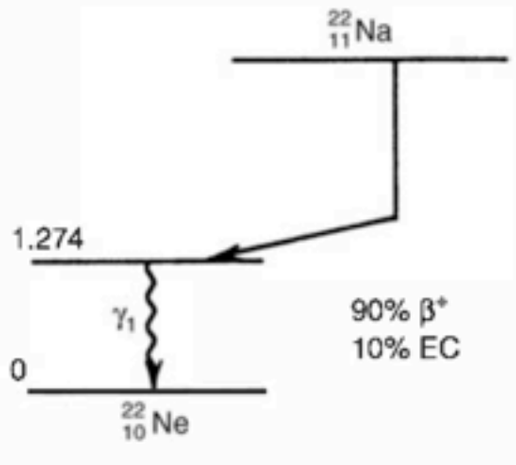

γ1 : 1.274 MeV γ (100%)
annihilation radiation
Ne char. X-rays

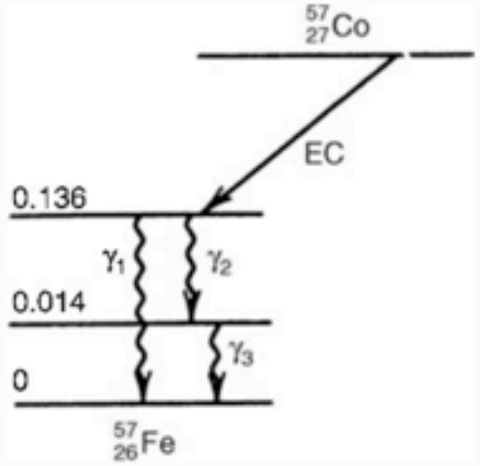

γ1 : 0.136 MeV γ (11%)
γ2 : 0.122 MeV γ (87%)
γ3 : 0.014 MeV γ (9%)
Fe char. X-rays

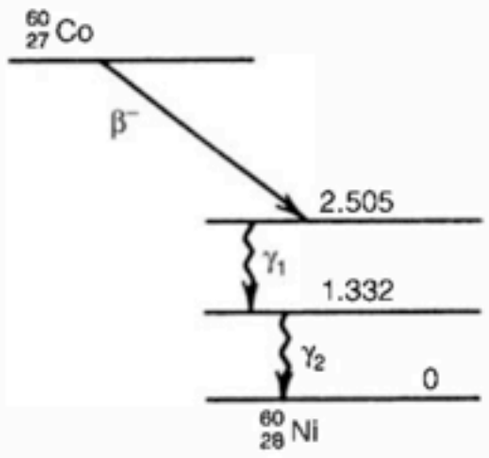

γ1 : 1.173 MeV γ (100%)
γ2 : 1.332 MeV γ (100%)

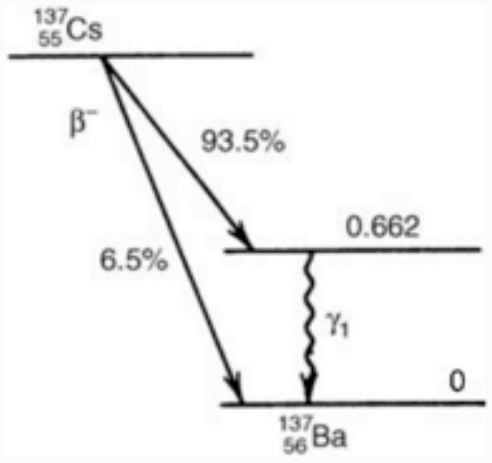

γ1 : 0.662 MeV γ (85%)
Ba char. X-rays

Radiation Sources

Electromagnetic Radiation : Annihilation radiation

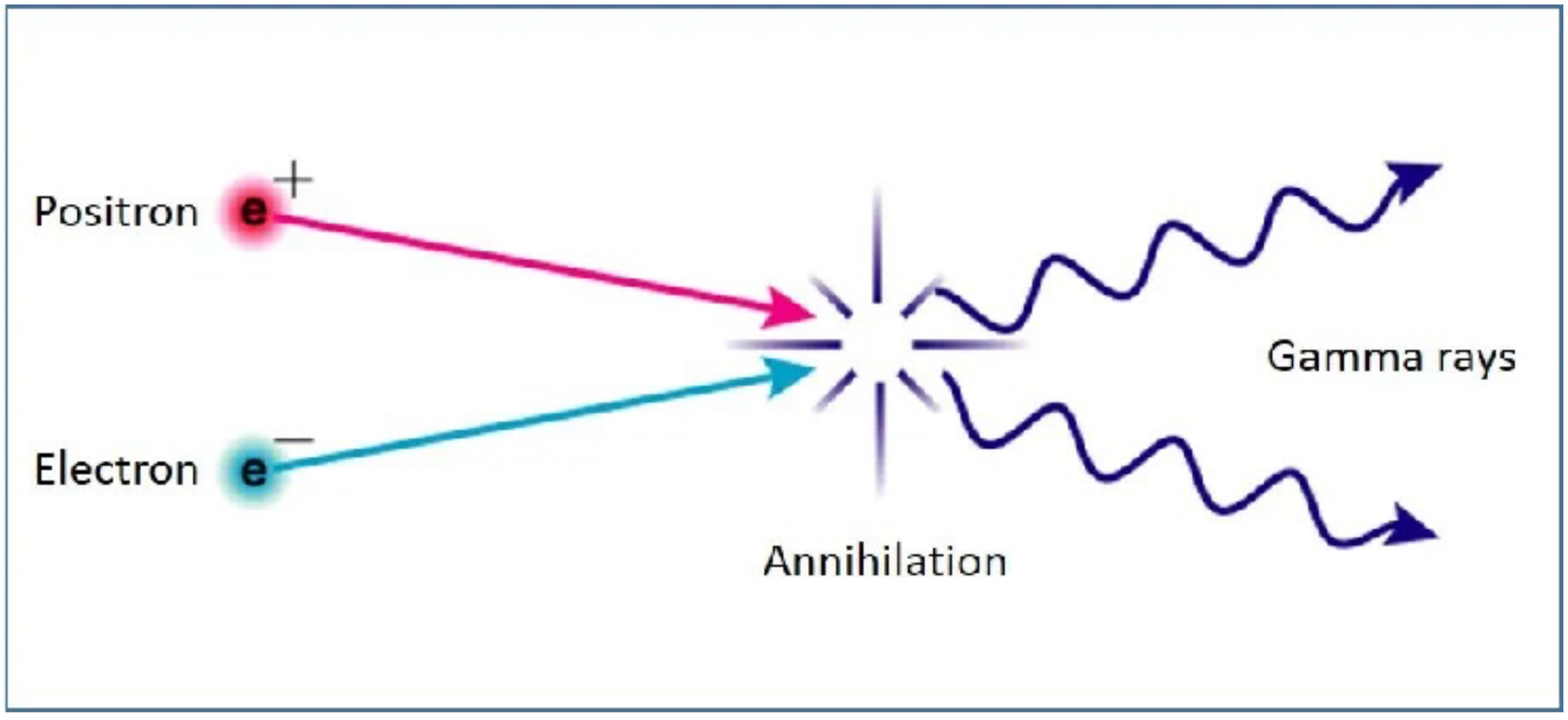

Picture: https://alevelphysics.co.uk/notes/particle-antiparticle-photons/

Radiation Sources

Electromagnetic Radiation :
Bremsstrahlung & Characteristic X-rays

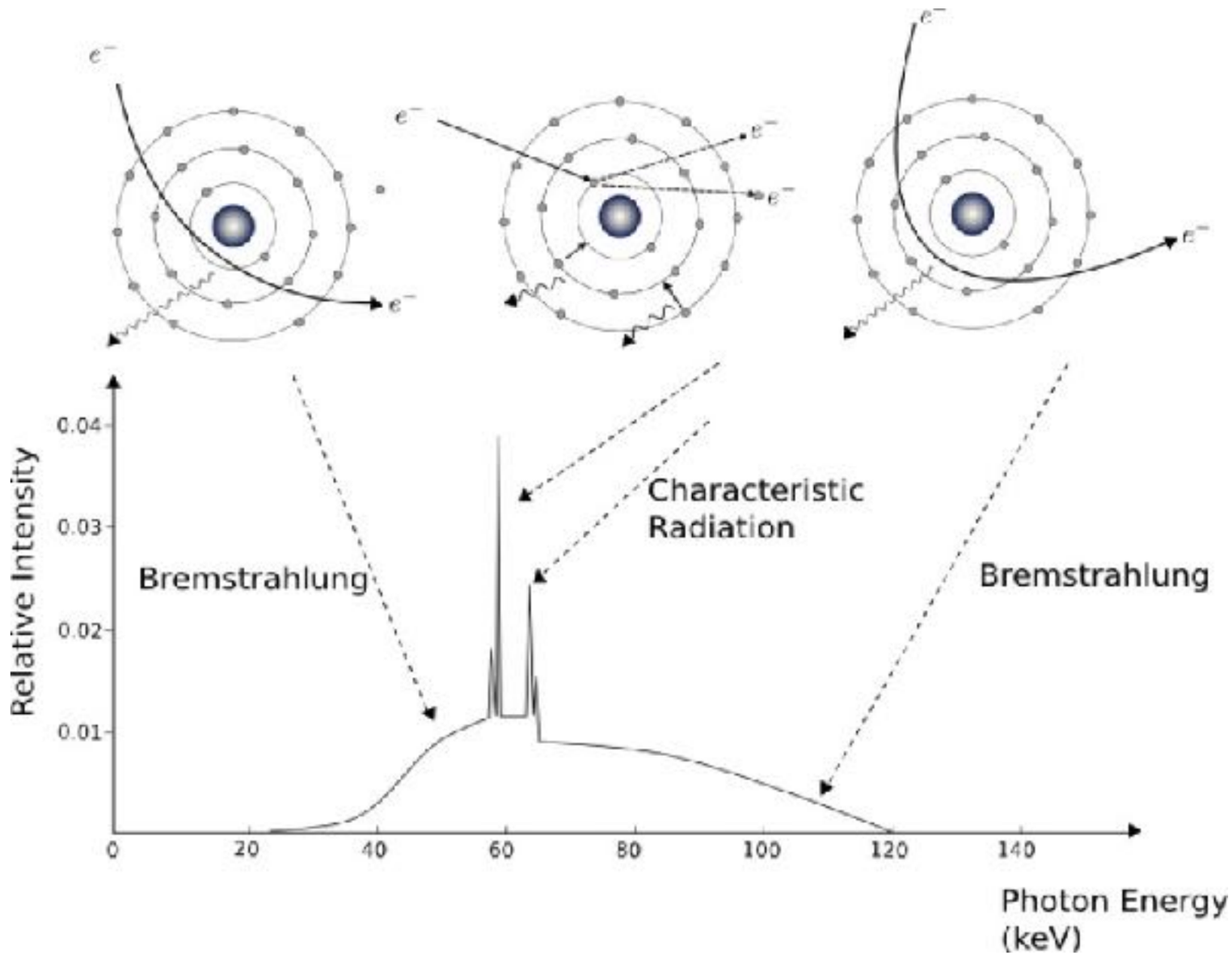

Picture: https://www.ncbi.nlm.nih.gov/books/NBK546155/figure/ch7.fig8/

Radiation Sources

Electromagnetic Radiation :
Bremsstrahlung & Characteristic X-rays

1. **Excitation by Radioactive Decay**

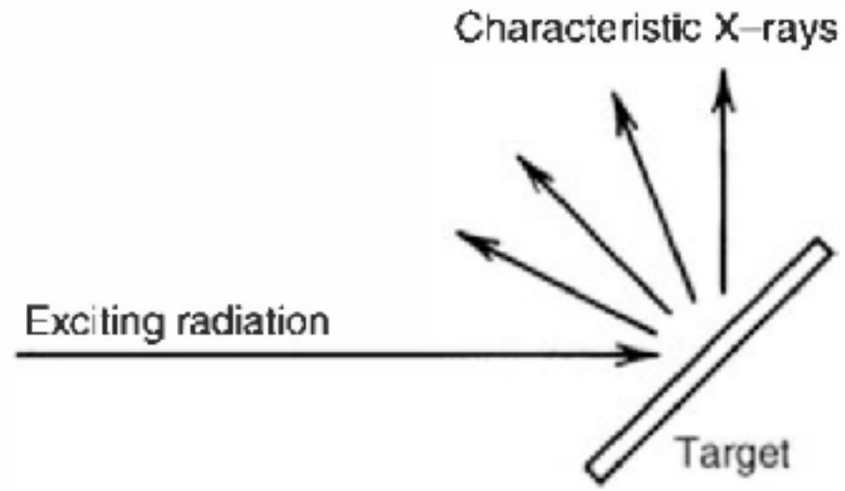

2. **Excitation by External Radiation**

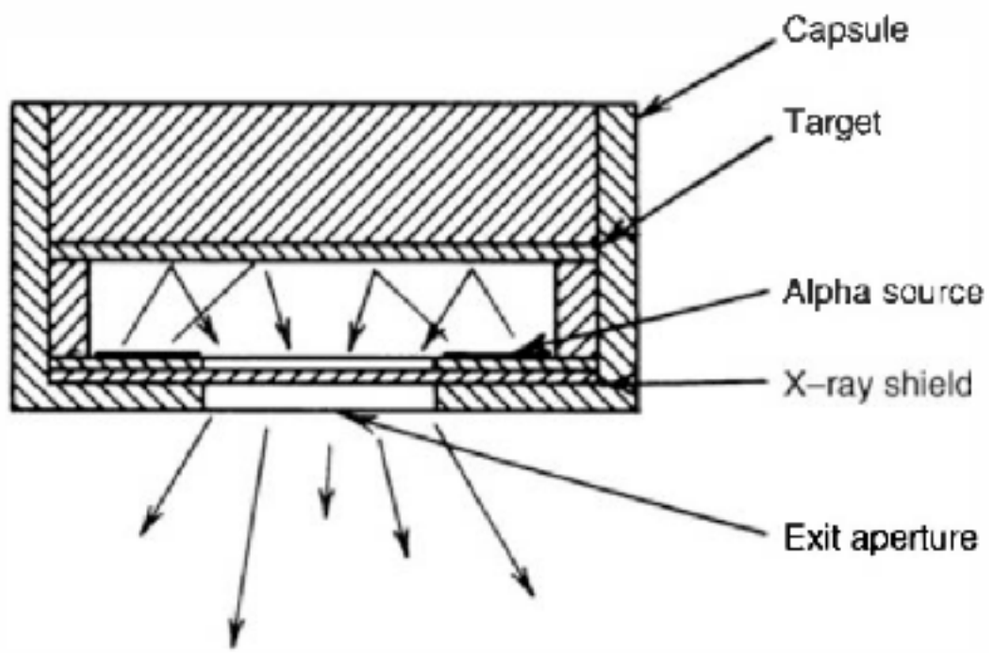

Radiation Sources

Electromagnetic Radiation : Synchrotron Radiation

1. From bending magnet

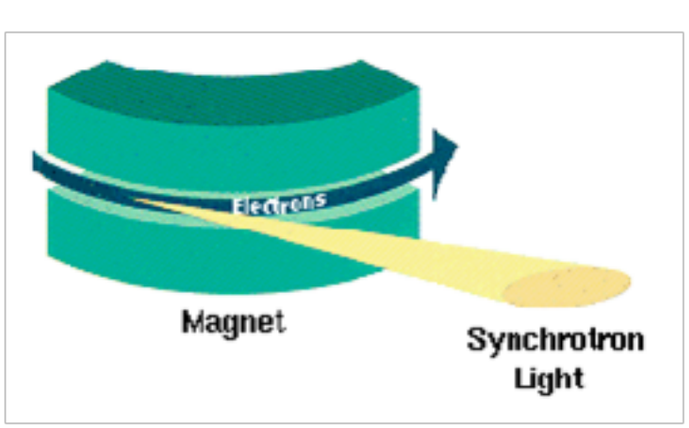

2. From undulator

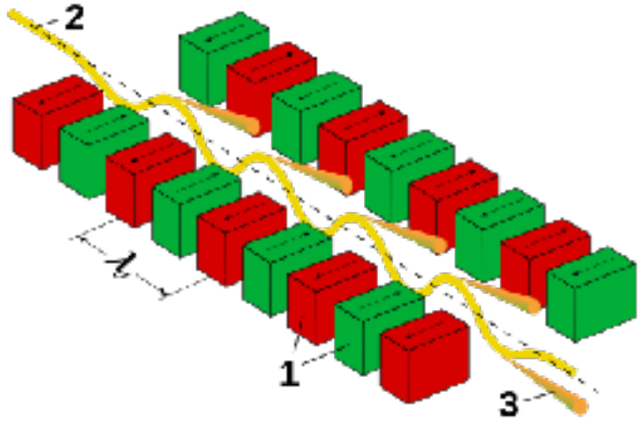

3. From astronomical source

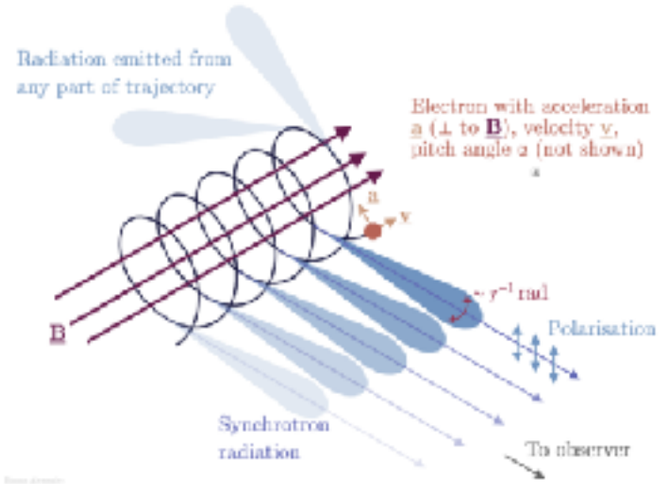

Picture: https://en.wikipedia.org/wiki/Synchrotron_radiation

Radiation Sources

Neutron sources

1. Spontaneous fission

$$^{87}\mathrm{Br} \rightarrow {}^{87}\mathrm{Kr}^{*} + \beta^{-}$$
$$^{87}\mathrm{Kr}^{*} \rightarrow {}^{86}\mathrm{Kr} + \mathrm{n}$$

2. Radioisotope source (α,n)

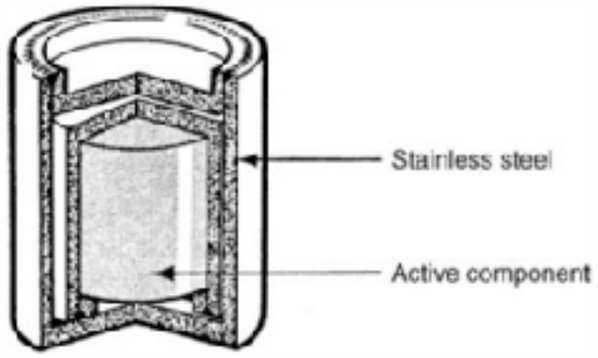

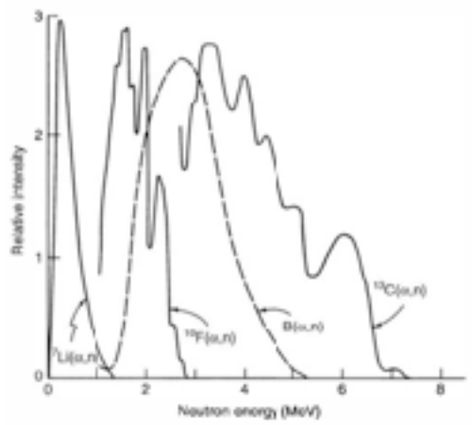

Figure 1.14 Neutron energy spectra from alternative (α, n) sources. (^{7}Li data from Geiger and Van der Zwan,[28] and remainder from Lorch.[20])

3. Photoneutron source

$$^{9}_{4}\mathrm{Be} + h\nu \rightarrow {}^{8}_{4}\mathrm{Be} + {}^{1}_{0}\mathrm{n}$$
$$^{2}_{1}\mathrm{H} + h\nu \rightarrow {}^{1}_{1}\mathrm{H} + {}^{1}_{0}\mathrm{n}$$

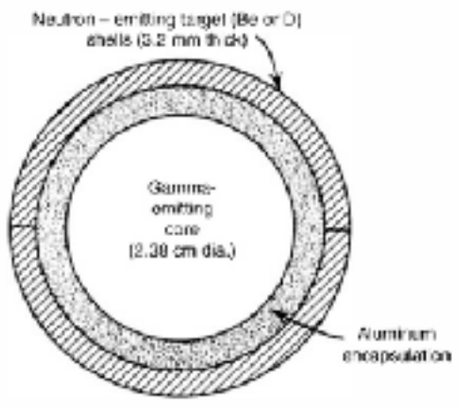

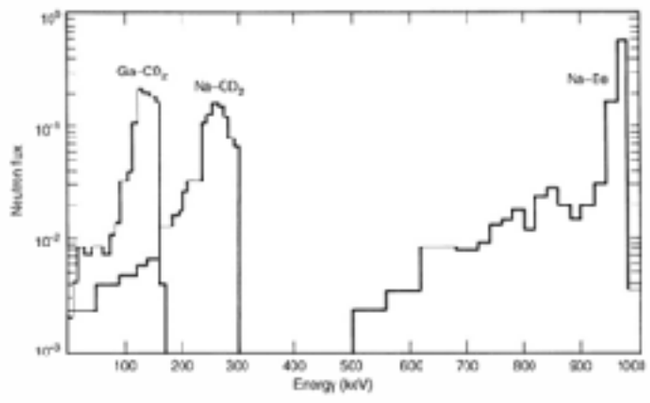

Figure 1.15 Neutron spectra calculated for the photoneutron source dimensions shown in Fig. 1.15. The gamma emitters are either ^{72}Ga or ^{24}Na. The outer shells are either deuterated polyethylene (CD_2) or beryllium (Be).

4. Reaction from accelerated charged particles

The D-D reaction $\quad {}^{2}_{1}\mathrm{H} + {}^{2}_{1}\mathrm{H} \rightarrow {}^{3}_{2}\mathrm{He} + {}^{1}_{0}\mathrm{n}$

The D-T reaction $\quad {}^{2}_{1}\mathrm{H} + {}^{3}_{1}\mathrm{H} \rightarrow {}^{4}_{2}\mathrm{He} + {}^{1}_{0}\mathrm{n}$

Radiation Sources

Neutron sources

Table 1.6 Characteristics of Be(α, n) Neutron Sources

Source	Half-Life	E_α (MeV)	Neutron Yield per 10^6 Primary Alpha Particles		Percent Yield with $E_n < 1.5$ MeV	
			Calculated	Experimental	Calculated	Experimental
^{239}Pu/Be	24,000 y	5.14	65	57	11	9–33
^{210}Po/Be	138 d	5.30	73	69	13	12
^{238}Pu/Be	87.4 y	5.48	79[a]	—	—	—
^{241}Am/Be	433 y	5.48	82	70	14	15–23
^{244}Cm/Be	18 y	5.79	100[b]	—	18	29
^{242}Cm/Be	162 d	6.10	118	106	22	26
^{226}Ra/Be + daughters	1602 y	Multiple	502	—	26	33–38
^{227}Ac/Be + daughters	21.6 y	Multiple	702	—	28	38

[a]From Anderson and Hertz.[23] All other data as calculated or cited in Geiger and Van der Zwan.[24]
[b]Does not include a 4% contribution from spontaneous fission of ^{244}Cm.

Radiation Sources

Neutron sources

Table 1.7 Alternative (α, n) Isotopic Neutron Sources

Target	Reaction	*Q*-Value	Neutron Yield per 10^6 Alpha Particles
Natural B	$^{10}B(\alpha, n)$	+1.07 MeV	13 for ^{241}Am alpha particles
	$^{11}B(\alpha, n)$	+0.158 MeV	
F	$^{19}F(\alpha, n)$	−1.93 MeV	4.1 for ^{241}Am alpha particles
Isotopically separated ^{13}C	$^{13}C(\alpha, n)$	+2.2 MeV	11 for ^{238}Pu alpha particles
Natural Li	$^{7}Li(\alpha, n)$	−2.79 MeV	
Be (for comparison)	$^{9}Be(\alpha, n)$	+5.71 MeV	70 for ^{241}Am alpha particles

Data from Lorch[20] and Geiger and Van der Zwan.[28]

Radiation Sources

Neutron sources

Table 1.8 Photoneutron Source Characteristics

Gamma-Ray Emitter	Half-Life[a]	Gamma Energy[a] (MeV)	Target	Neutron Energy[b] (keV)	Neutron Yield (n/s) for 10^{10} Bq Activity[c]
^{24}Na	15.0 h	2.7541	Be	967	340,000
		2.7541	D	263	330,000
^{28}Al	2.24 min	1.7787	Be	101	32,600
^{38}Cl	37.3 min	2.1676	Be	446	43,100
^{56}Mn	2.58 h	1.8107	Be	129	91,500
		2.1131		398	
		2.9598		1149	
		2.9598	D	365	162
^{72}Ga	14.1 h	1.8611	Be	174	64,900
		2.2016		476	
		2.5077		748	
		2.5077	D	140	25,100
^{76}As	26.3 h	1.7877	Be	109	3050
		2.0963		383	
^{88}Y	107 d	1.8361	Be	152	229,000
		2.7340		949	
		2.7340	D	253	160
^{116m}In	54.1 min	2.1121	Be	397	15,600
^{124}Sb	60.2 d	1.6910	Be	23	210,000
^{140}La	40.3 h	2.5217	Be	760	10,200
		2.5217	D	147	6600
^{144}Pr	17.3 min	2.1856	Be	462	690

[a]Decay data from Ref. 1.

[b]Calculated for $\theta = \pi/2$, approximate midpoint of primary spectrum.

[c]Monte Carlo calculations for the source dimensions given in Fig. 1.15. Outer target shells are either metallic Be or deuterated polyethylene. Core materials assumed to be NaF, Al, CCl_4, MnO_2, Ga_2O_3, As_2O_3, Y_2O_3, In, Sb, La_2O_3, and Pr_2O_3.

Source: G. F. Knoll, "Radioisotope Neutron Sources," Chap. 2 in *Neutron Sources for Basic Physics and Applications*, Pergamon Press, New York, 1983.

Radiation Interactions

Radiation Interactions

Nature of interactions

Charged Particulate Radiations		Uncharged Radiations
Heavy charged particles (characteristic distance $\cong 10^{-5}$ m)	$\Leftarrow$	Neutrons (characteristic length $\cong 10^{-1}$ m)
Fast electrons (characteristic distance $\cong 10^{-3}$ m)	$\Leftarrow$	X-rays and gamma rays (characteristic length $\cong 10^{-1}$ m)

Radiation Interactions

Stopping power

$$S = -\frac{dE}{dx}$$

$$-\frac{dE}{dx} = \frac{4\pi e^4 z^2}{m_0 v^2} NB$$

$$B \equiv Z\left[\ln\frac{2m_0v^2}{I} - \ln\left(1-\frac{v^2}{c^2}\right) - \frac{v^2}{c^2}\right]$$

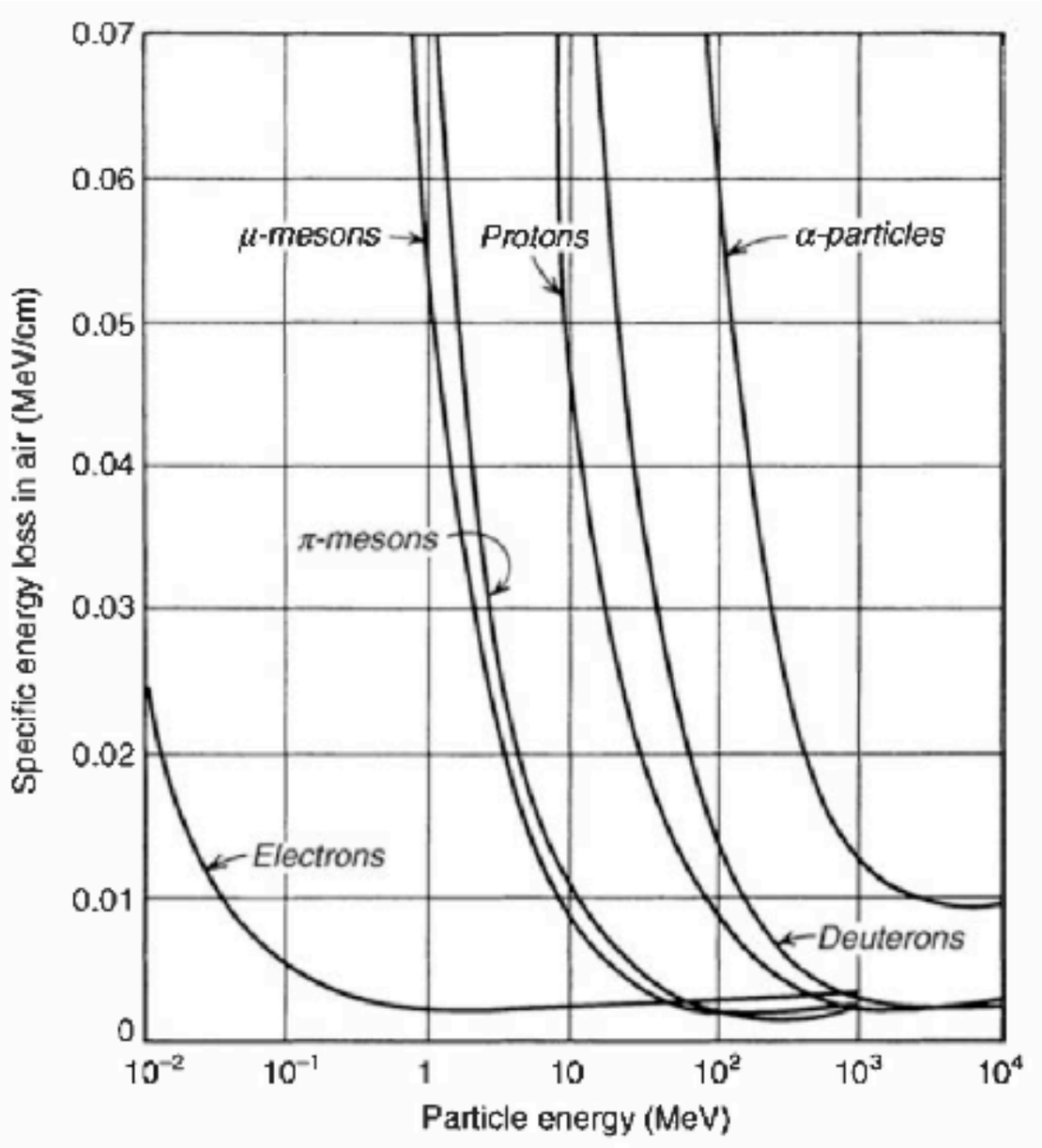

Radiation Interactions

Energy loss : Bragg Curve

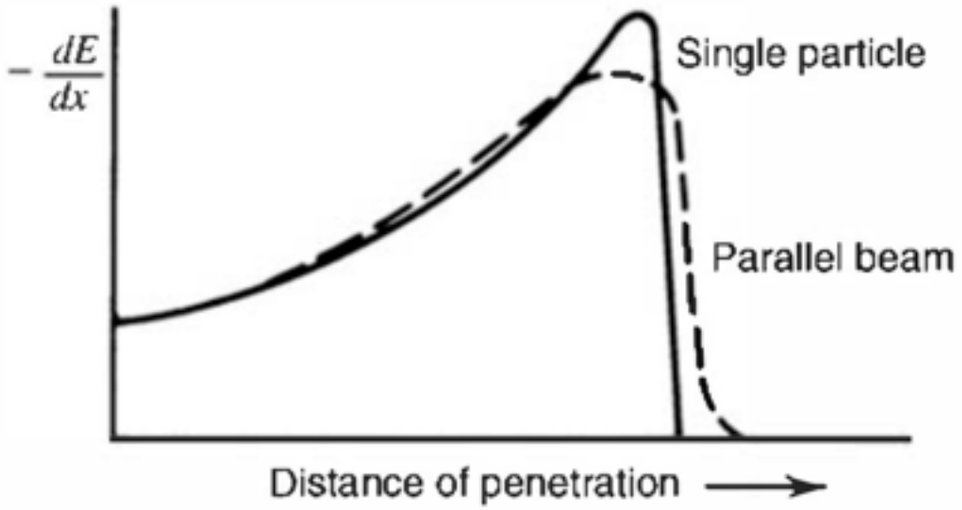

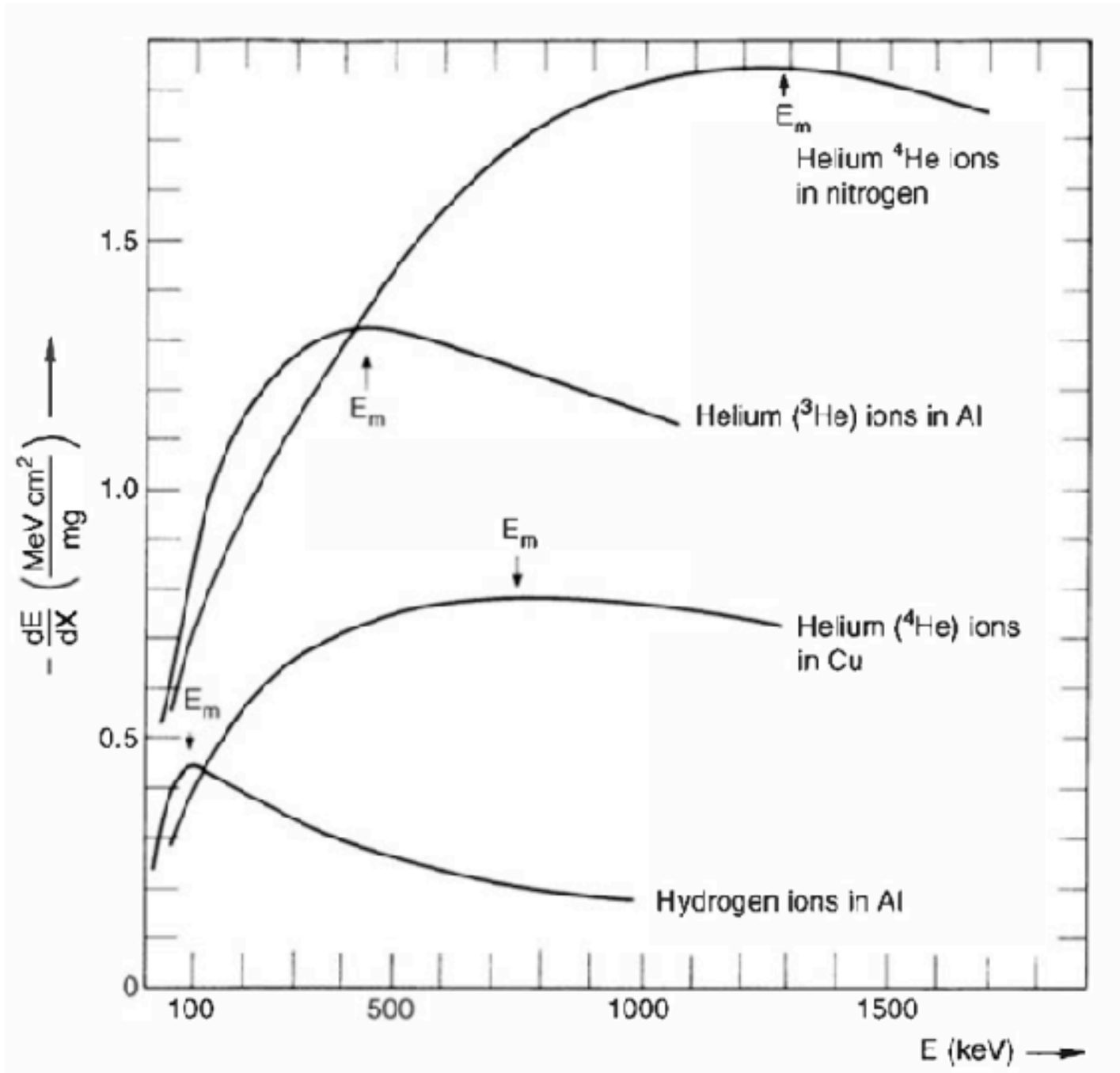

Radiation Interactions

Energy loss : Energy straggling

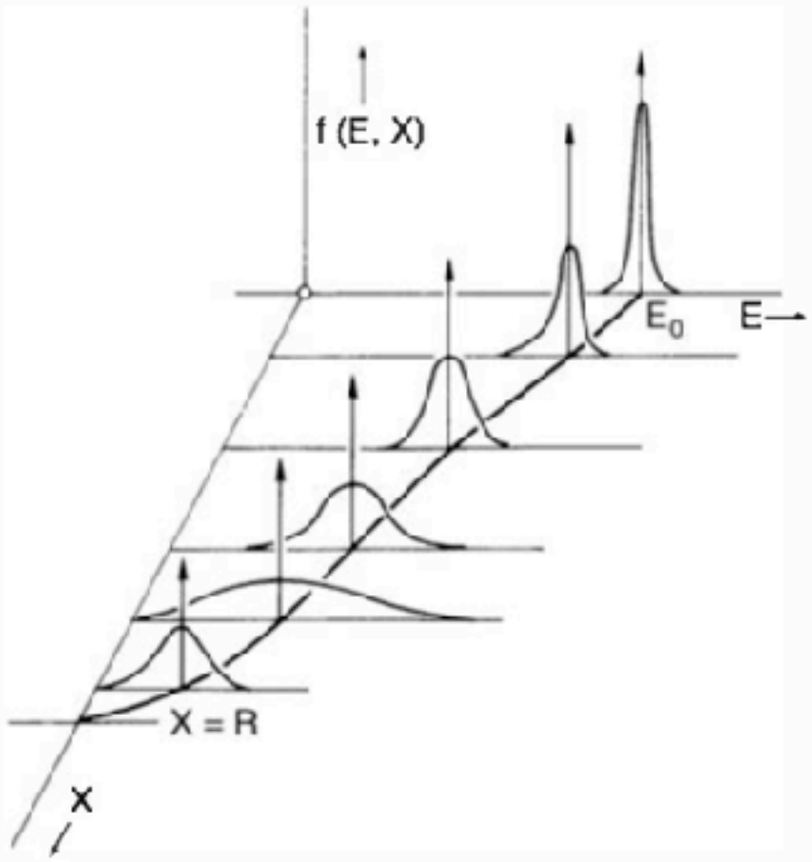

Figure 2.4 Plots of energy distribution of a beam of initially monoenergetic charged particles at various penetration distances. *E* is the particle energy and *X* is the distance along the track. (From Wilken and Fritz.[3])

Radiation Interactions

Range

The range of the alpha particles in the absorber material can be determined from this curve in several ways. The *mean range* is defined as the absorber thickness that reduces the alpha particle count to exactly one-half of its value in the absence of the absorber. This definition is most commonly used in tables of numerical range values. Another version that appears in the literature is the *extrapolated range*, which is obtained by extrapolating the linear portion of the end of the transmission curve to zero.

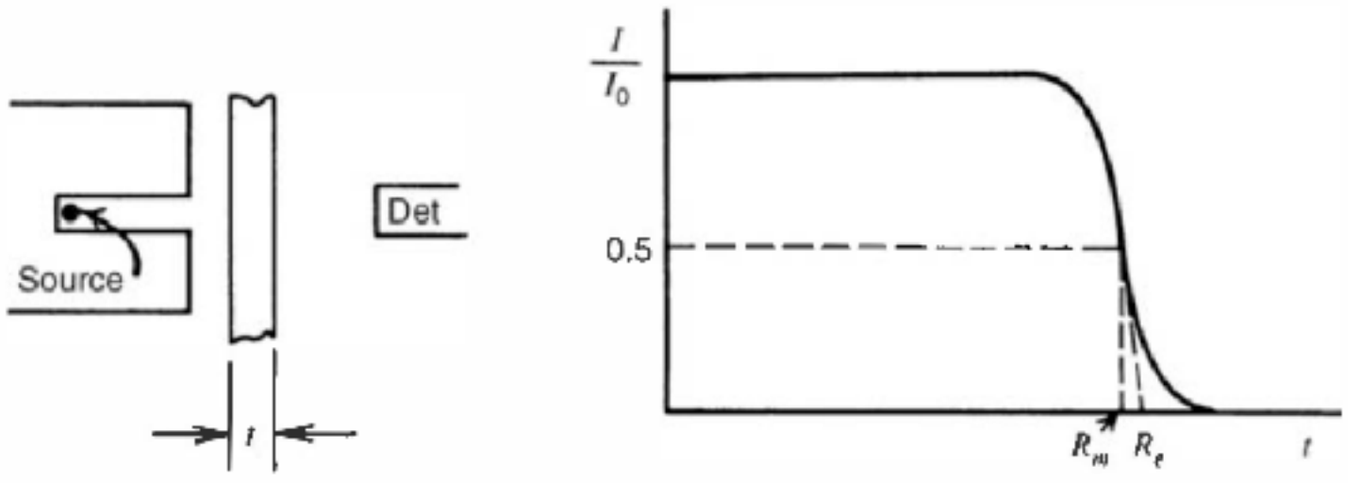

Figure 2.5 An alpha particle transmission experiment. I is the detected number of alpha particles through an absorber thickness t, whereas I_0 is the number detected without the absorber. The mean range R_m and extrapolated range R_e are indicated.

Radiation Interactions

Range

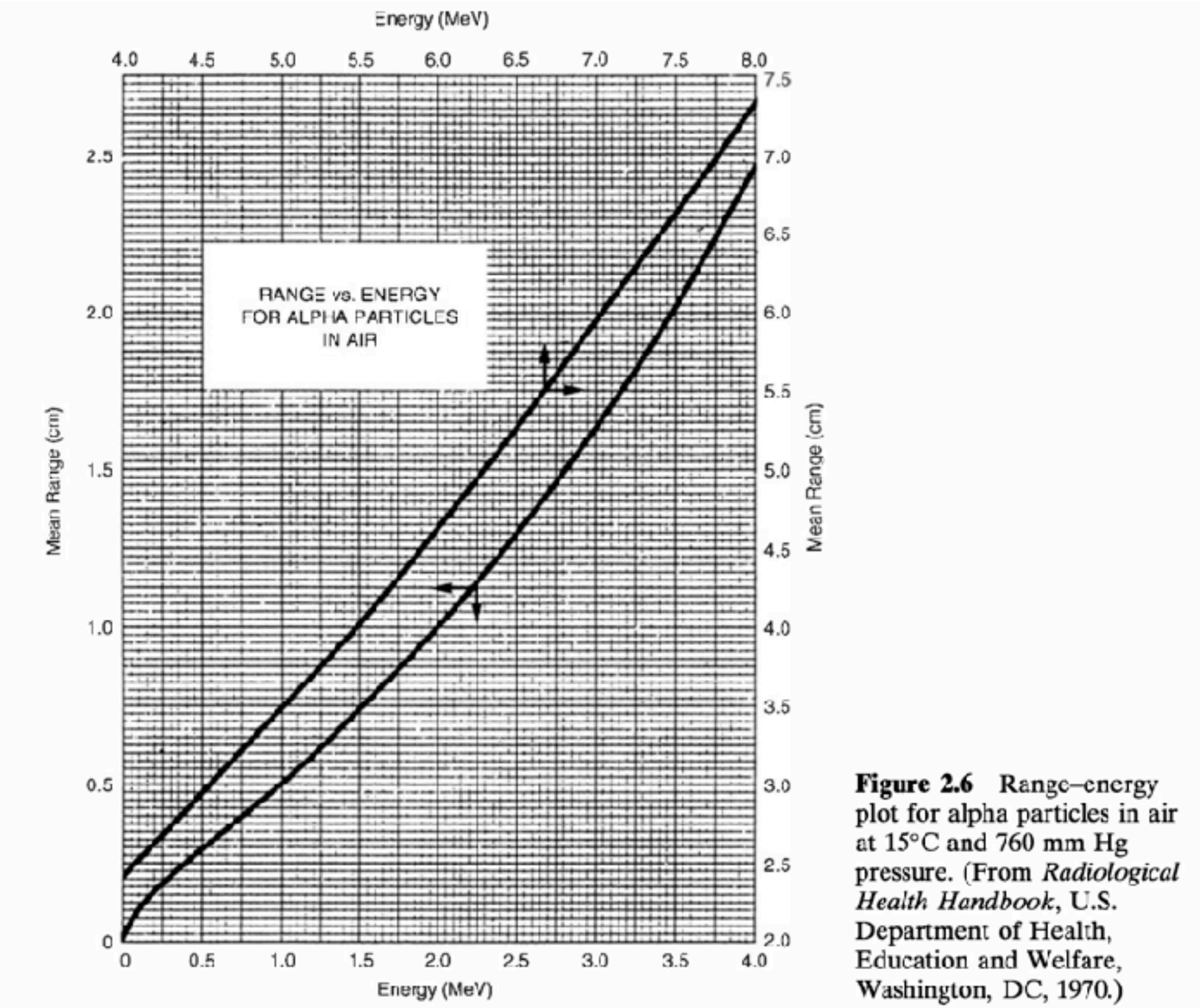

Figure 2.6 Range–energy plot for alpha particles in air at 15°C and 760 mm Hg pressure. (From *Radiological Health Handbook*, U.S. Department of Health, Education and Welfare, Washington, DC, 1970.)

Radiation Interactions

Range

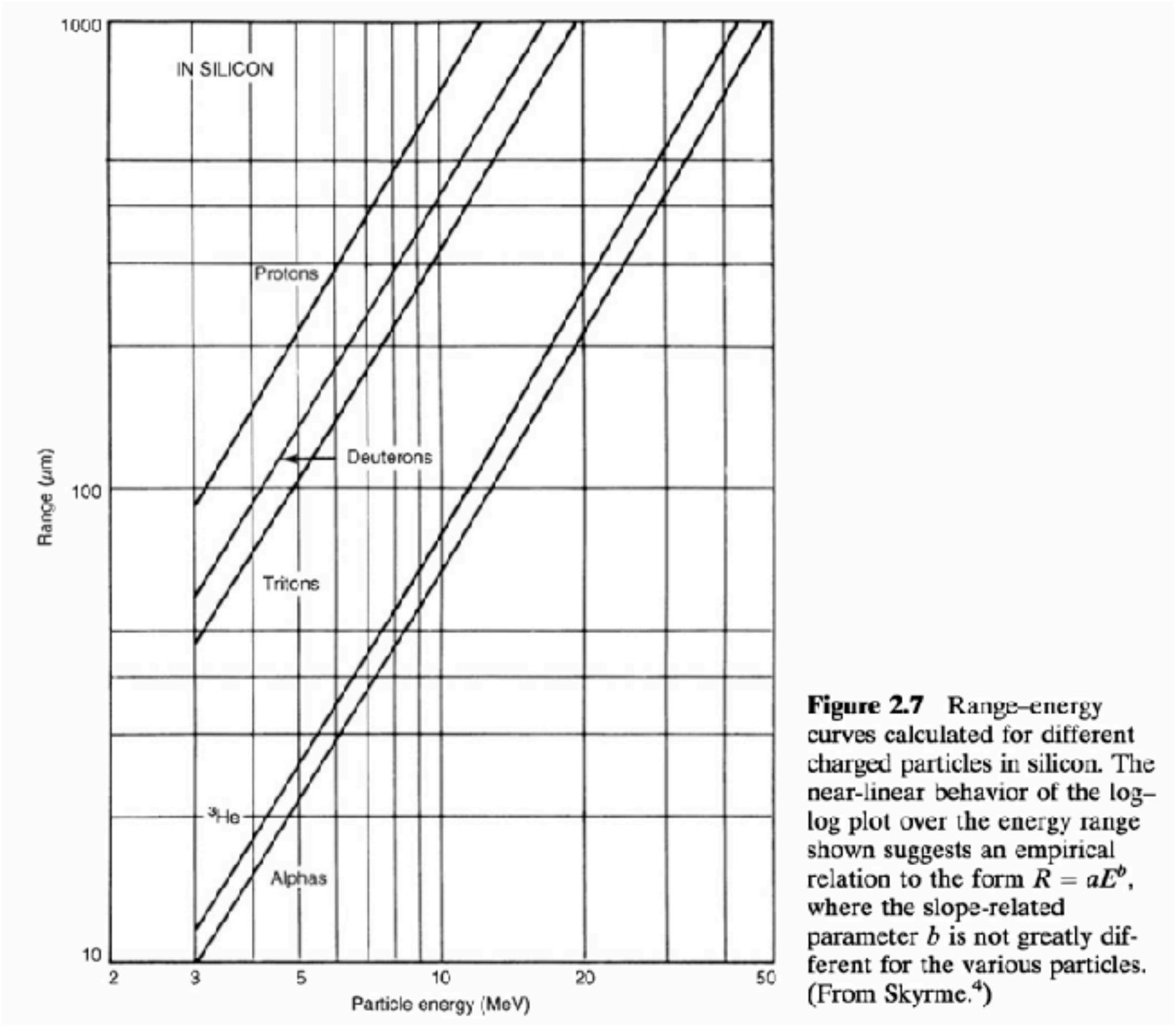

Figure 2.7 Range–energy curves calculated for different charged particles in silicon. The near-linear behavior of the log–log plot over the energy range shown suggests an empirical relation to the form $R = aE^b$, where the slope-related parameter b is not greatly different for the various particles. (From Skyrme.[4])

Radiation Interactions

Range

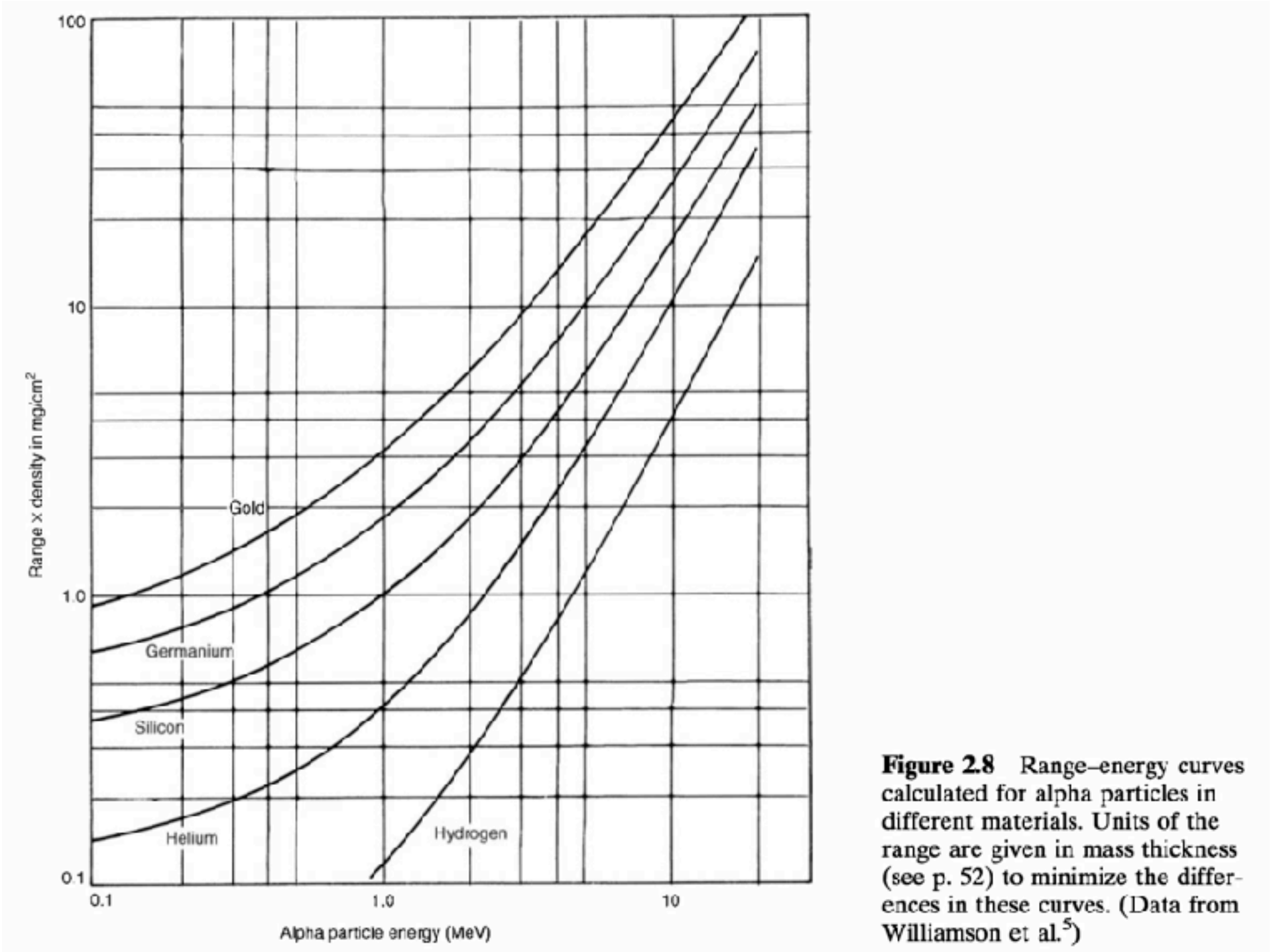

Figure 2.8 Range–energy curves calculated for alpha particles in different materials. Units of the range are given in mass thickness (see p. 52) to minimize the differences in these curves. (Data from Williamson et al.[5])

Radiation Interactions

Specific energy loss

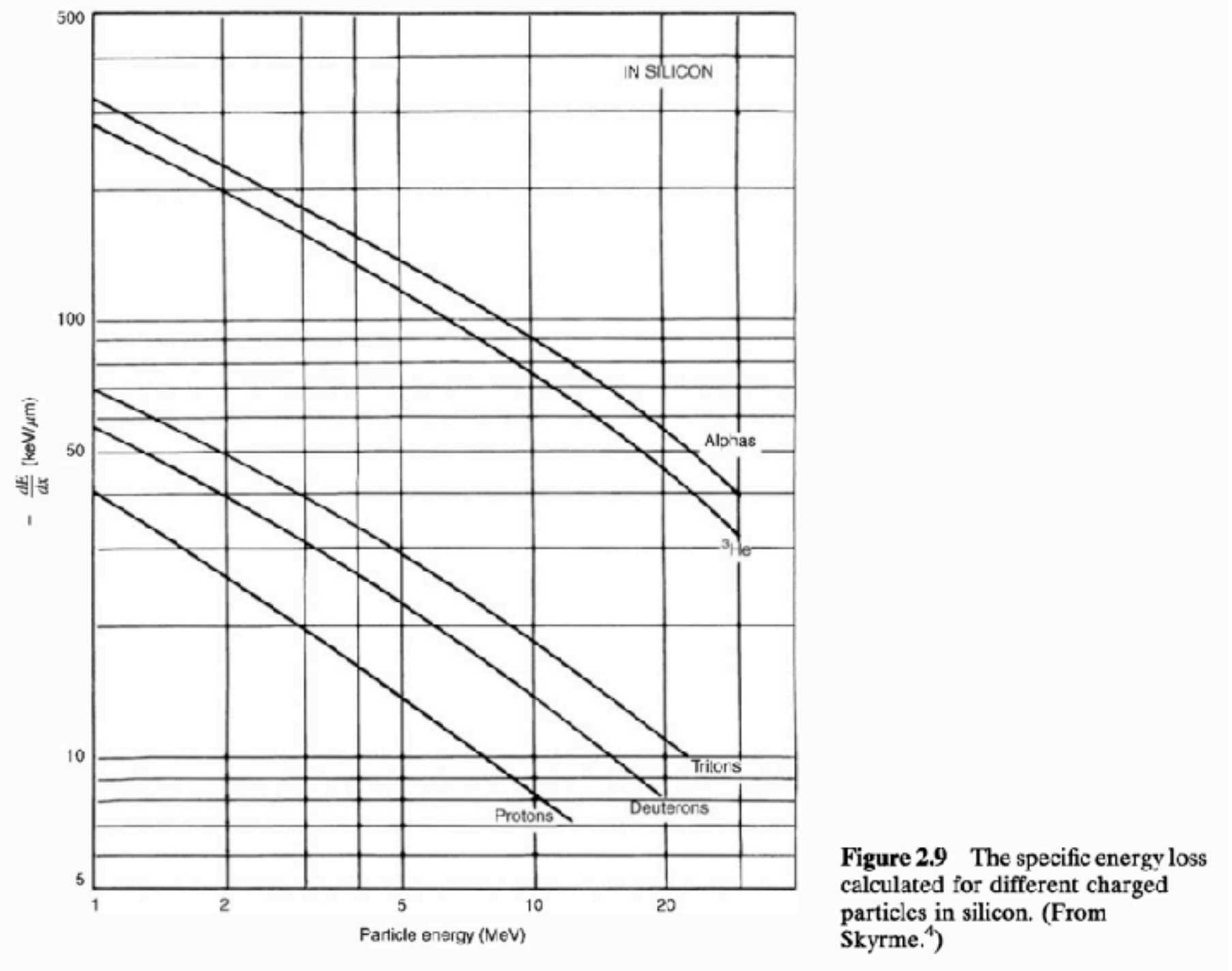

Figure 2.9 The specific energy loss calculated for different charged particles in silicon. (From Skyrme.[4])

Radiation Interactions

Specific energy loss

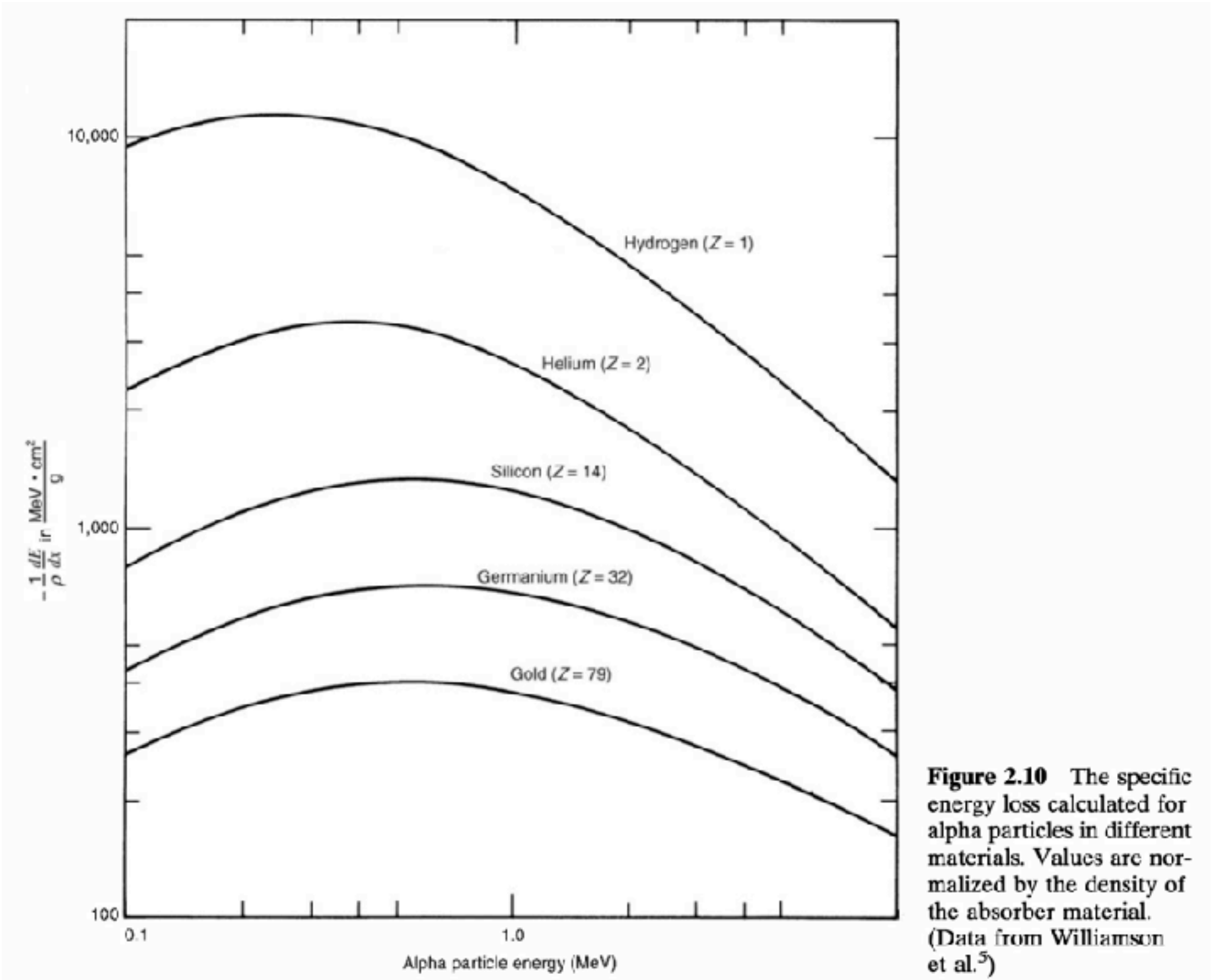

Figure 2.10 The specific energy loss calculated for alpha particles in different materials. Values are normalized by the density of the absorber material. (Data from Williamson et al.[5])

Radiation Interactions

Specific energy loss

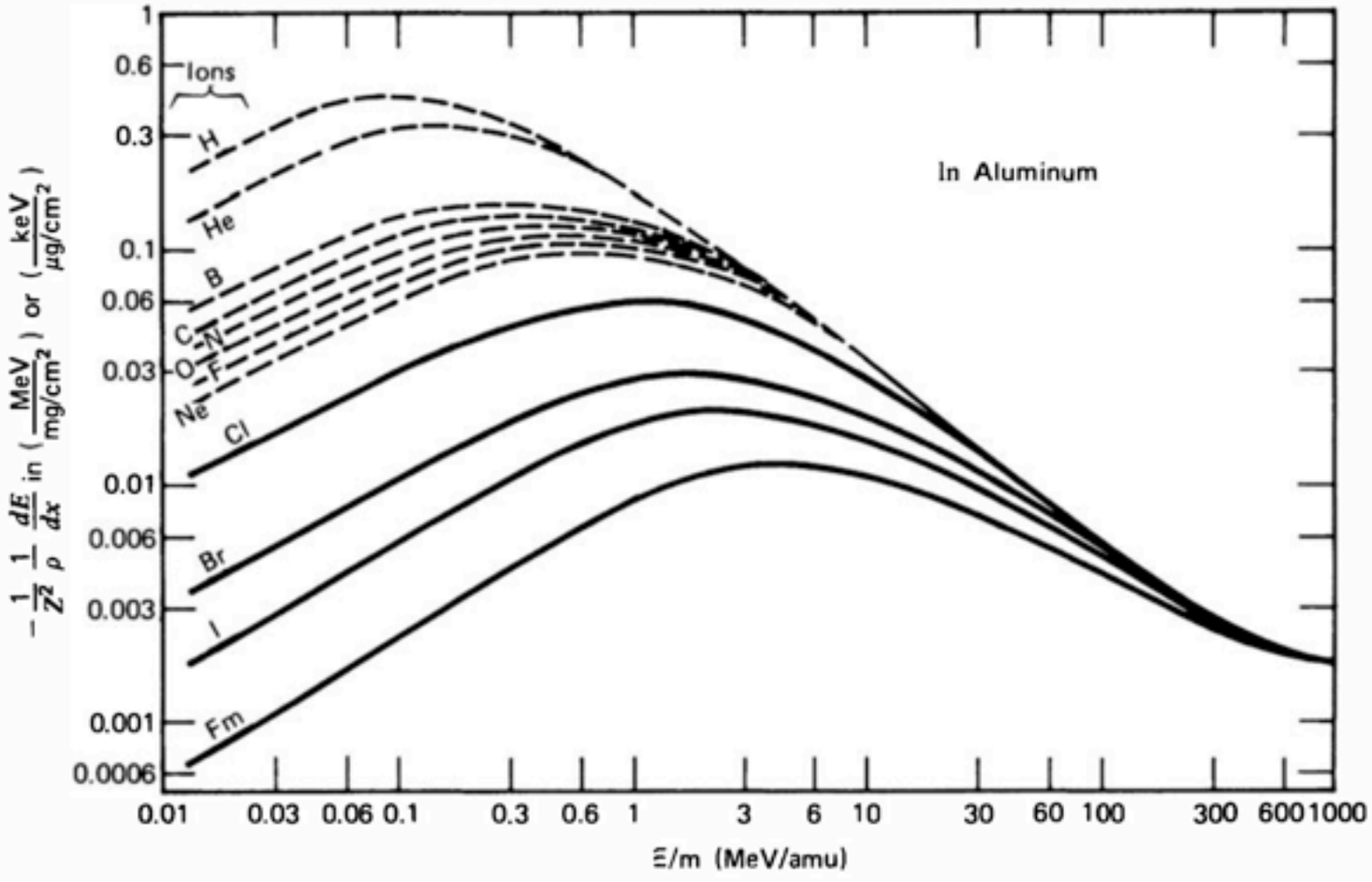

Figure 2.11 Plots showing the specific energy loss of various heavy ions in aluminum. The abscissa is the ion energy divided by its mass, and the ordinate is dE/dx divided by the density of aluminum and the square of the ion atomic number. Typical fission fragments (e.g., iodine) show a continuously decreasing dE/dx while slowing from their initial energy (~1 MeV/amu). (From Northcliffe and Schilling.[8])

Radiation Interactions

Specific energy loss

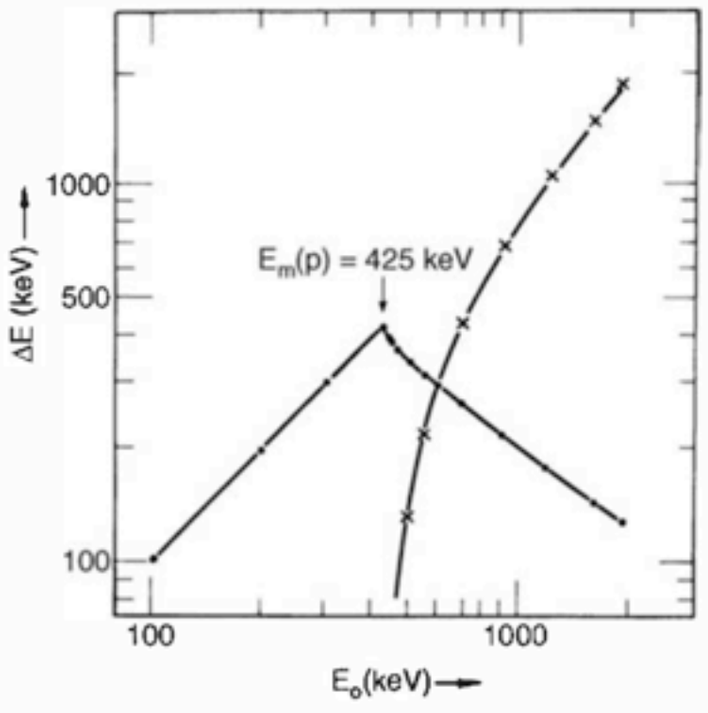

Figure 2.12 Energy loss of protons of initial energy E_0 in a silicon detector of 4.6 μm thickness (shown as dots). The transmitted energy for penetrating protons is also shown (as crosses). (From Wilken and Fritz.[3])

Radiation Interactions

Stopping time

$$v = \sqrt{\frac{2E}{m}} = c\sqrt{\frac{2E}{mc^2}} = \left(3.00 \times 10^8 \frac{\text{m}}{\text{s}}\right)\sqrt{\frac{2E}{(931\ \text{MeV/amu})m_A}}$$

$$T = \frac{R}{\langle v \rangle} = \frac{R}{Kc}\sqrt{\frac{mc^2}{2E}} = \frac{R}{K(3.00 \times 10^8\ \text{m/s})}\sqrt{\frac{931\ \text{MeV/amu}}{2}}\sqrt{\frac{m_A}{E}}$$

Radiation Interactions

Scaling laws : Bragg-Kleeman rule

$$\frac{R_1}{R_0} \cong \frac{\rho_0 \sqrt{A_1}}{\rho_1 \sqrt{A_0}}$$

$$R_a(v) = \frac{m_a {z_b}^2}{m_b {z_a}^2} R_b(v)$$

Radiation Interactions

Fast electron : Specific energy loss

1. Ionization and excitation

$$-\left(\frac{dE}{dx}\right)_c = \frac{2\pi e^4 NZ}{m_0 v^2}\left(\ln\frac{m_0 v^2 E}{2I^2(1-\beta^2)} - (\ln 2)\left(2\sqrt{1-\beta^2} - 1 + \beta^2\right) + (1-\beta^2) + \frac{1}{8}\left(1-\sqrt{1-\beta^2}\right)^2\right)$$

2. Radiative process : Bremstrahlung

$$-\left(\frac{dE}{dx}\right)_r = \frac{NEZ(Z+1)e^4}{137 m_0^2 c^4}\left(4\ln\frac{2E}{m_0 c^2} - \frac{4}{3}\right)$$

3. Total linear stopping power

$$\frac{dE}{dx} = \left(\frac{dE}{dx}\right)_c + \left(\frac{dE}{dx}\right)_r \qquad \frac{(dE/dx)_r}{(dE/dx)_c} \cong \frac{EZ}{700}$$

Radiation Interactions

Fast electron : Absorption

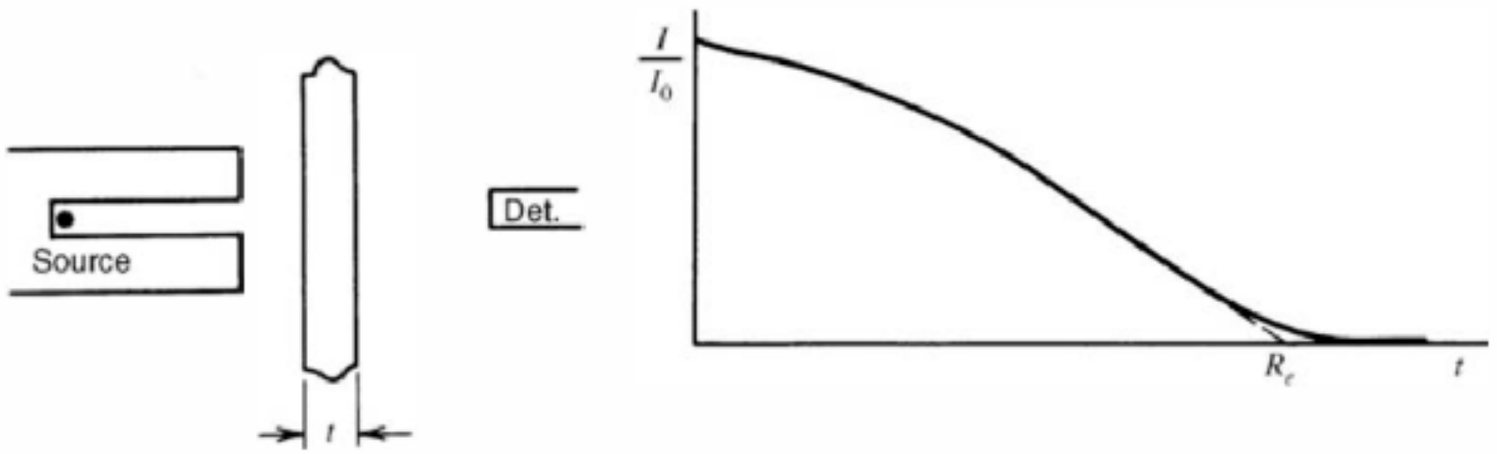

Figure 2.13 Transmission curve for monoenergetic electrons. R_e is the extrapolated range.

$$\frac{I}{I_0} = e^{-nt}$$

I_0 = counting rate without absorber

I = counting rate with absorber

t = absorber thickness g/cm^2

Radiation Interactions

Fast electron : Absorption

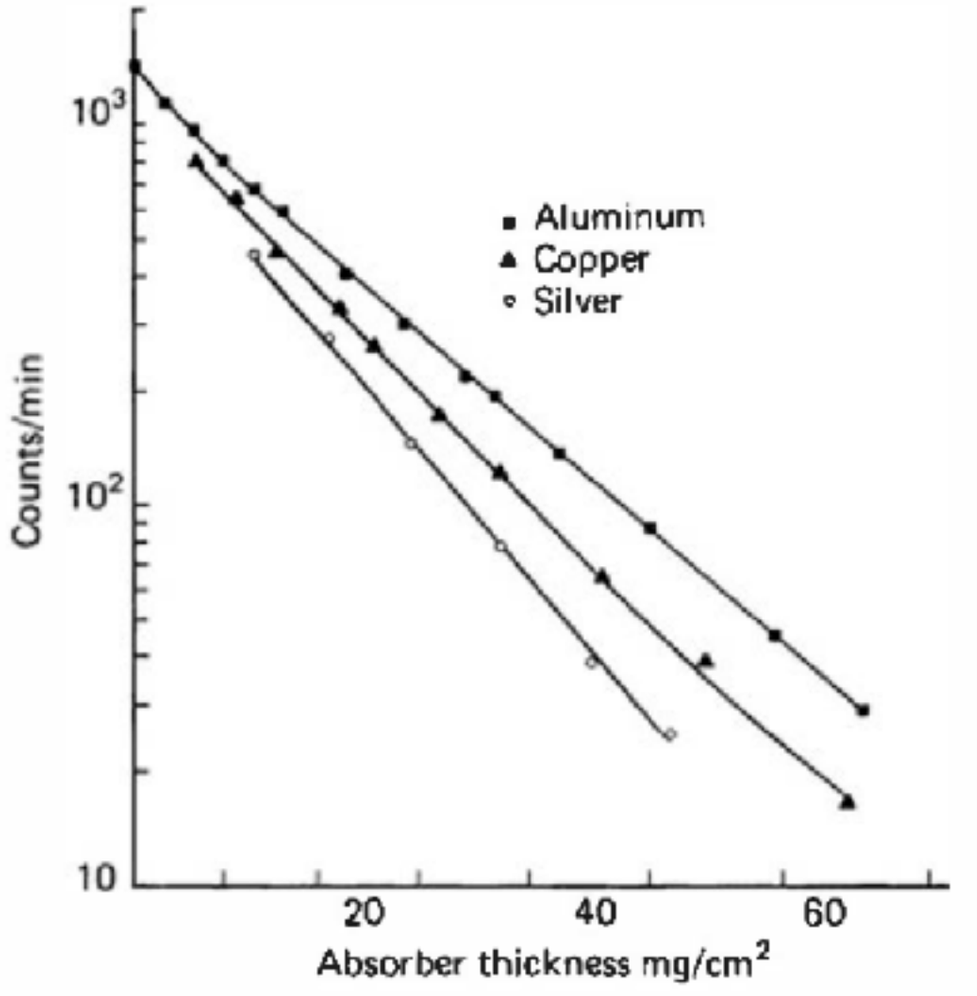

Figure 2.15 Transmission curves for beta particles from ^{185}W (endpoint energy of 0.43 MeV). (From Baltakmens.[26])

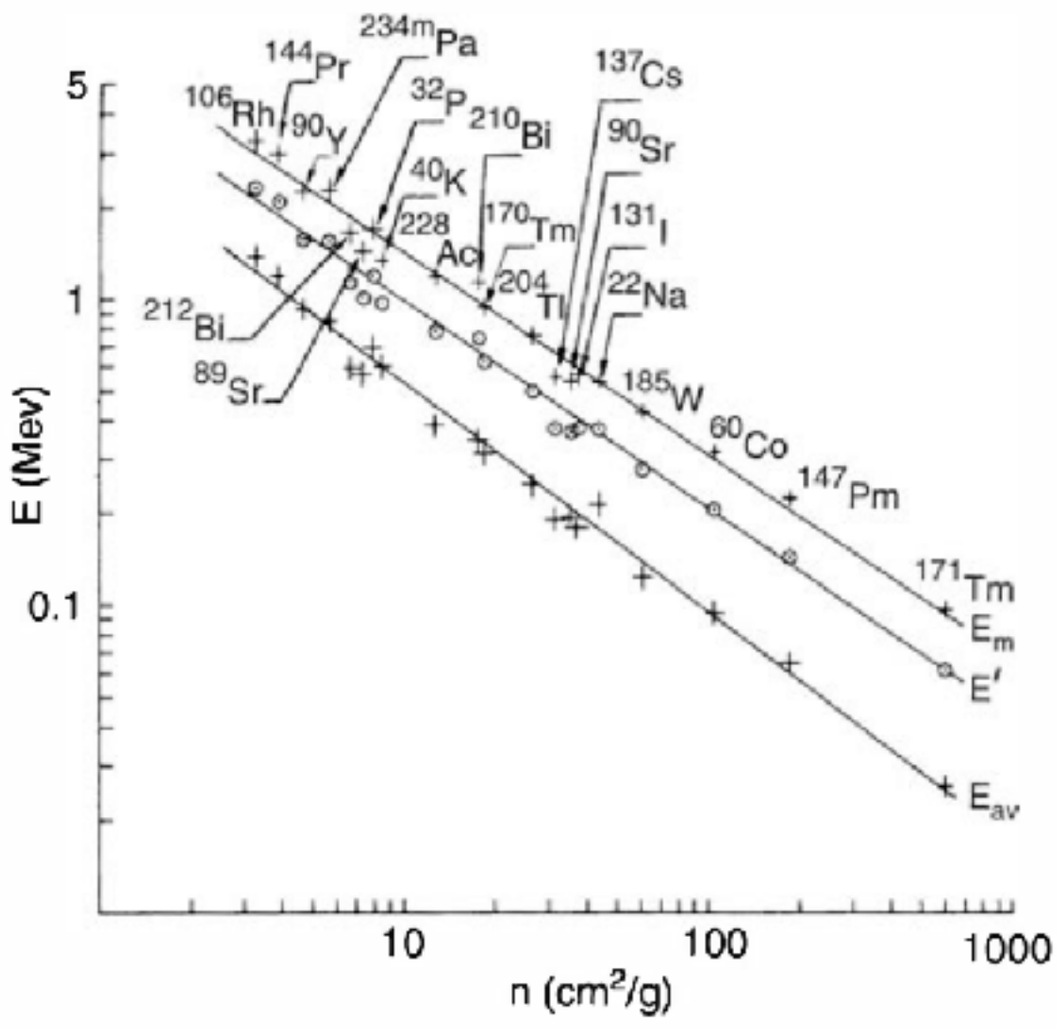

Figure 2.16 Beta particle absorption coefficient n in aluminum as a function of the endpoint energy E_m, average energy E_{av}, and $E' \equiv 0.5\,(E_m + E_{av})$ of different beta emitters. (From Baltakmens.[27])

Radiation Interactions

Positron interaction

Positrons differ significantly, however, in that the annihilation radiation described in Chapter 1 is generated at the end of the positron track. Because these 0.511 MeV photons are very penetrating compared with the range of the positron, they can lead to the deposition of energy far from the original positron track.

Radiation Interactions

Gamma rays interaction

1. Photoelectric absorption
2. Compton scattering
3. Pair production

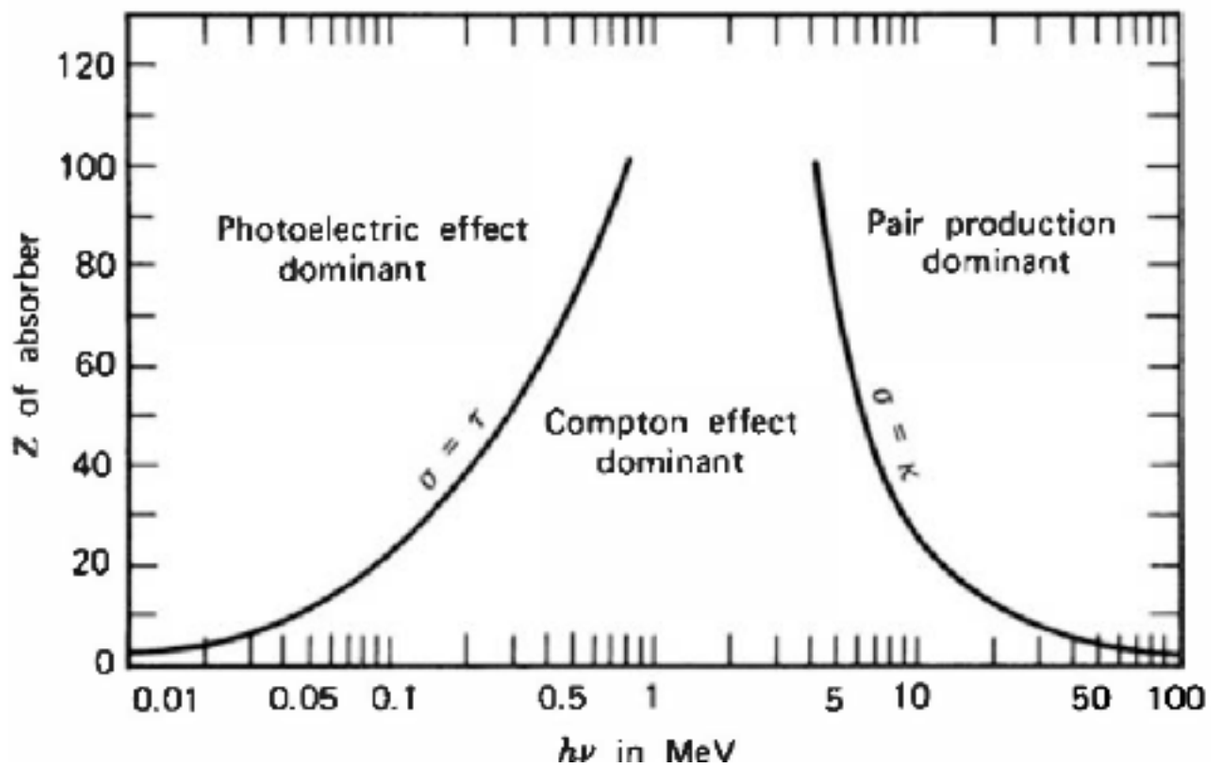

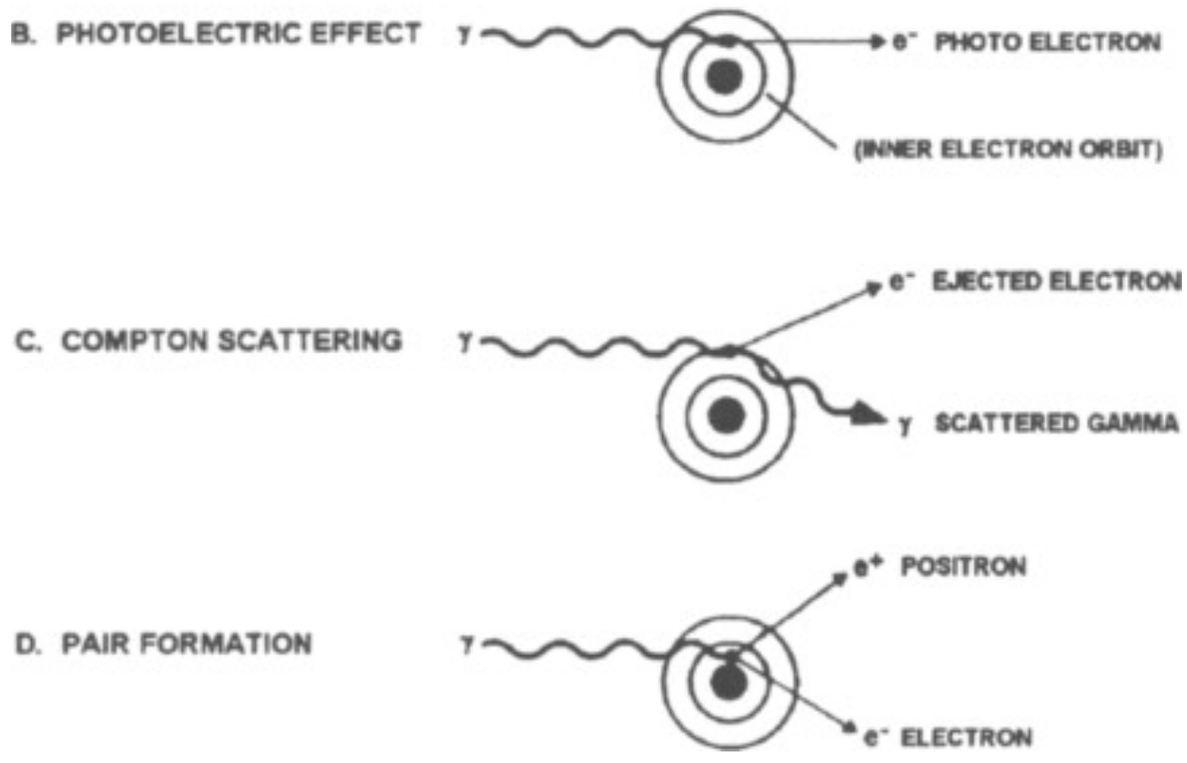

Radiation Interactions

Photoelectric absorption

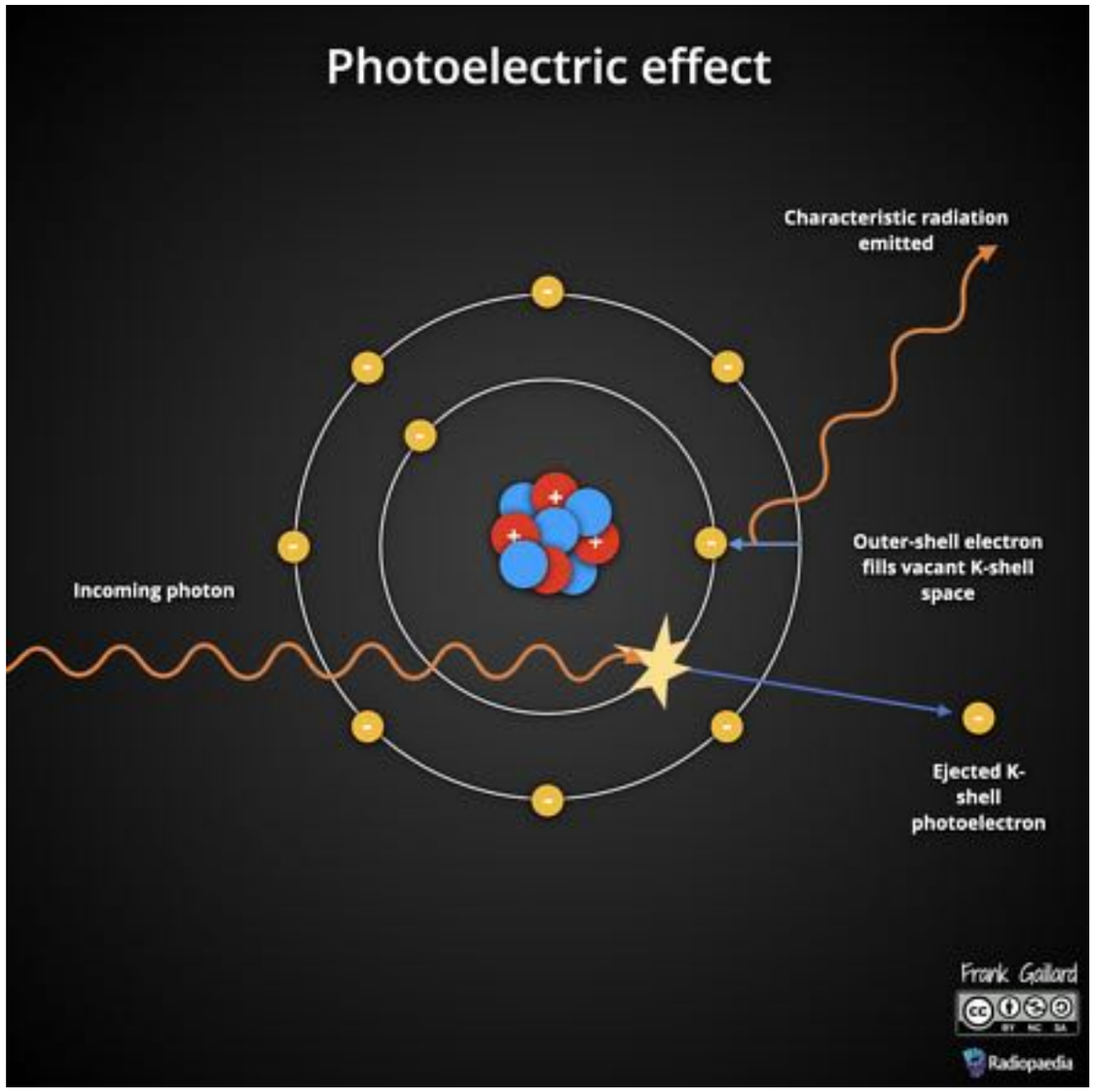

$$E_{e^-} = h\nu - E_b$$

Picture: https://radiopaedia.org/articles/photoelectric-effect

Radiation Interactions

Compton scattering

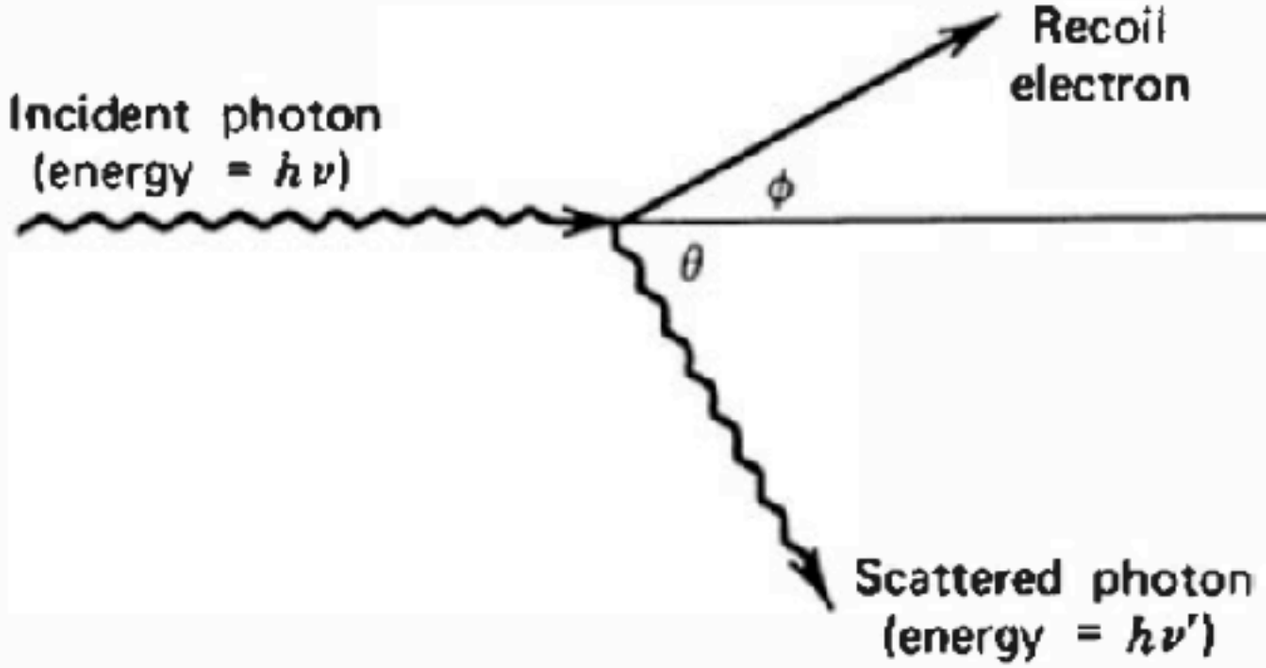

$$h\nu' = \frac{h\nu}{1 + \frac{h\nu}{m_0 c^2}(1 - \cos\theta)}$$

Radiation Interactions

Compton scattering

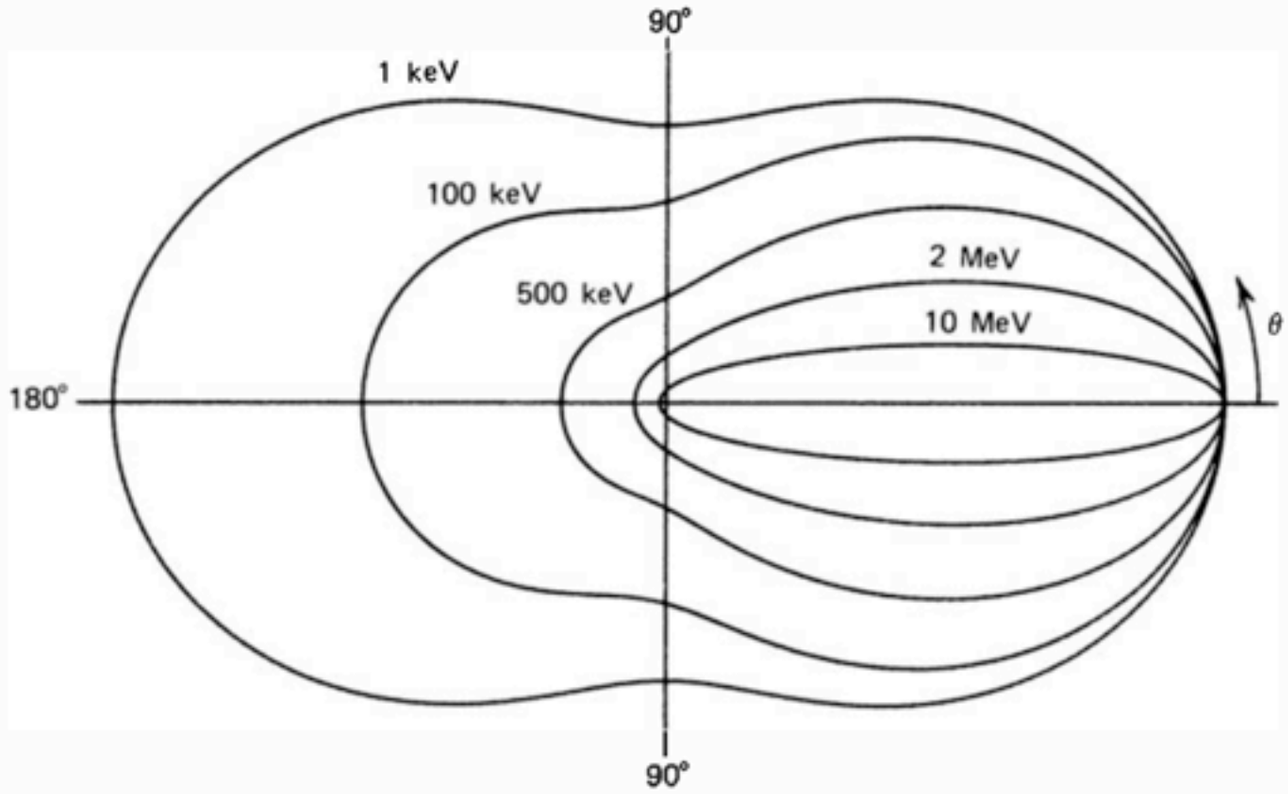

Figure 2.19 A polar plot of the number of photons (incident from the left) Compton scattered into a unit solid angle at the scattering angle θ. The curves are shown for the indicated initial energies.

The angular distribution of scattered gamma rays is predicted by the *Klein–Nishina formula* for the differential scattering cross section $d\sigma/d\Omega$:

$$\frac{d\sigma}{d\Omega} = Zr_0^2\left(\frac{1}{1+\alpha(1-\cos\theta)}\right)^2\left(\frac{1+\cos^2\theta}{2}\right)\left(1+\frac{\alpha^2(1-\cos\theta)^2}{(1+\cos^2\theta)[1+\alpha(1-\cos\theta)]}\right) \qquad (2.18)$$

Radiation Interactions

Pair production

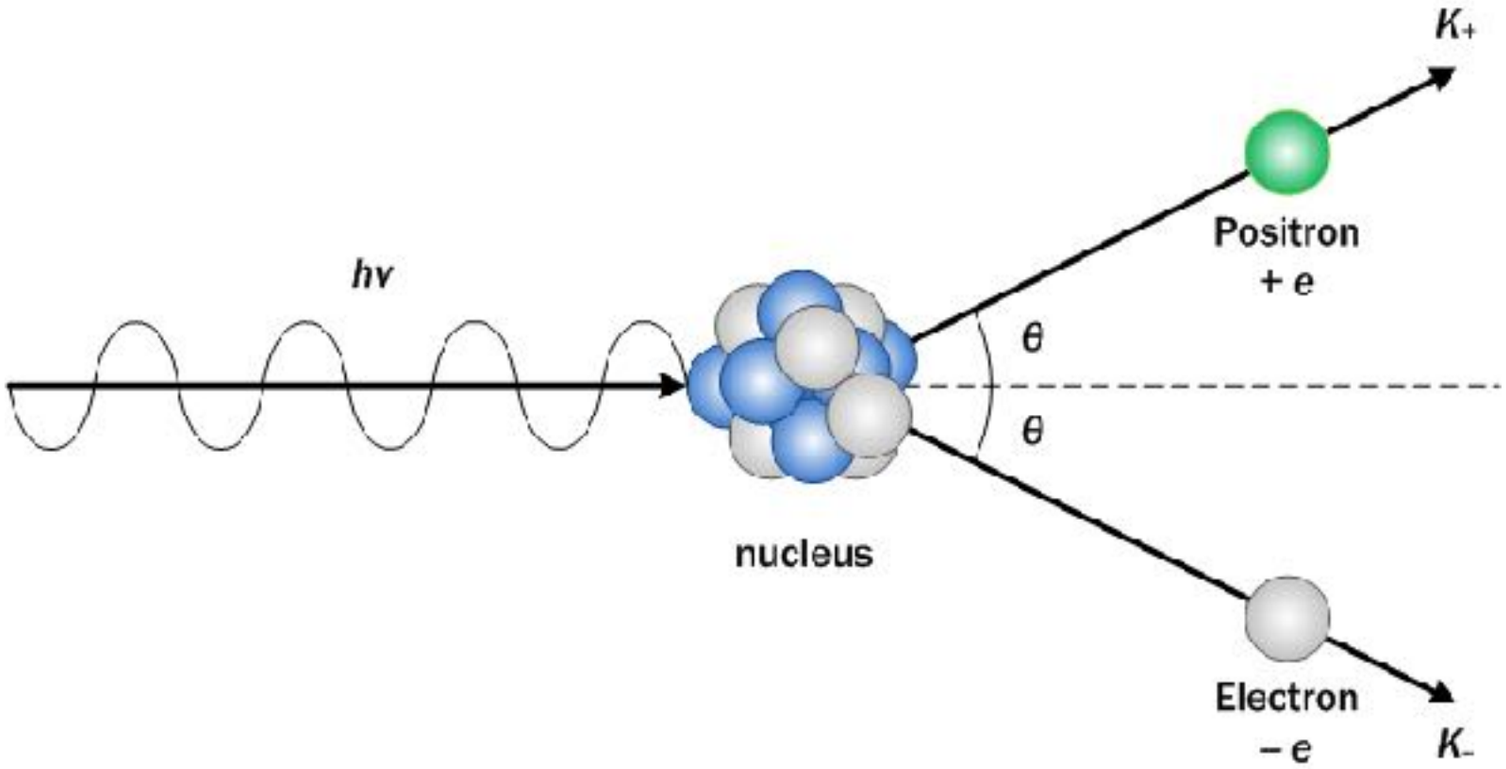

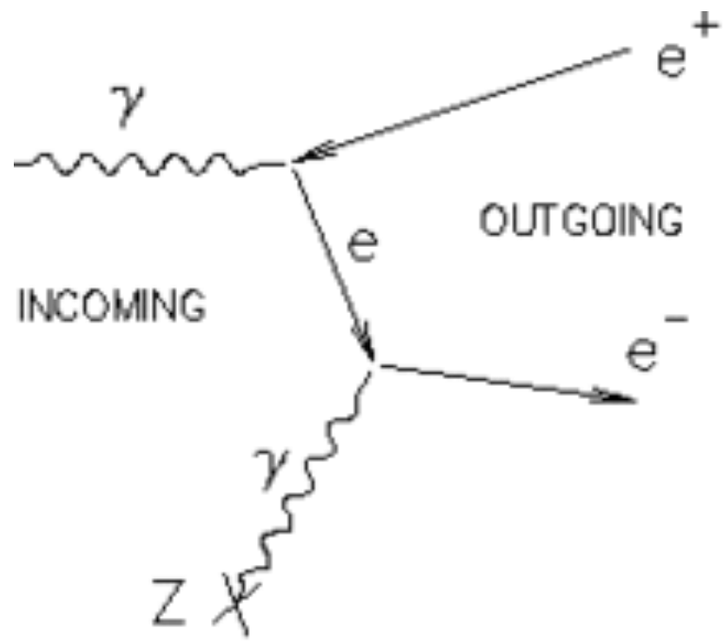

Radiation Interactions

Coherent scattering

In addition to Compton scattering, another type of scattering can occur in which the gamma-ray photon interacts coherently with all the electrons of an absorber atom. This *coherent scattering* or *Rayleigh scattering* process[1] neither excites nor ionizes the atom, and the gamma-ray photon retains its original energy after the scattering event. Because virtually no energy is transferred, this process is often neglected in basic discussions of gamma-ray interactions, and we will also ignore it in the discussions that follow. However, the direction of the photon is changed in coherent scattering, and complete models of gamma-ray transport must take it into account. The probability of coherent scattering is significant only for low photon energies (typically below a few hundred keV for common materials) and is most prominent in high-Z absorbers. The average deflection angle decreases with increasing energy, further restricting the practical importance of coherent scattering to low energies.

Radiation Interactions

Gamma ray attenuation

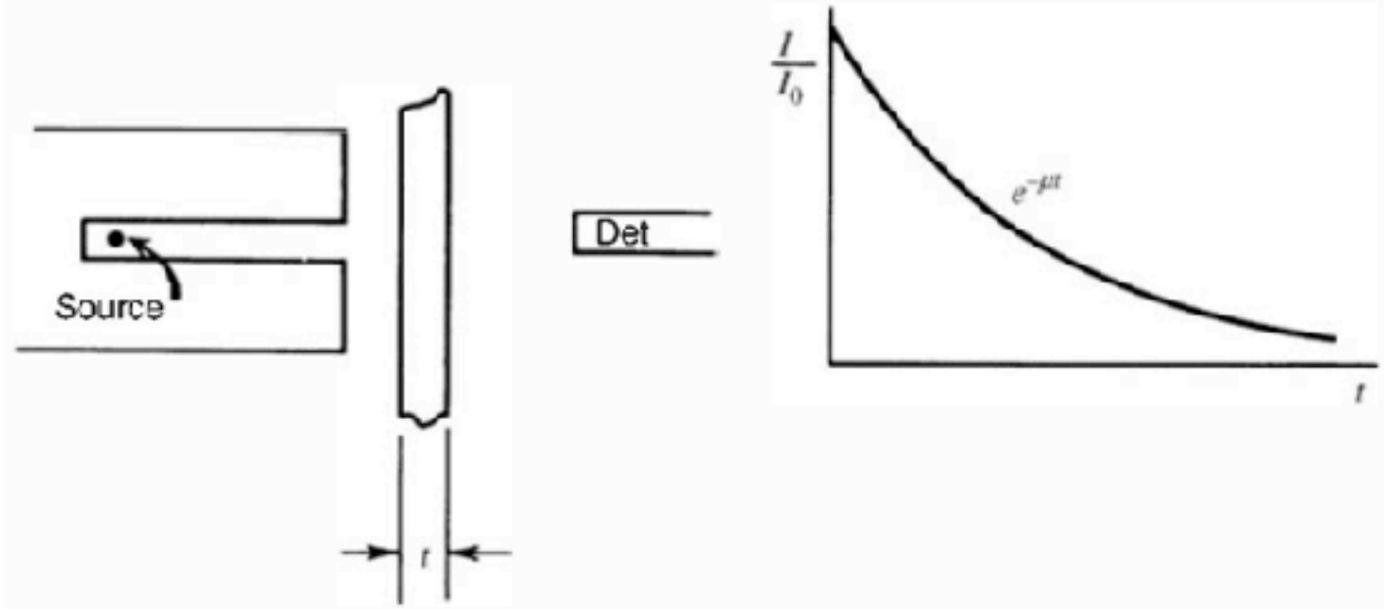

Figure 2.21 The exponential transmission curve for gamma rays measured under "good geometry" conditions.

$$\frac{I}{I_0} = e^{-\mu t}$$

$$\mu = \tau(\text{photoelectric}) + \sigma(\text{Compton}) + \kappa(\text{pair})$$

$$\lambda = \frac{\int_0^\infty x e^{-\mu x} dx}{\int_0^\infty e^{-\mu x} dx} = \frac{1}{\mu}$$

$$\text{mass attenuation coefficient} = \frac{\mu}{\rho}$$

Radiation Interactions

Neutron interaction

1. **Slow neutron** : elastic scattering, neutron-induced nuclear reaction (n,gamma) (n,alpha) (n,p)
2. **Fast neutron** : inelastic scattering, recoil nuclei, hydrogen-rich material to slow down

Radiation Interactions

Exposure and dose

1. **Exposure (X)** = charge due to ionization per mass
   has a unit of **Roentgen (R)** or coulomb per kilogram

$$1\,\mathrm{R} = 2.58 \times 10^{-4}\ \mathrm{C/kg}$$

2. **Absorbed dose (D)** = absorbed energy per mass
   has a unit of **rad = 100 ergs/gram**
   has a unit of **Gray (Gy) = 1 Joule/kg**

$$1\,\mathrm{Gy} = 100\,\mathrm{rad}$$

3. **Dose equivalent (H),** Q=quality factor
   has a unit of **rem** if D in **rad**
   haa a unit of **sievert(Sv)** if D in **Gy**

$$H = DQ$$

Table 2.2 Quality Factors for Different Radiations	
L in Water (keV/μm)	Q
< 10	1
10–100	$0.32L - 2.2$
> 100	$300/\sqrt{L}$

From ICRP.[30]

4. **Effective dose (H_E)**
   h_E = the fluence-to-effective dose conversion
   Phi = fluence = N/(4Pid^2))

$$H_E = h_E \Phi$$

Radiation Interactions

Exposure and dose

5. **ICRP dose** = equivalent dose in an organ ir tissue T due to radiation R

$$H_{T,R} = w_R \cdot D_{T,R}$$

$$H_T = \sum_R H_{T,R} = \sum_R w_R \cdot D_{T,R}$$

The *effective dose E* is defined as the sum over all tissues or organs with *tissue weighting factors* w_T as provided by the ICRP:

$$E = \sum_T w_T \cdot H_T \tag{2.36}$$

Table 2.3 Radiation Weighting Factors

Type and Energy Range		Radiation Weighting Factor, w_R
Photons, all energies		1
Electrons and muons, all energies		1
Neutrons, energy	< 10 keV	5
	10 keV to 100 keV	10
	> 100 keV to 2 MeV	20
	> 2 MeV to 20 MeV	10
	> 20 MeV	5
Protons, other than recoil protons, energy > 2 MeV		5
Alpha particles, fission fragments, heavy nuclei		20

From ICRP.[30]

Ionization Chambers

Ionization Chambers

Ionization process in gases

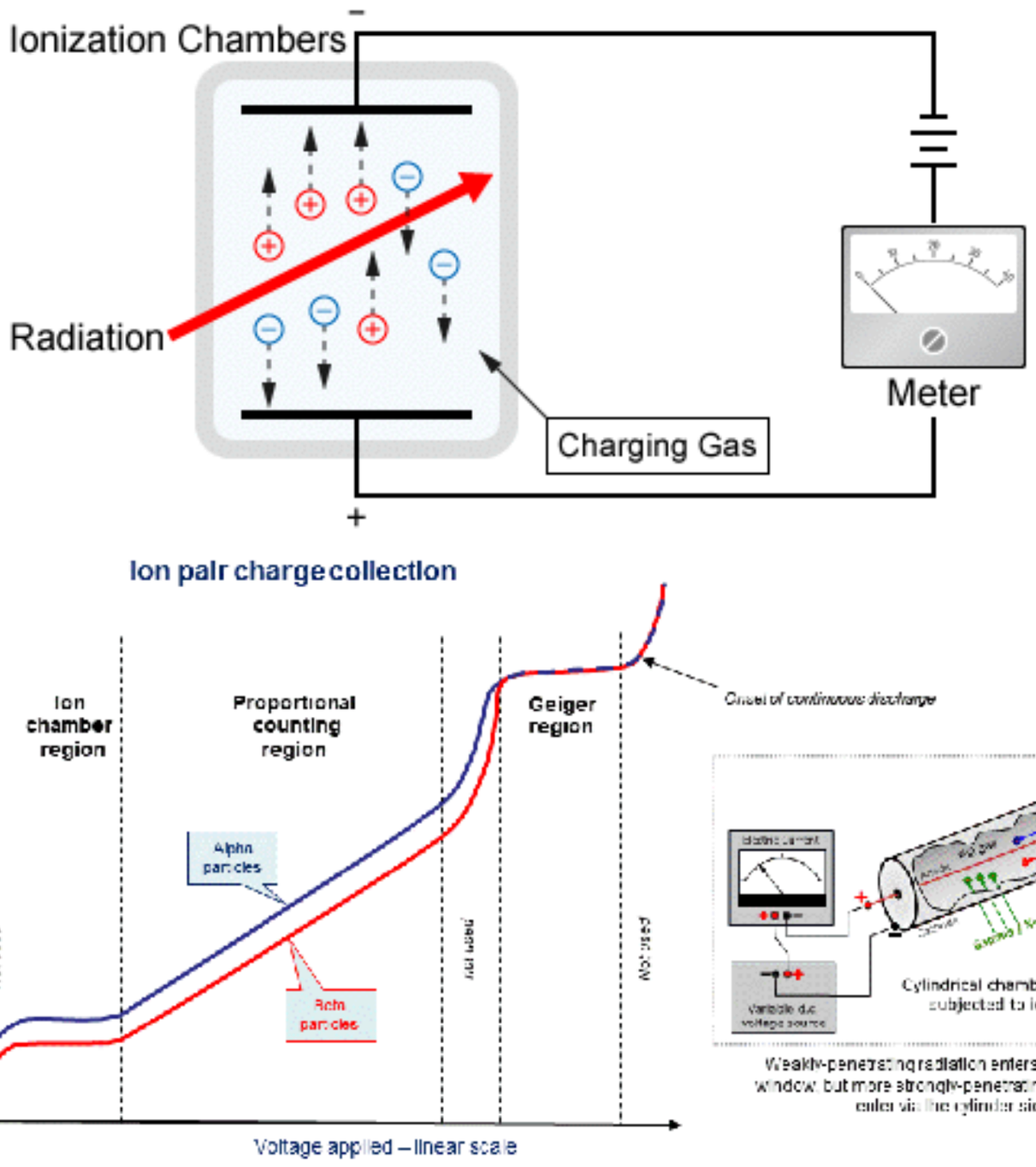

Picture: https://www.matsusada.com/application/ps/ionization_chambers/

Ionization Chambers

Ionization process in gases

Table 5.1 Values of the Energy Dissipation per Ion Pair (the *W*-Value) for Different Gases[a]

Gas	First Ionization Potential (eV)	*W*-Value (eV/ion pair)	
		Fast Electrons	Alpha Particles
Ar	15.7	26.4	26.3
He	24.5	41.3	42.7
H_2	15.6	36.5	36.4
N_2	15.5	34.8	36.4
Air		33.8	35.1
O_2	12.5	30.8	32.2
CH_4	14.5	27.3	29.1

[a]Values for *W* from ICRU Report 31, "Average Energy Required to Produce an Ion Pair," International Commission on Radiation Units and Measurements, Washington, DC, 1979.

Ionization Chambers

Diffusion, Charge transfer, and Recombination

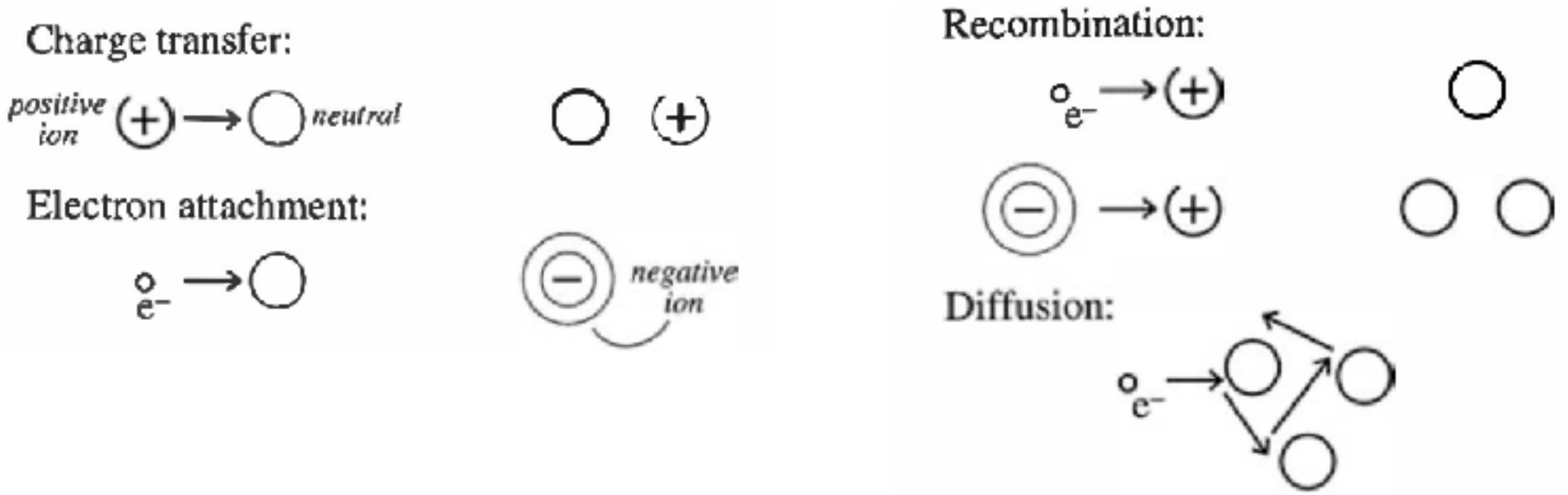

Because the collision frequency is proportional to the product of the concentrations of the two species involved, the recombination rate can be written

$$\frac{dn^+}{dt} = \frac{dn^-}{dt} = -\alpha n^+ n^- \tag{5.2}$$

where
n^+ = number density of positive species
n^- = number density of negative species
α = recombination coefficient

Ionization Chambers

Charge mobility

$$\nu = \frac{\mu \mathscr{E}}{p}$$

ν = drift velocity
$\mathscr{E}$ = electric field strength
p = gas pressure

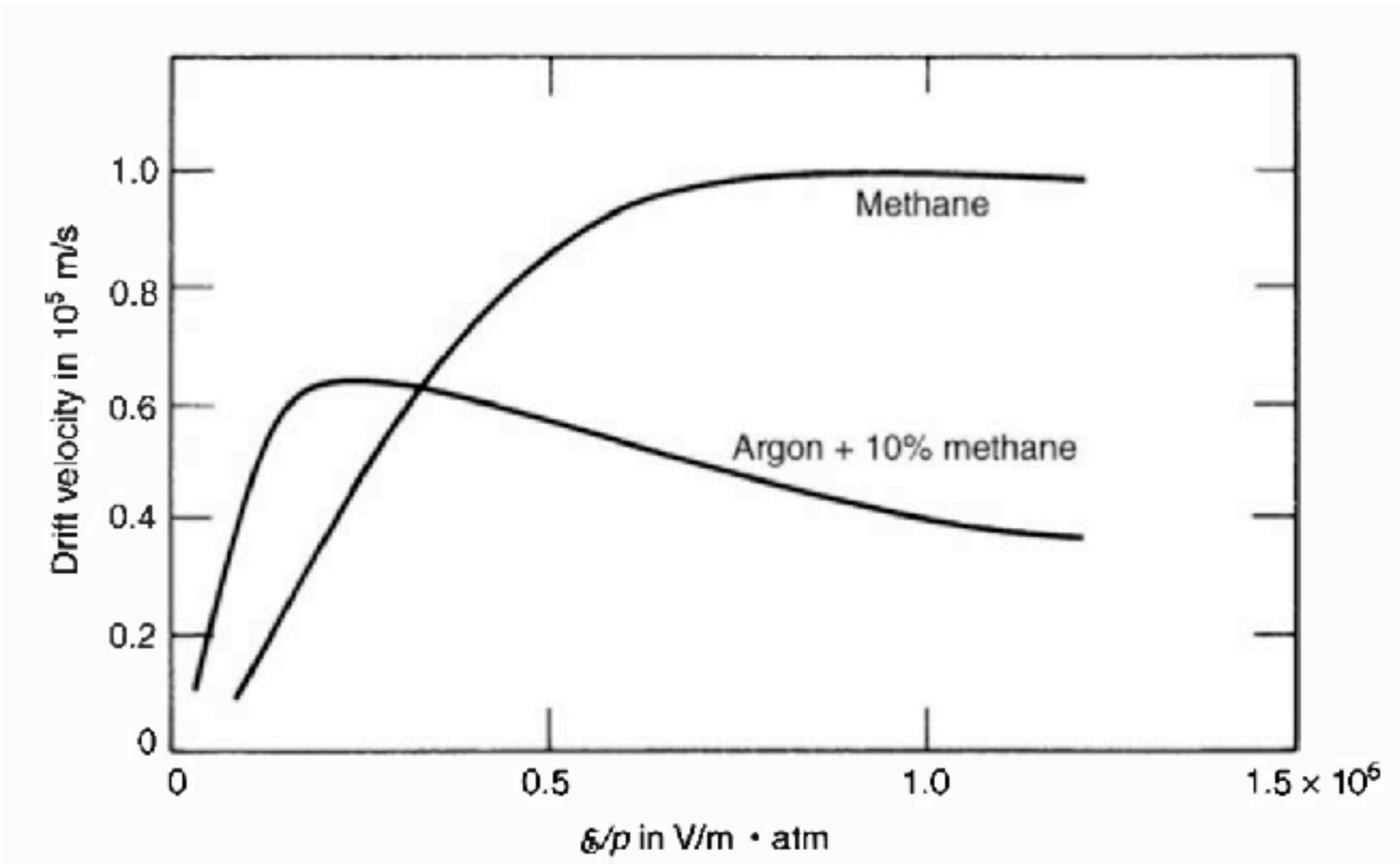

Ionization Chambers

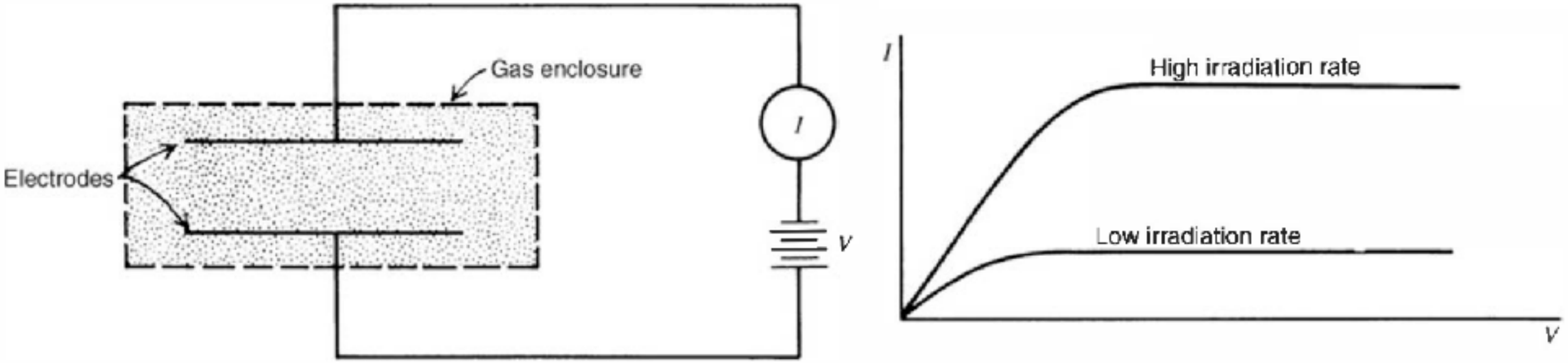

Figure 5.3 The basic components of an ion chamber and the corresponding current–voltage characteristics.

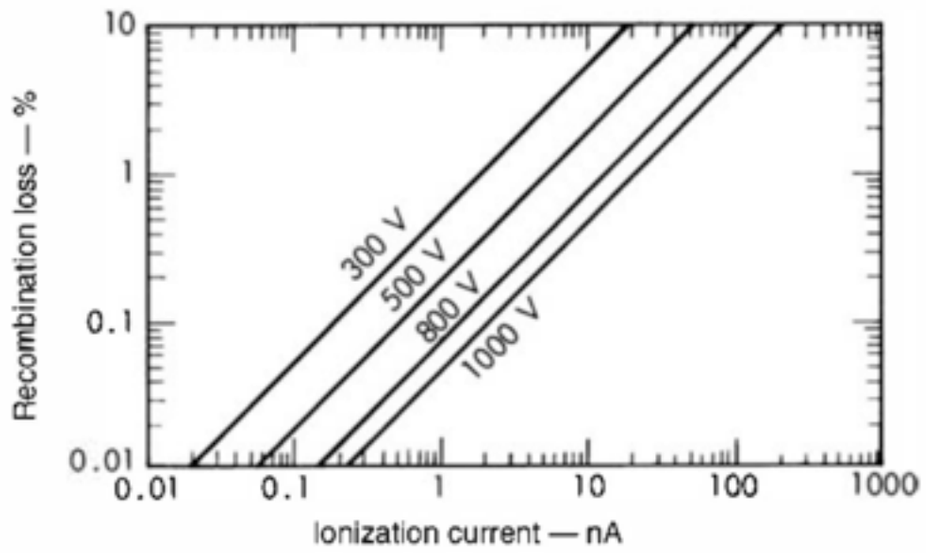

Figure 5.4 Losses due to recombination in an ion chamber filled with argon at 1 atm. These losses are minimized at high values of the applied voltage as shown. (From Colmenares.[9])

Ionization Chambers

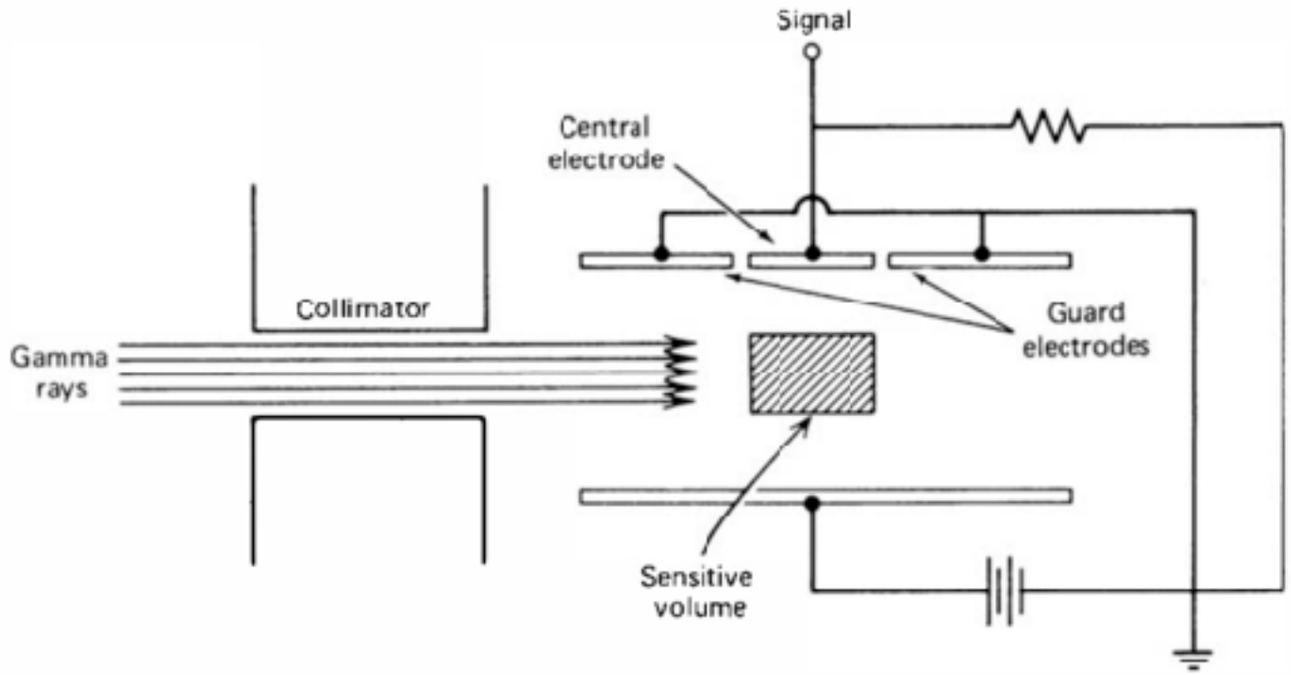

Figure 5.10 The free-air ionization chamber. Because secondary electrons created in the sensitive volume cannot reach the electrodes before stopping, compensation is required only in the dimension parallel to the incident radiation.

$$D_m = WS_mP$$

W = average energy loss per ion pair formed in the gas
S_m = relative mass stopping power (energy loss per unit density) of the material to that of the gas
P = number of ion pairs per unit mass formed in the gas

Ionization Chambers

Applications : Survey meter

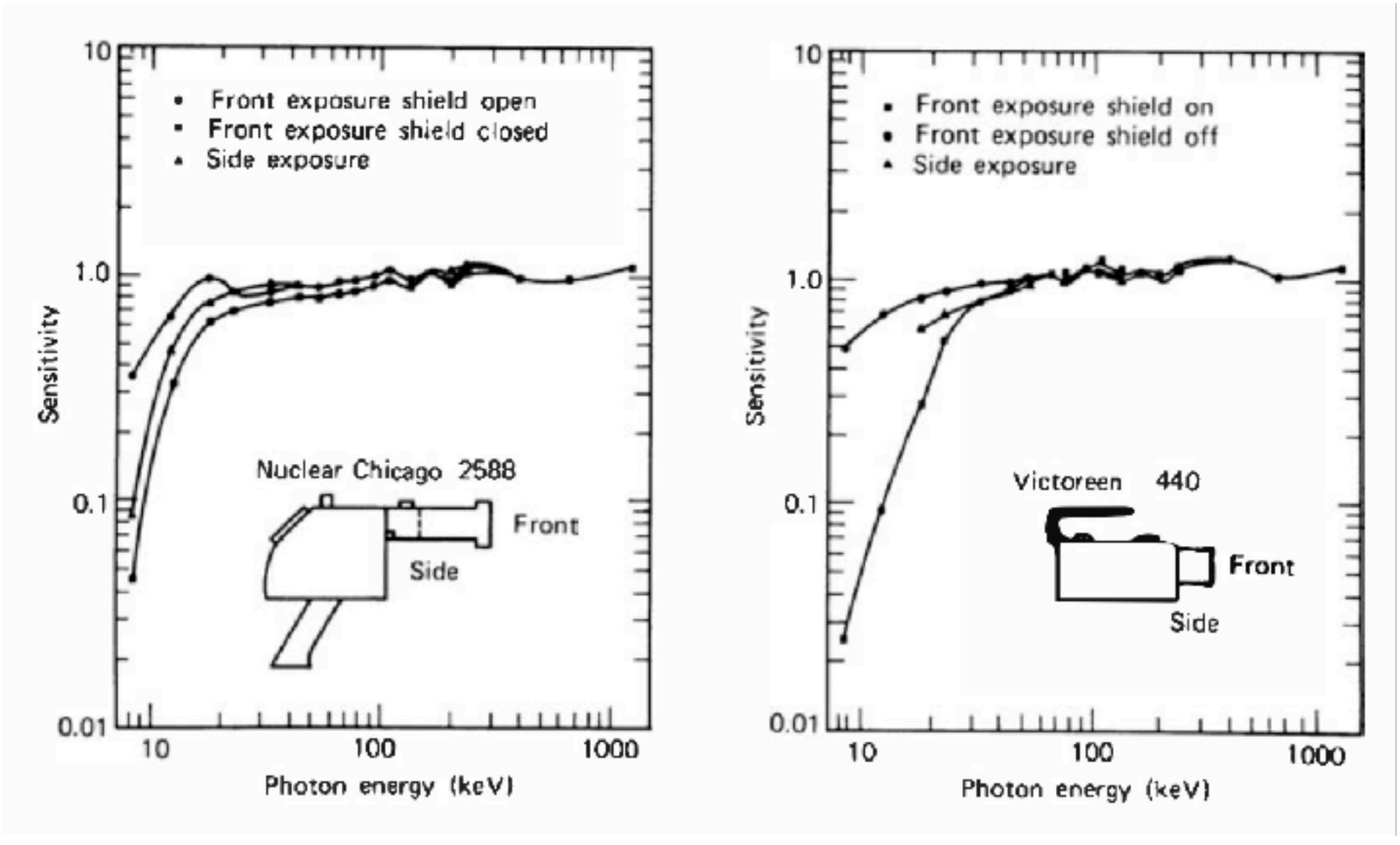

Ionization Chambers

Applications : Calibrator

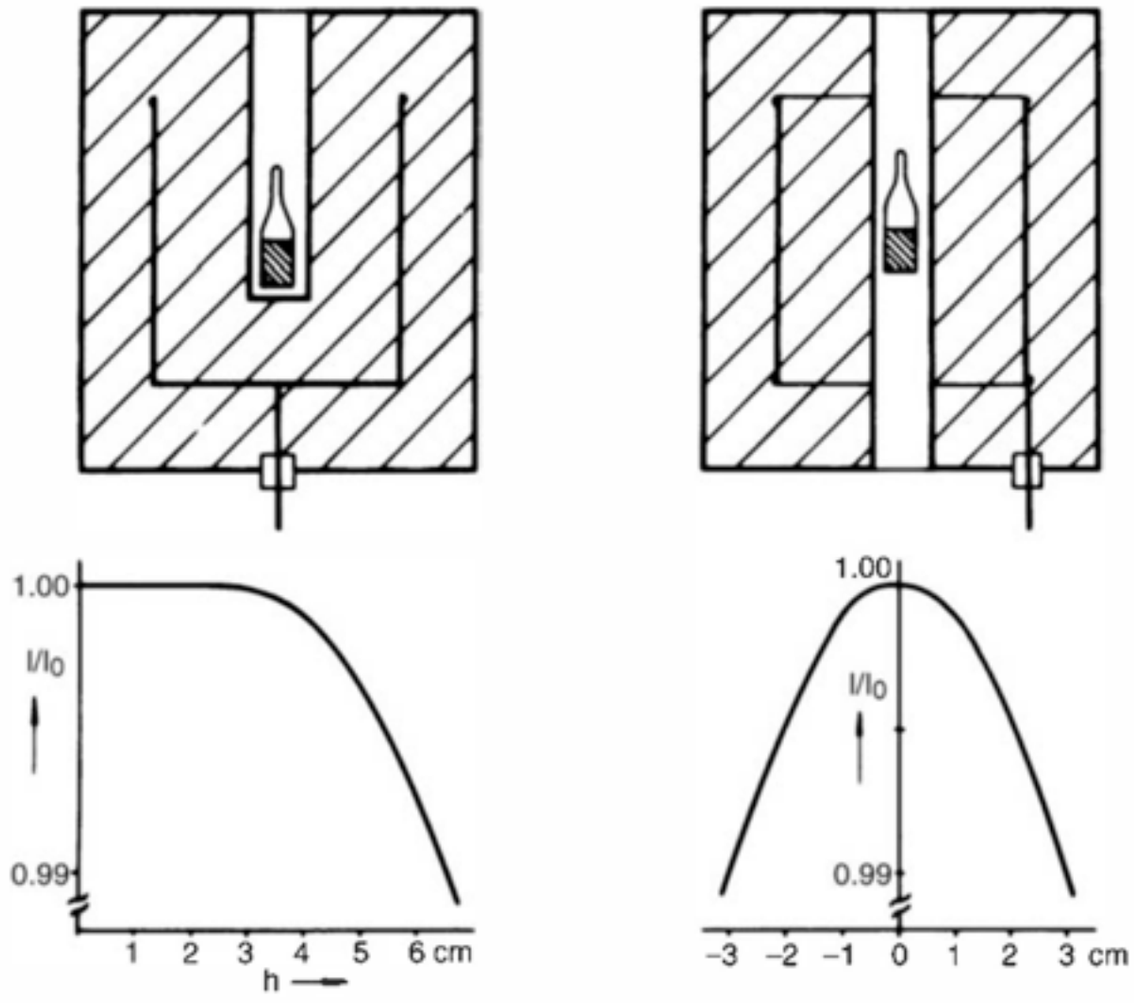

Ionization Chambers

Applications : Measurement of radioactive gases

The ionization current expected from a given quantity of radioactive gas within the chamber is given by

$$I = \frac{\overline{E}\alpha e}{W} \tag{5.12}$$

where
I = ionization current (in A)
$\overline{E}$ = average energy deposited in the gas per disintegration (in eV)
α = total activity (in Bq)
e = electronic charge (in C)
W = average energy deposited per ion pair in the gas (in eV)

Proportional Counters

Proportional Counters

Gas multiplication

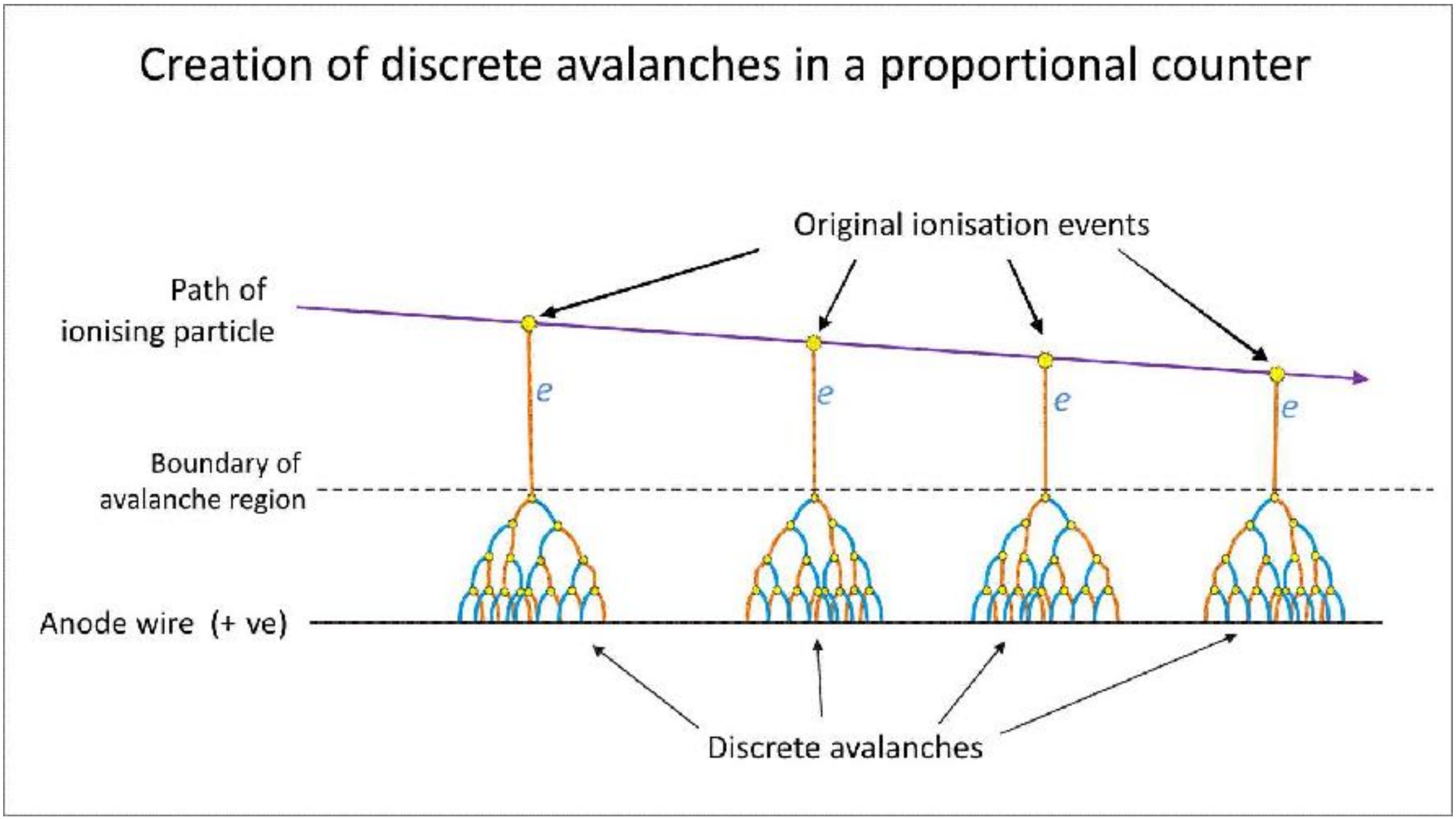

Picture: https://en.wikipedia.org/wiki/Proportional_counter

Proportional Counters

Regions of Detector Operation

Practical Gaseous Ionisation Detector Regions

This shows an idealised plot of the three gaseous detection regions, using the concept of applying a variable voltage to a cylindrical chamber which is subjected to constant ionising radiation. Alpha and beta particles are separately plotted to demonstrate the effect of different radiation energies, but the same principles apply to all forms of ionising radiation.

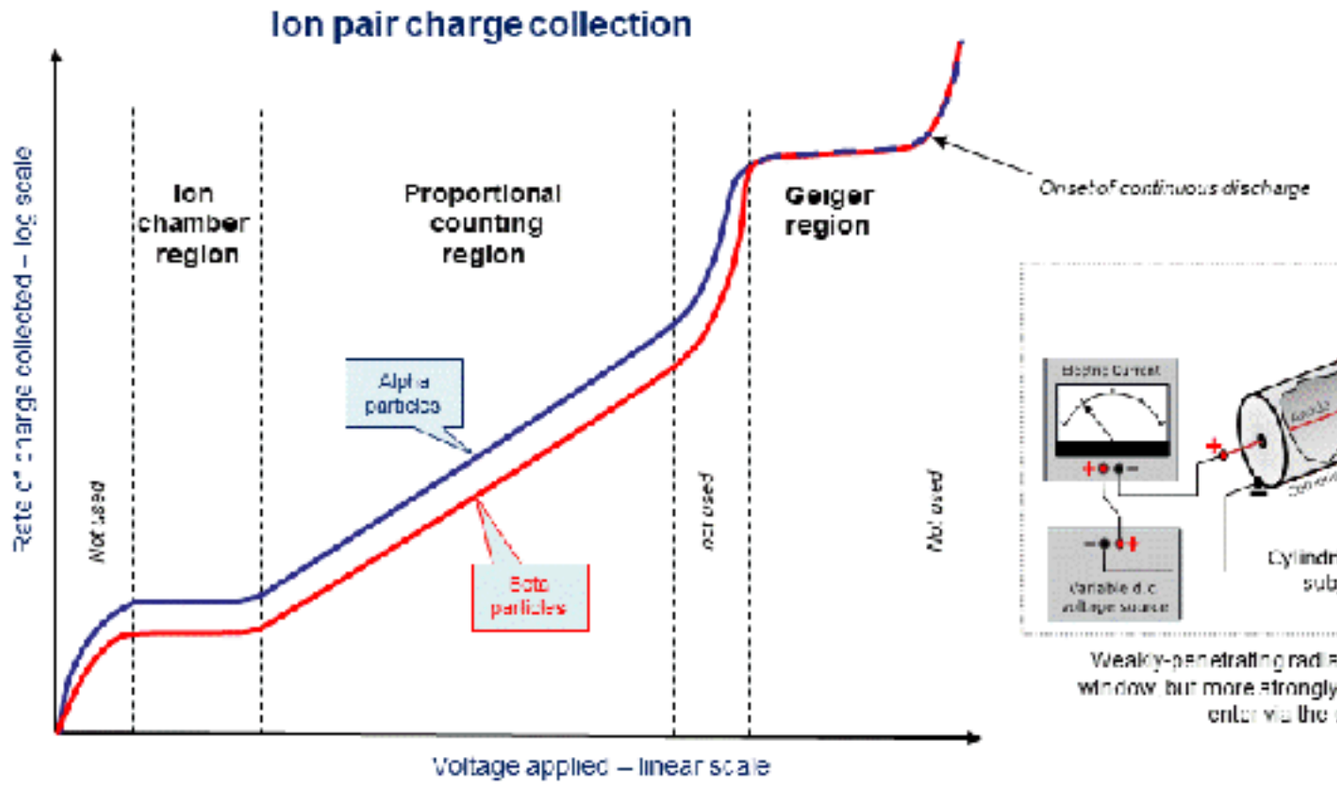

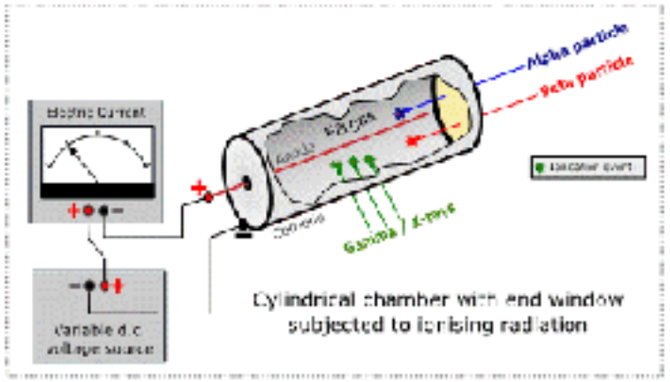

Weakly-penetrating radiation enters via a very thin end window but more strongly-penetrating radiation can also enter via the cylinder side wall.

In the ion chamber region gas ionisation is direct and results in a current flow proportional to overall ionisation. At higher field strengths gas multiplication effects can be used, allowing output of individual ionisation events as measurable pulses.
In the proportional region, pulse sizes are proportional to the energy of each ionisation event. In the Geiger region a fill gas at reduced pressure ($1/10^{th}$ atmosphere) allows greater multiplication but produces a uniform pulse for each ionising event regardless of its energy.

Picture: https://en.wikipedia.org/wiki/Proportional_counter

Proportional Counters

Choice of Geometry

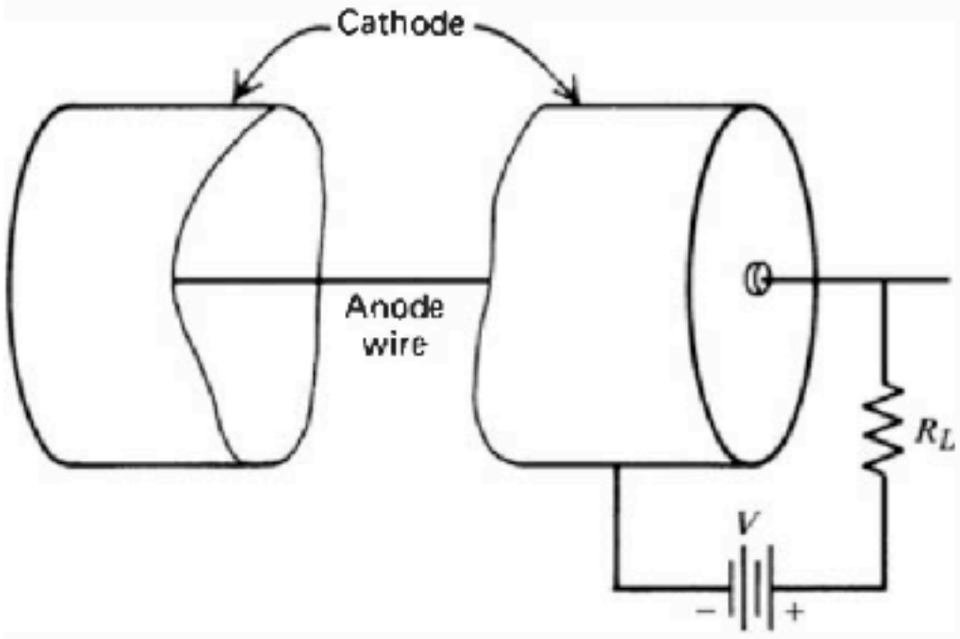

Figure 6.3 Basic elements of a proportional counter. The outer cathode must also provide a vacuum-tight enclosure for the fill gas. The output pulse is developed across the load resistance R_L.

Gas multiplication requires large values of the electric field. In cylindrical geometry, the electric field at a radius r is given by

$$\mathscr{E}(r) = \frac{V}{r \ln(b/a)} \tag{6.3}$$

where

V = voltage applied between anode and cathode

a = anode wire radius

b = cathode inner radius

Proportional Counters

Choice of Geometry

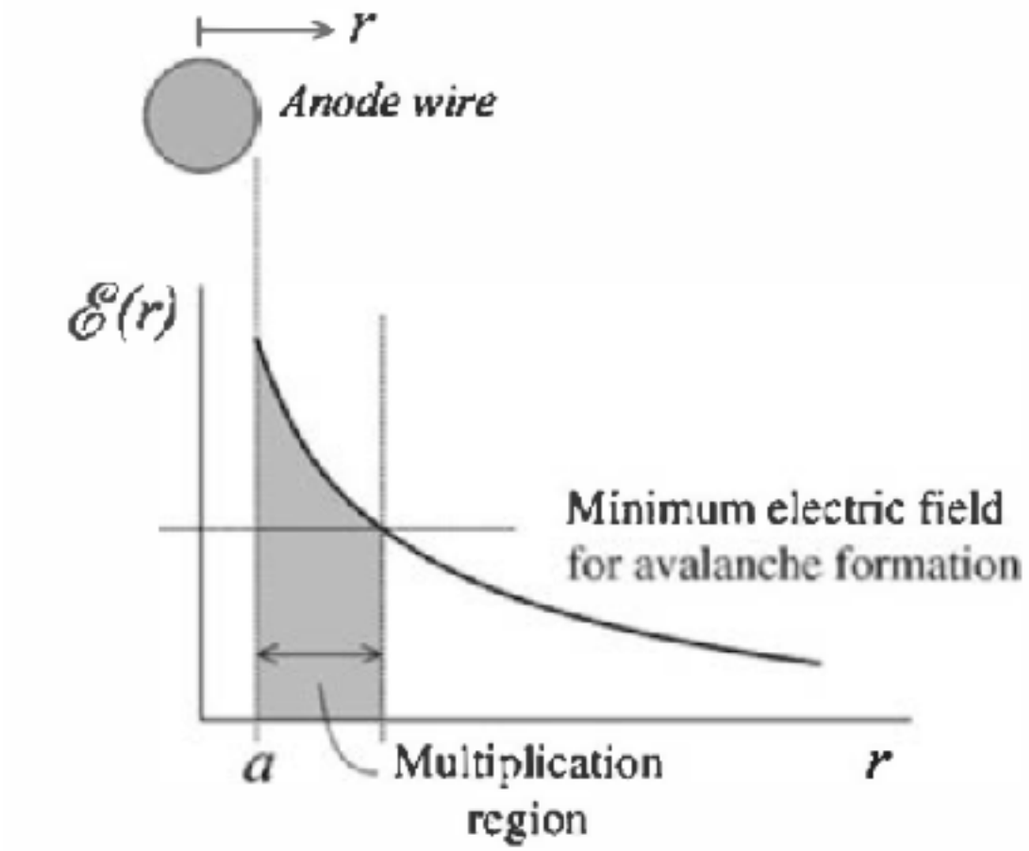

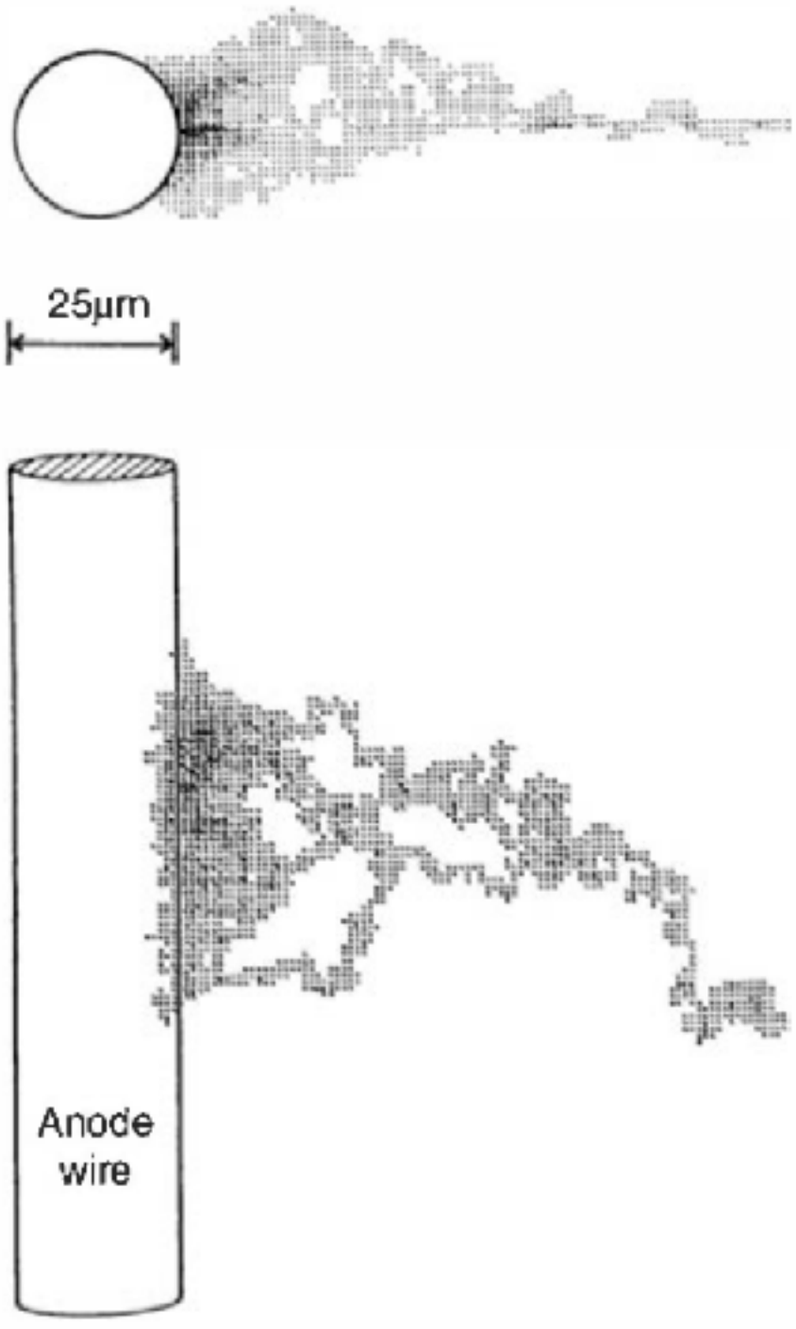

Proportional Counters

Design : Sealed Tubes

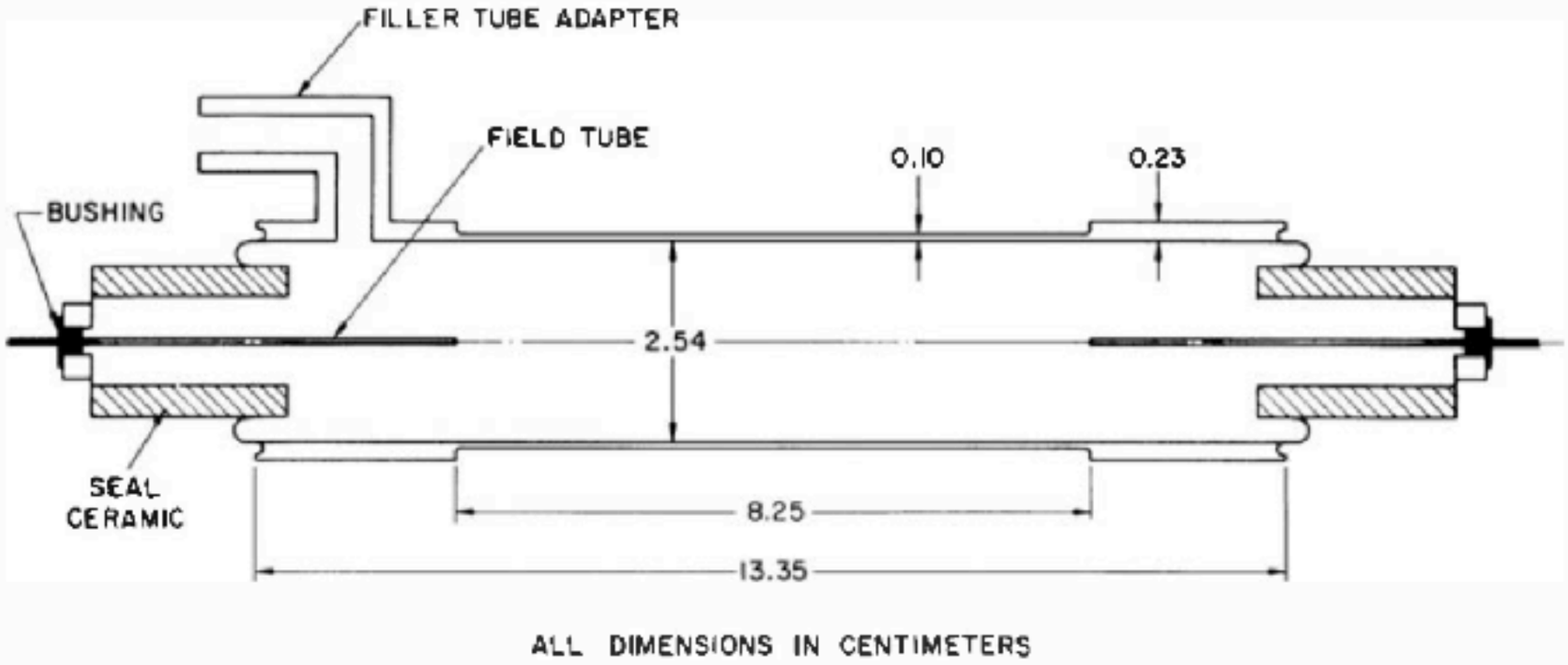

Figure 6.6 Cross-sectional view of a specific proportional tube design used in fast neutron detection. The anode is a 0.025-mm-diameter stainless steel wire. The field tubes consist of 0.25-mm-diameter hypodermic needles fitted around the anode at either end of the tube. (From Bennett and Yule.[4])

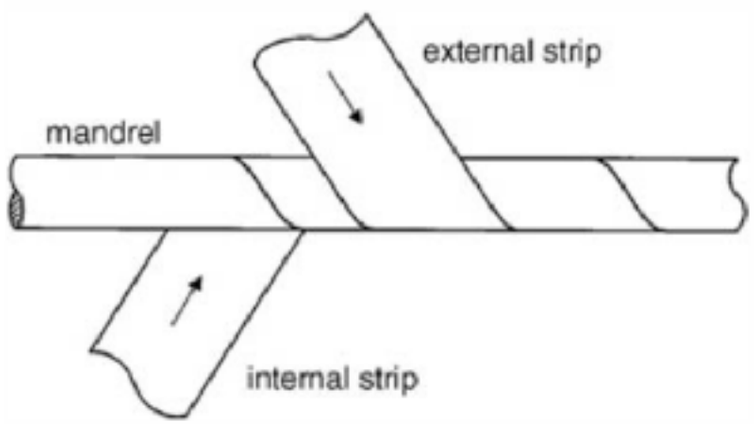

Figure 6.7 The fabrication of a straw tube from two foil strips. Adhesive is used to bind the strips together into a rigid tube. (From Marzec et al.[9])

Proportional Counters

Design : Windowless Flow Counters

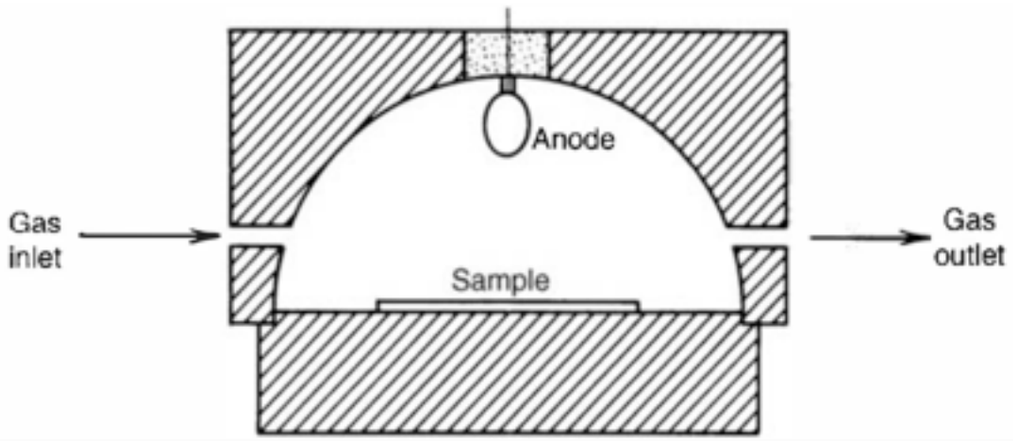

Figure 6.8 Diagram of a 2π gas flow proportional counter with a loop anode wire and hemispherical volume. The sample can often be inserted into the chamber by sliding a tray to minimize the amount of air introduced.

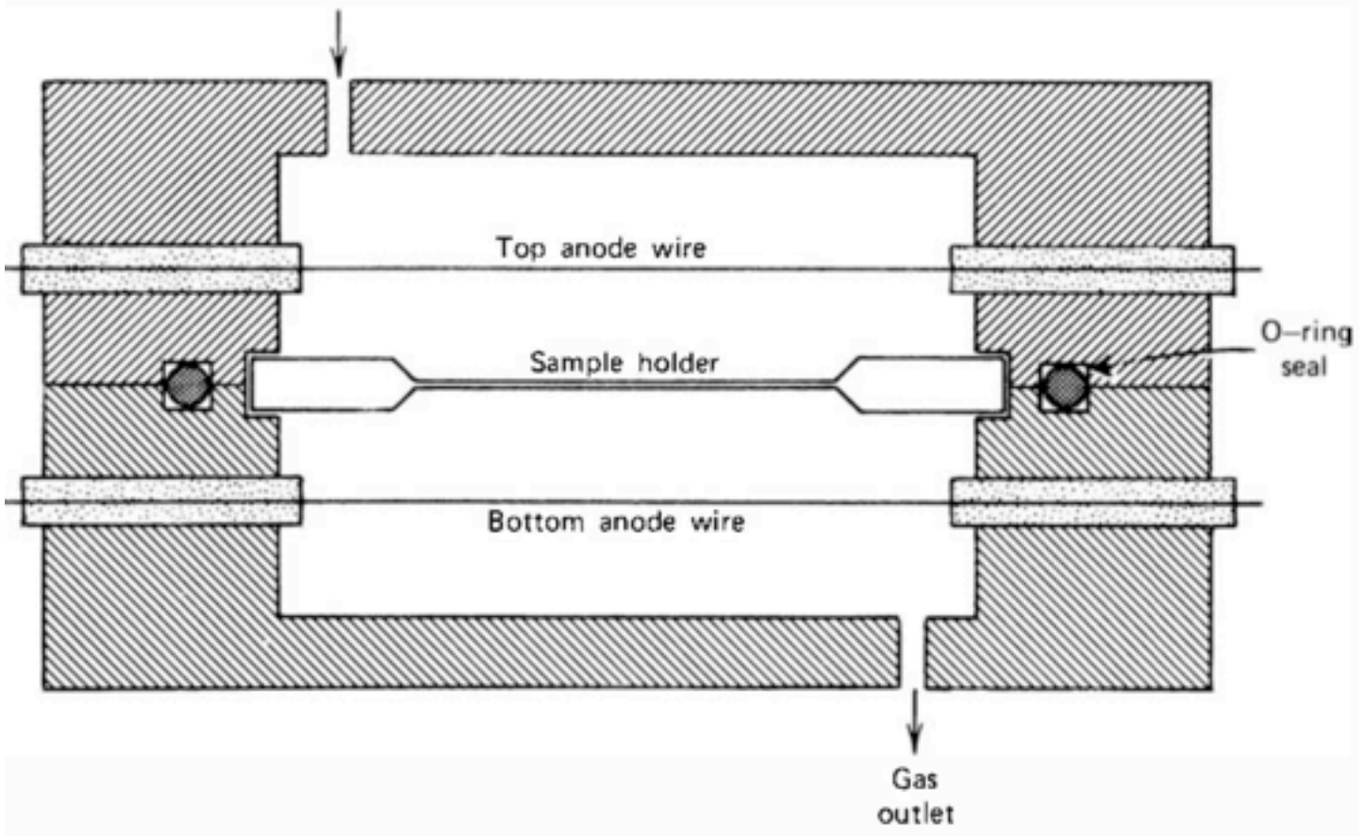

Figure 6.10 A 4π gas flow proportional counter used to detect radiations that emerge from both surfaces of the sample. The top and bottom halves are provided with separate anode wires and can be separated to introduce the sample that is mounted between them.

Proportional Counters

Performance : Gas multiplication factor

$$\ln M = \frac{V}{\ln(b/a)} \cdot \frac{\ln 2}{\Delta V}\left(\ln \frac{V}{pa\ln(b/a)} - \ln K\right)$$

M = gas multiplication factor
V = applied voltage
a = anode radius
b = cathode radius
p = gas pressure

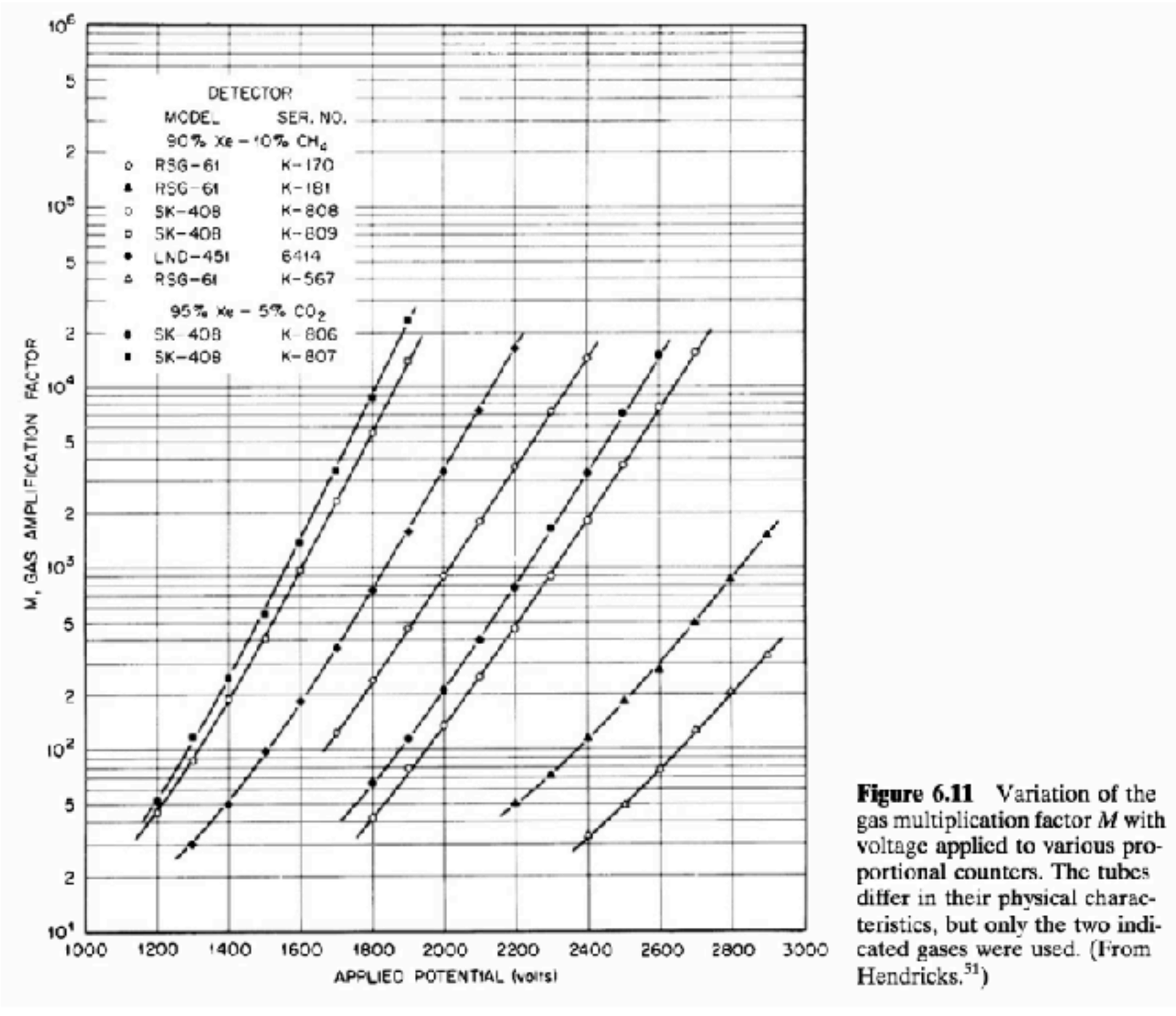

Figure 6.11 Variation of the gas multiplication factor M with voltage applied to various proportional counters. The tubes differ in their physical characteristics, but only the two indicated gases were used. (From Hendricks.[51])

Proportional Counters

Performance : Gas multiplication factor

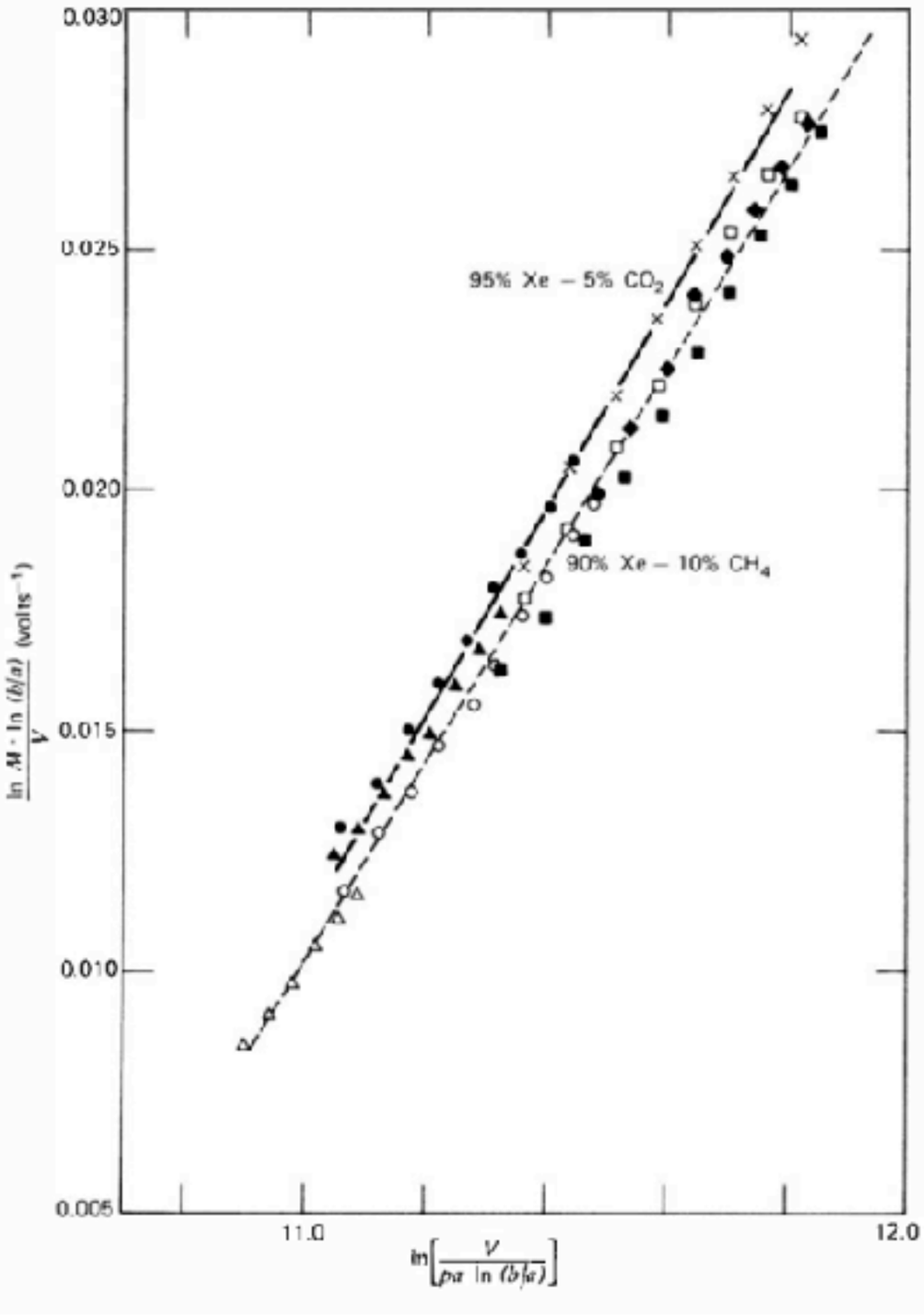

Figure 6.12 A Diethorn plot of the same data shown in Fig. 6.11. As predicted by Eq. (6.10), a graph of $[\ln M \cdot \ln(b/a)/V]$ versus $\ln [V/pa \ln(b/a)]$ for all counters using the same gas closely matches a straight line with slope of $(\ln 2/\Delta V)$ and intercept $(-\ln 2)(\ln K)/\Delta V$. (From Hendricks.[51])

Table 6.1 Diethorn Parameters for Proportional Gases[a]

Gas Mixture	K ($10^4 V$/cm · atm)	ΔV (V)	Reference
90% Ar, 10% CH_4 (P-10)	4.8	23.6	52
95% Ar, 5% CH_4 (P-5)	4.5	21.8	52
100% CH_4 (methane)	6.9	36.5	52
100% C_3H_8 (propane)	10.0	29.5	52
96% He, 4% isobutane	1.48	27.6	52
75% Ar, 15% Xe, 10% CO_2	5.1	20.2	52
69.4% Ar, 19.9% Xe, 10.7% CH_4	5.45	20.3	52
64.6% Ar, 24.7% Xe, 10.7% CO_2	6.0	18.3	52
90% Xe, 10% CH_4	3.62	33.9	51
95% Xe, 5% CO_2	3.66	31.4	51

[a]See Eq. (6.10).

Proportional Counters

Energy resolution

Table 6.2 Resolution-Related Constants for Proportional Gases

Gas	W (eV/ion pair)	Fano Factor F		Multiplication Variance b	Energy Resolution at 5.9 keV	
		Calculated[a]	Measured		Calculated[b]	Measured
Ne	36.2	0.17		0.45	14.5%	
Ar	26.2	0.17		0.50	12.8%	
Xe	21.5		≤ 0.17			
Ne + 0.5% Ar	25.3	0.05		0.38	10.1%	11.6%
Ar + 0.5% C_2H_2	20.3	0.075	≤ 0.09	0.43	9.8%	12.2%
Ar + 0.8% CH_4	26.0	0.17	≤ 0.19			
Ar + 10% CH_4	26[c]			0.50	12.8%	13.2%

[a]From Alkhazov et al.[22]
[b]Given by $2.35[W(F + b)/5900\ \text{eV}]^{1/2}$ [see Eq. (6.24)].
[c]From Wolff.[52]
Source: Adapted from Sipila.[59]

Proportional Counters

Time characteristics

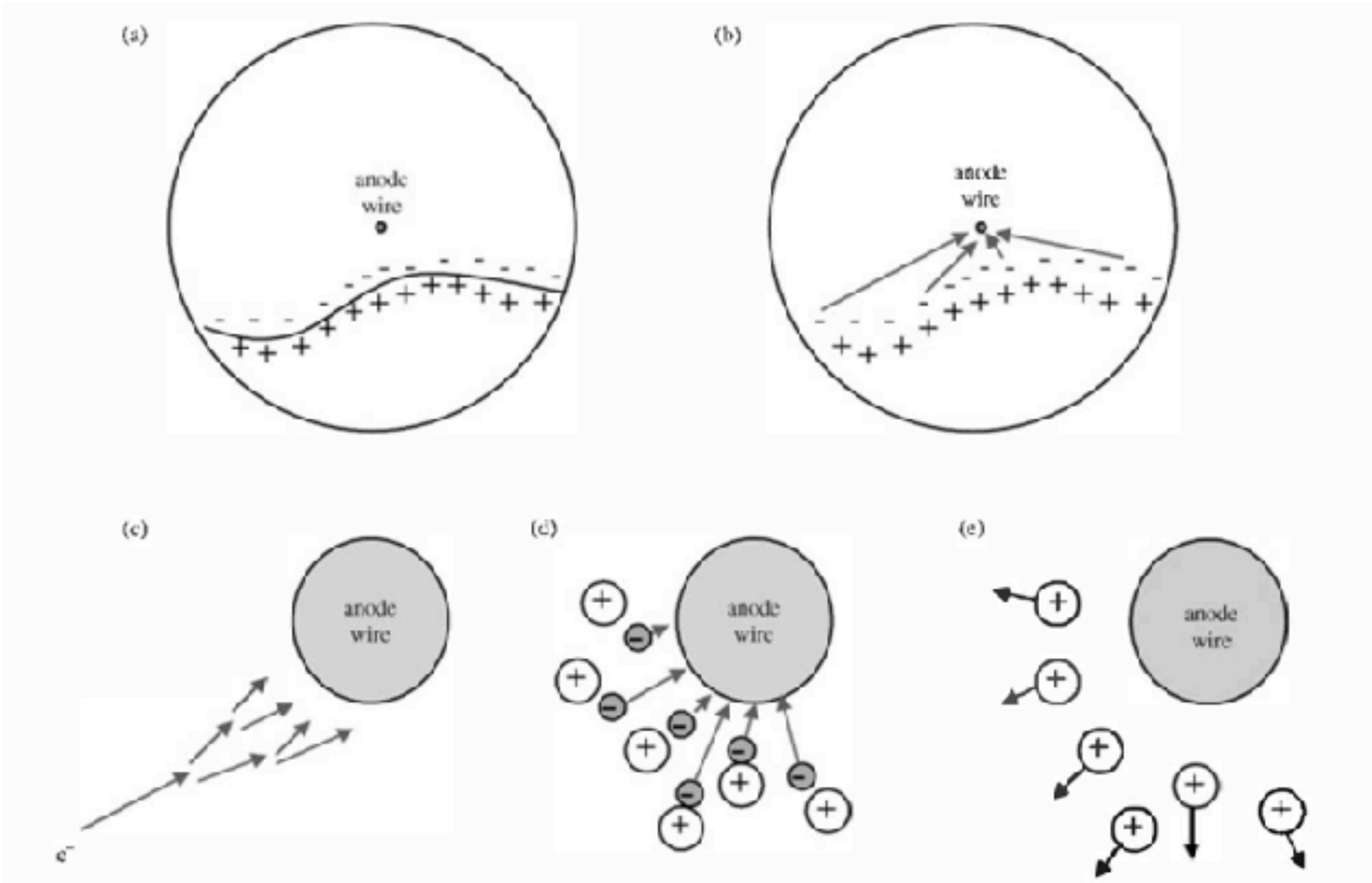

Figure 6.14 The sequence of events in producing a pulse in a proportional counter. (*a*) An energetic electron or charged particle produces ion pairs in its passage through the counter gas (nanosecond time scale). (*b*) The ionization electrons drift inward along a radius toward the anode wire (few microsecond time scale). (*c*) Each electron arriving at the multiplication region triggers its own avalanche (submicrosecond time scale). (*d*) The hundreds or thousands of electrons formed in each avalanche are quickly drawn to the wire surface (submicrosecond time scale). (*e*) The much slower positive ions from the avalanche move outward through the high field region near the wire, producing most of the output pulse amplitude (few microsecond time scale).

Proportional Counters

Time characteristics

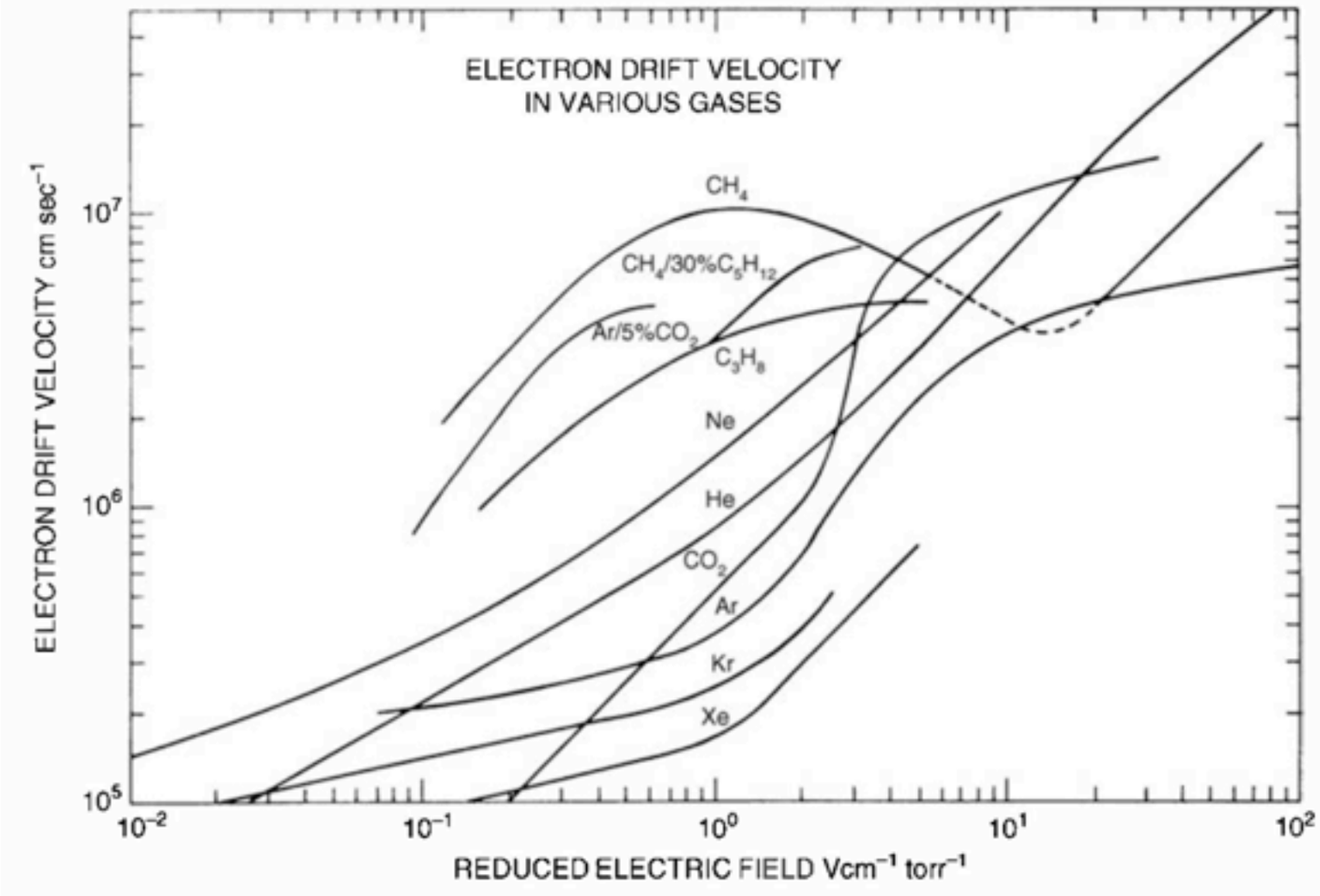

Figure 6.17 The electron drift velocities in various gases, as compiled by Jeavons et al.[75]

Proportional Counters

Multi-wire Proportional Counters

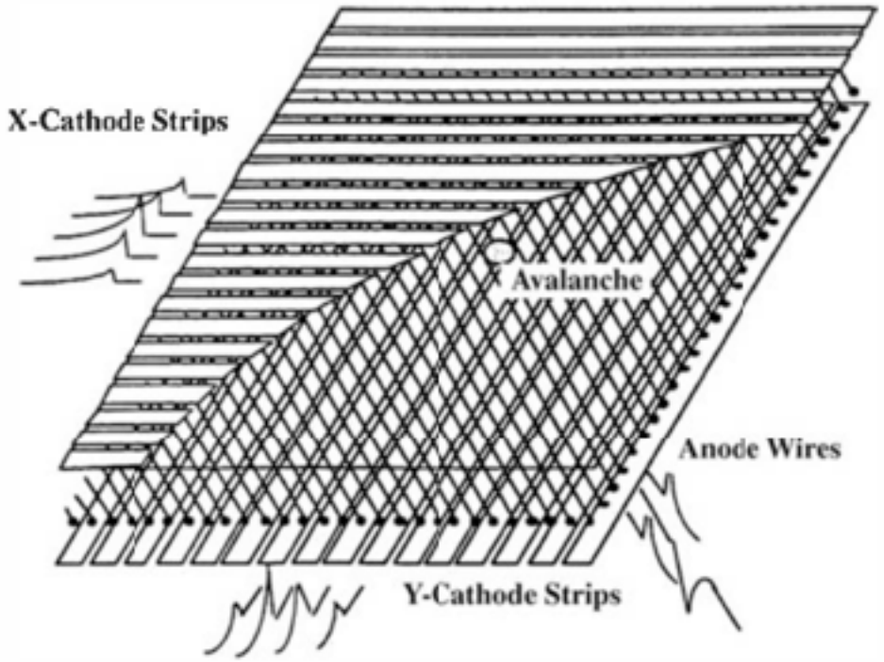

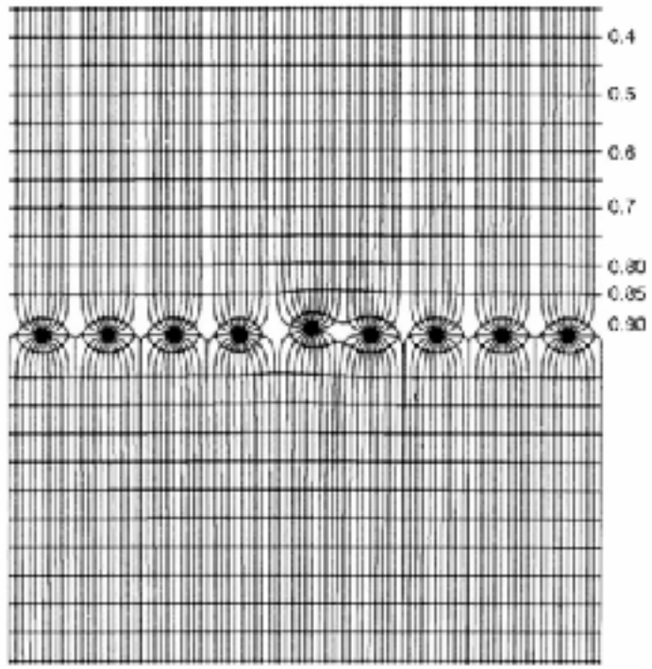

Figure 6.21 A plot of the electric field lines created by a grid of anode wires (running perpendicular to the page) that are placed equidistant between two parallel cathode plates at the top and bottom of the figure. Over much of the volume away from the grid, the field is nearly uniform. A high-field region is created in the immediate vicinity of each grid wire. (From Charpak and Sauli.[107])

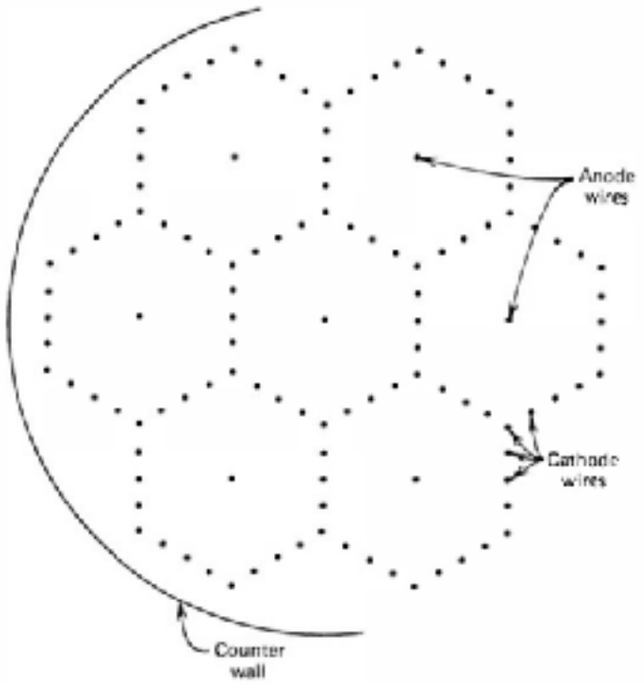

Figure 6.23 The cross-sectional view of a multicell proportional counter. A single anode wire is at the center of each cell, surrounded by a grid of cathode wires.

Proportional Counters

Gas Proportional Scintillation Counters

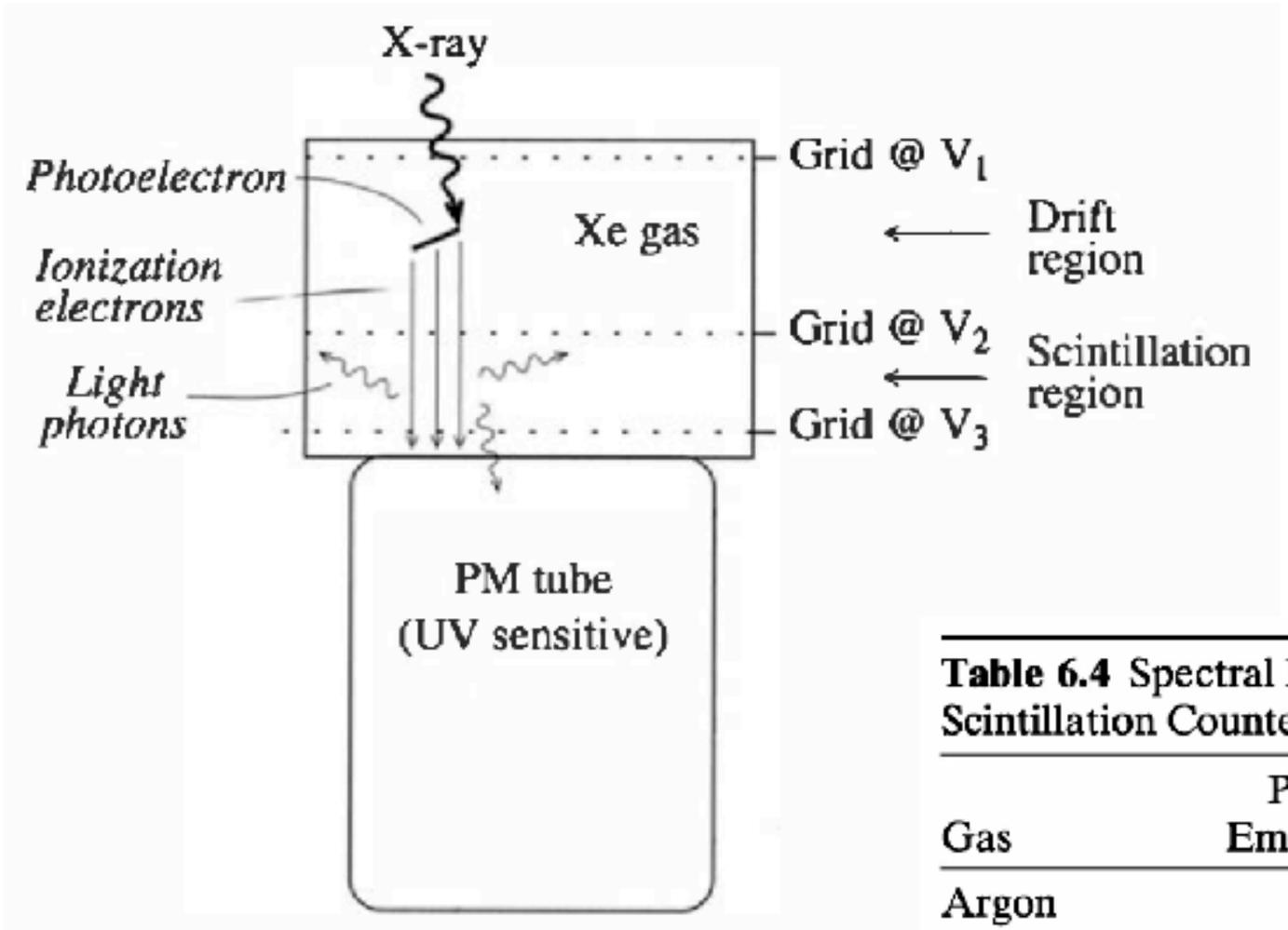

Table 6.4 Spectral Properties of Light Emitted in Gas Proportional Scintillation Counters

Gas	Peak Wavelength of Emission Spectrum (nm)	FWHM of Emission Spectrum (nm)
Argon	128	10
Krypton	147	12
Xenon	173	14

Data from Suzuki and Kubota.[138]

Proportional Counters

Microstrip Gas Chamber

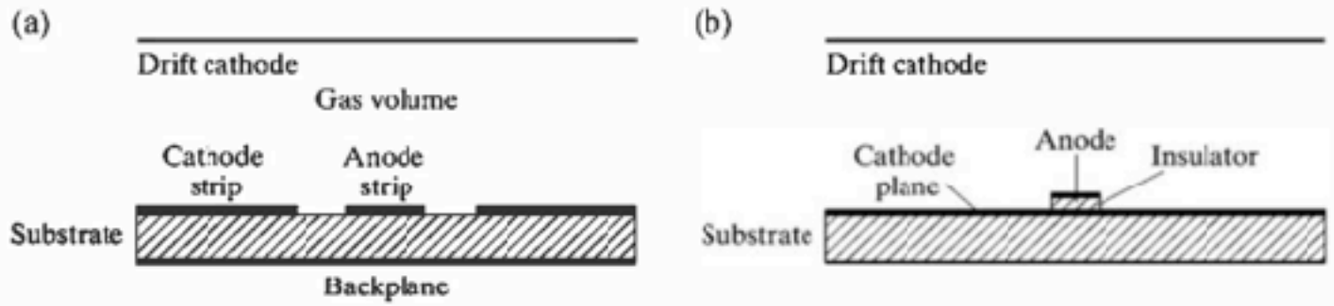

Figure 6.26 Cross sections of the electrode patterns for two configurations of microstrip gas chambers. Part (*a*) is a common pattern of alternating anode and cathode strips, and part (*b*) is a pattern of narrow anodes separated from a continuous cathode by insulating supports (commonly called a *microgap* configuration.)

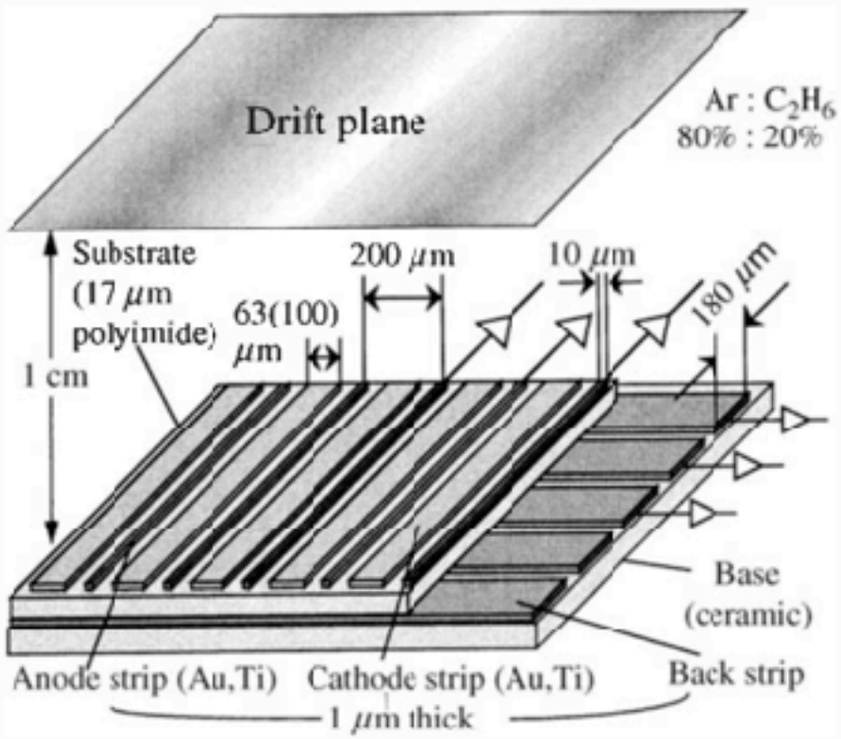

Figure 6.27 Structure of a two-dimensional position-sensing microstrip gas chamber. (From Tanimori et al.[113])

Proportional Counters

Gas Electron Multiplier (GEM)

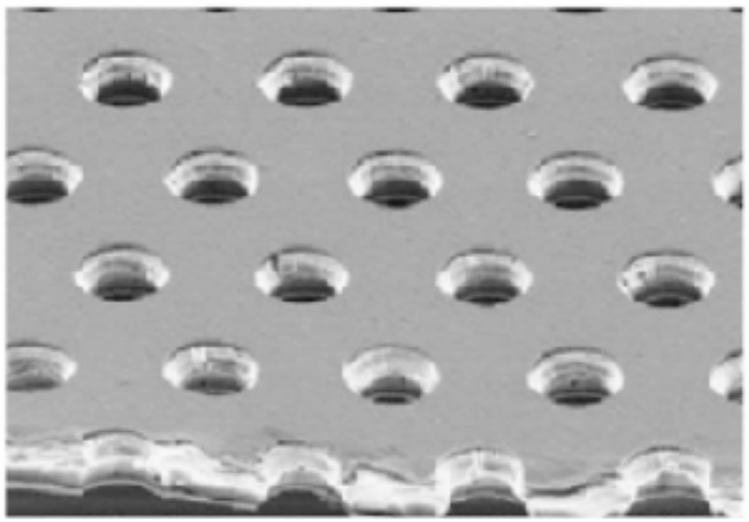

Figure 6.28 An electron microscope image of a small portion of a GEM foil. The hole pitch is 140 μm and the diameter is 70 μm. (From F. Sauli.[147])

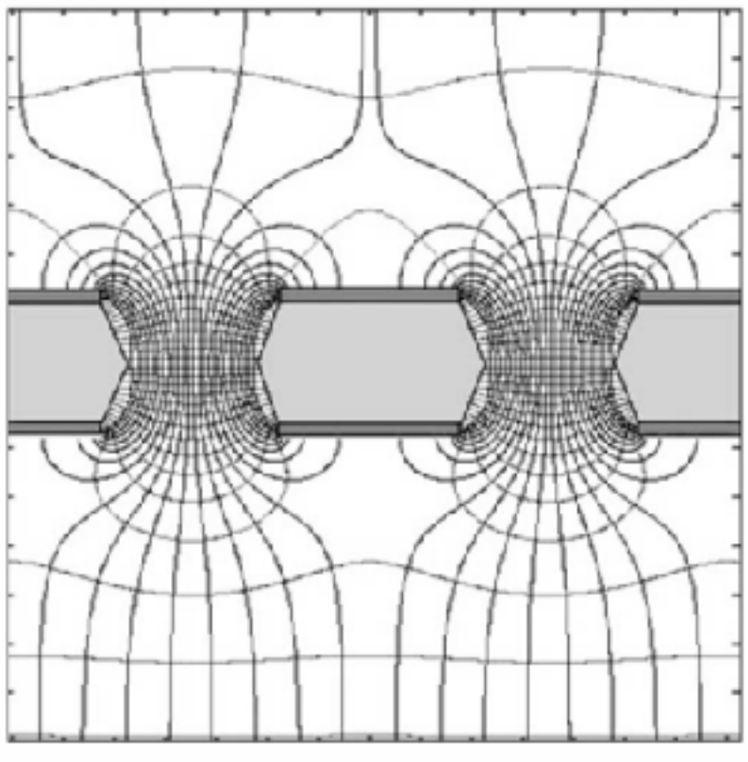

Figure 6.29 Sketch showing electric field lines and equipotential contours in the vicinity of two holes in a GEM foil. The concentration of the field lines leads to high field strength in the holes. (From F. Sauli.[149])

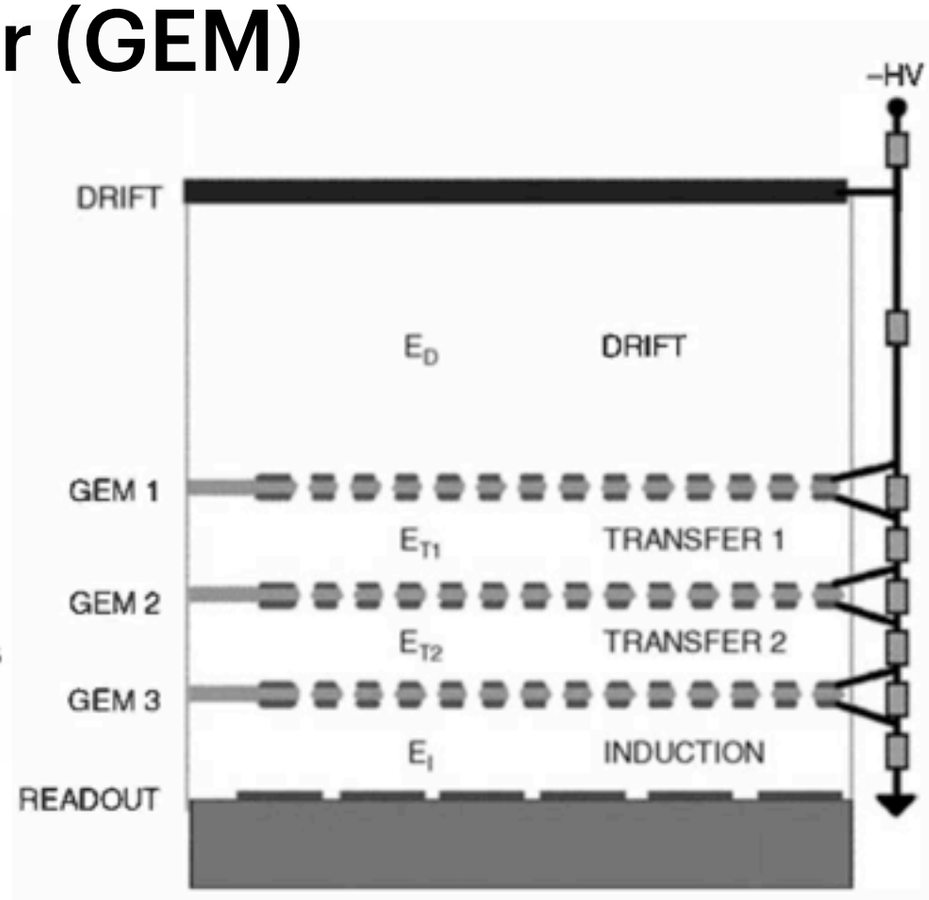

Figure 6.30 Arrangement of three GEM foils in cascade. The original ionization occurs in the region labeled DRIFT, and the ionization electrons are drawn downward to the first GEM foil. The amplified electrons emerging from GEM 1 are drifted to GEM 2 where they again multiply. One more GEM stage provides further amplification, and its output is collected at the readout plane that can be a gas microstrip structure or other readout pattern. The resistor chain at the right provides appropriate voltage differences between elements from a single high-voltage supply. (From F. Sauli.[150])

Proportional Counters

Micromegas (Micro-mesh gaseous structure)

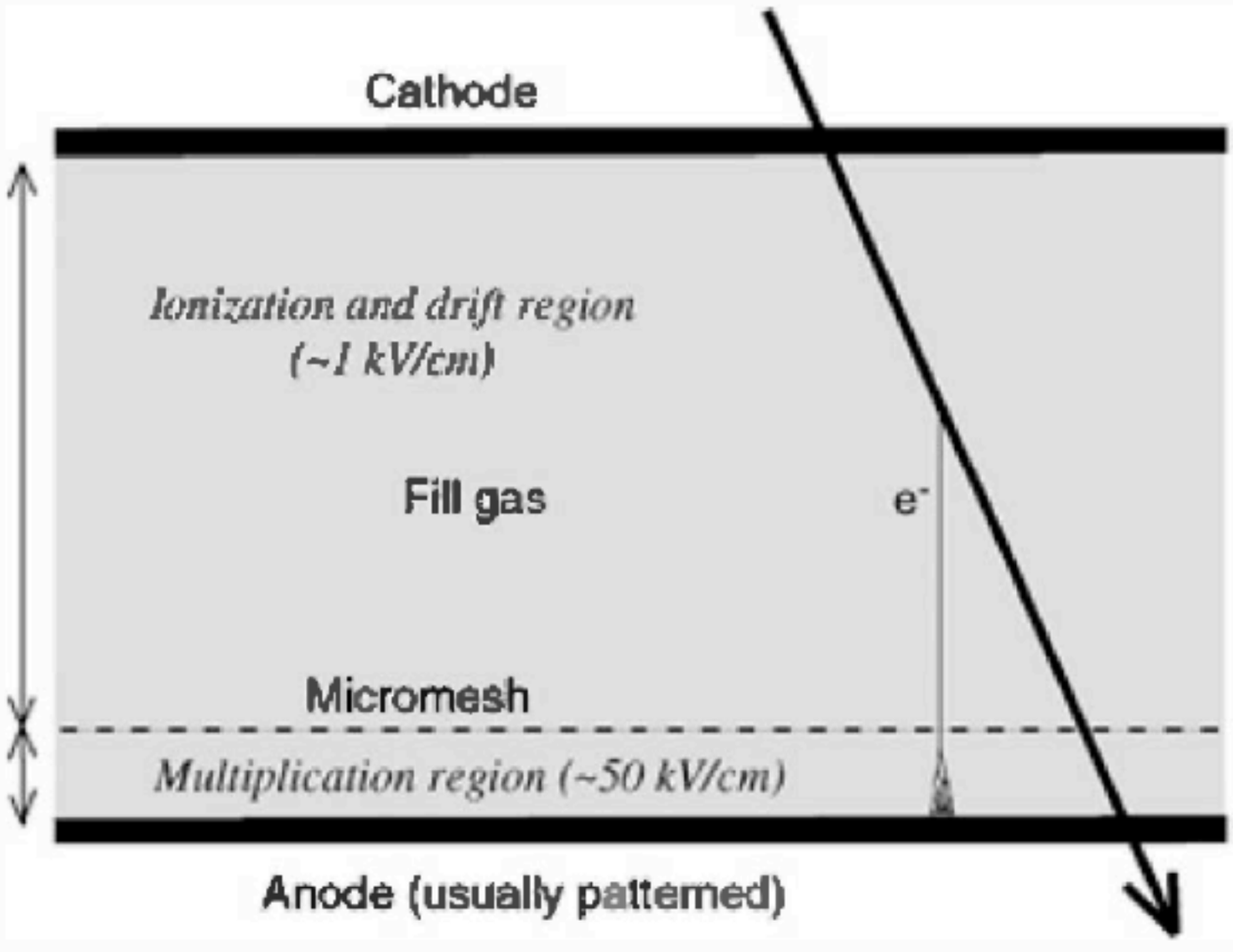

Figure 6.31 Basic principle of a Micromegas detector. Ionization electrons formed in the upper portion of the gas-filled chamber drift downward in a moderate electric field and pass through the micromesh into the multiplication region. There the electric field strength is much higher, and avalanches form.

Proportional Counters

Resistive Plate Chambers

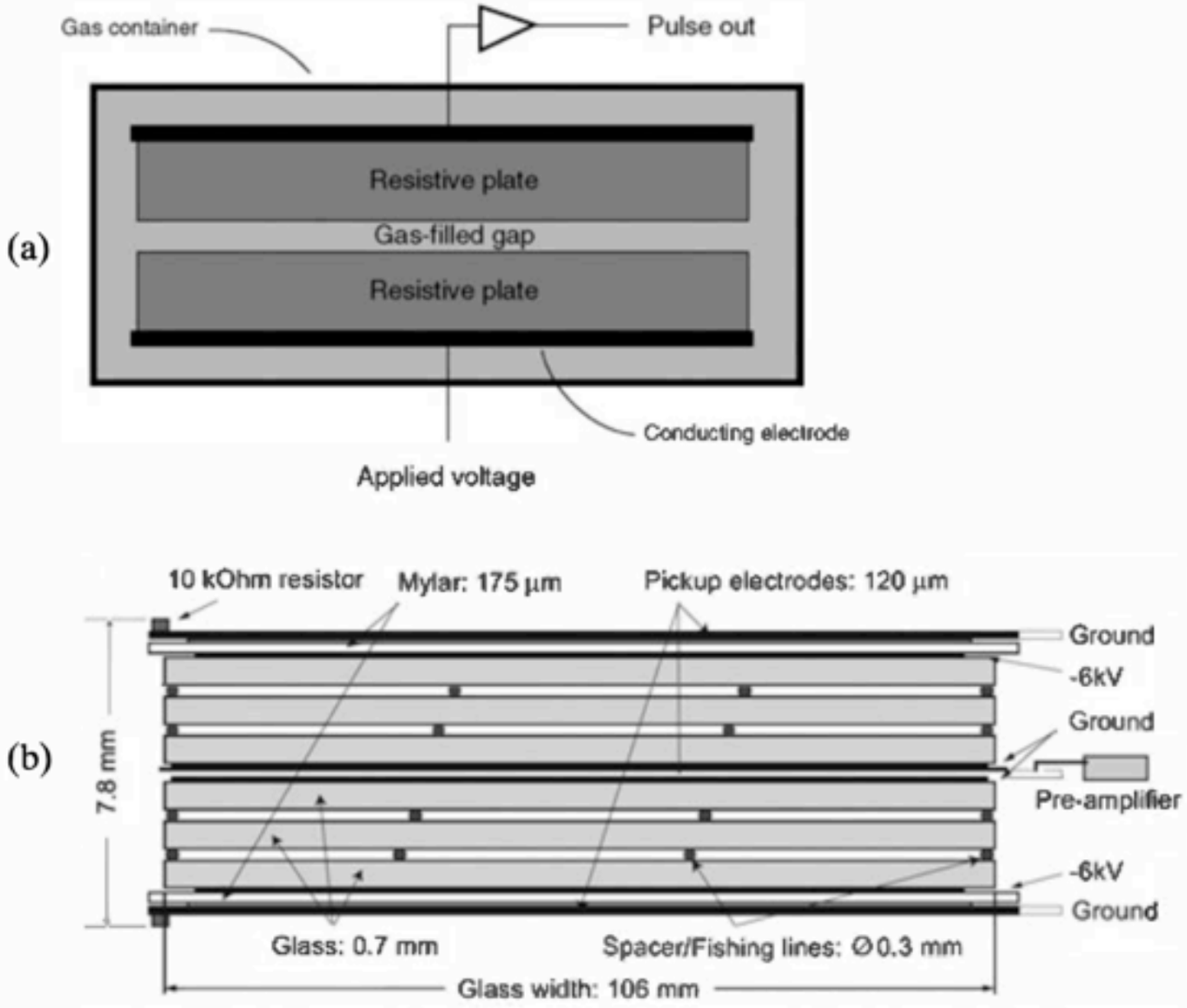

Figure 6.32 (*a*) Simplified representation of a Resistive Plate Chamber (RPC). A gas-filled gap separates two plates that have an appropriate electrical resistivity. (*b*) A multigap RPC. The full high voltage is applied to the outer plates, and the inner plates adjust to intermediate voltages. (From G. Belli et al.[164])

Geiger-Mueller Counters

Geiger-Mueller Counters

Avalanches

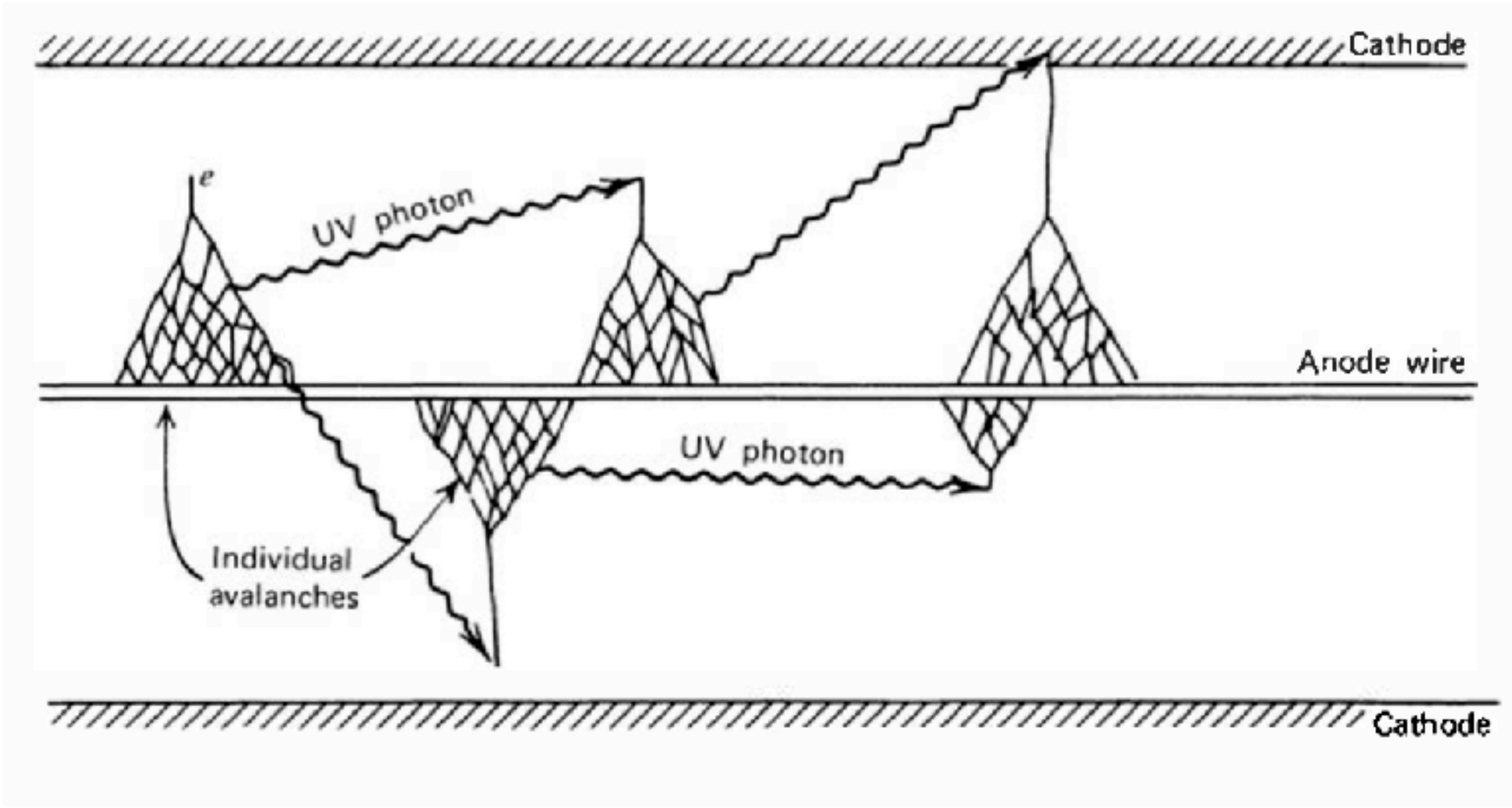

Geiger-Mueller Counters

Avalanches

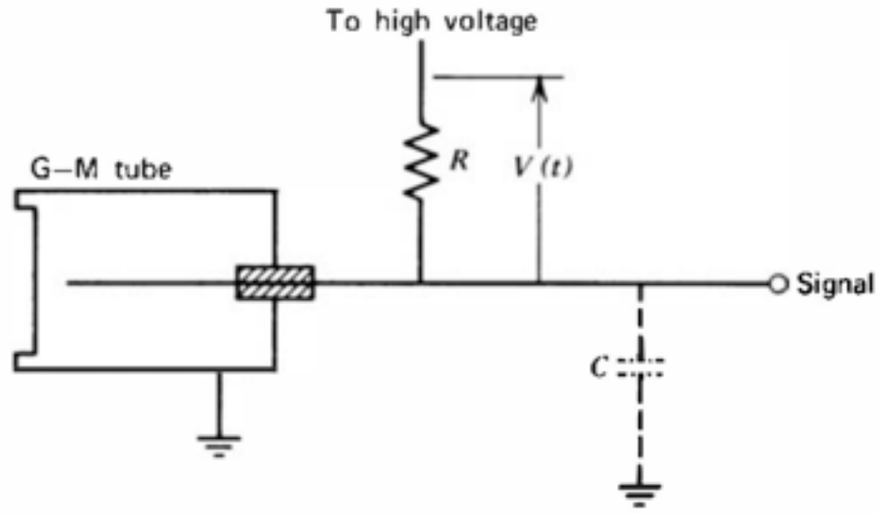

Figure 7.2 Equivalent counting circuit for a G-M tube. The product of resistance R and capacitance C (usually only inherent capacitance of the tube and electronics) determines the time constant of the restoration of the high voltage following a Geiger discharge.

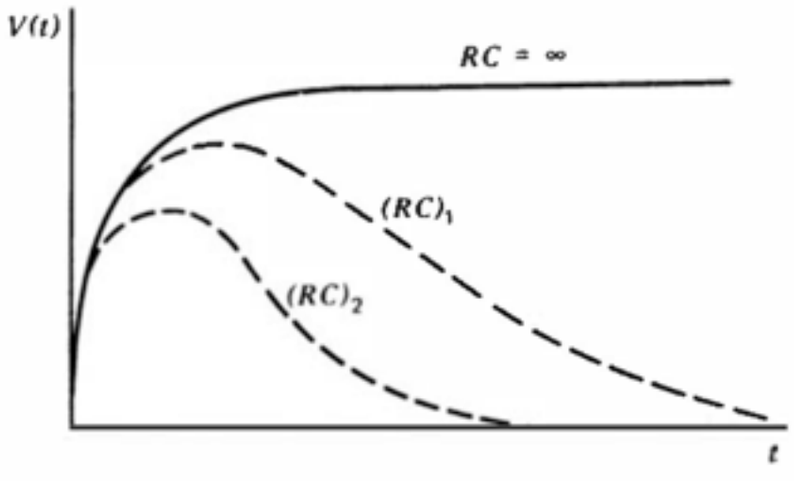

Figure 7.3 Shape of the G-M tube output pulse for different assumed time constants RC of the counting circuit. Here $(RC)_2 < (RC)_1 <$ infinite time constant. The signal voltage $V(t)$ is assumed to be measured as indicated in Fig. 7.2, giving a positive polarity. More conventionally, the pulse is measured with respect to ground within the amplifier, leading to inverted shape or negative polarity.

Geiger-Mueller Counters

Dead time

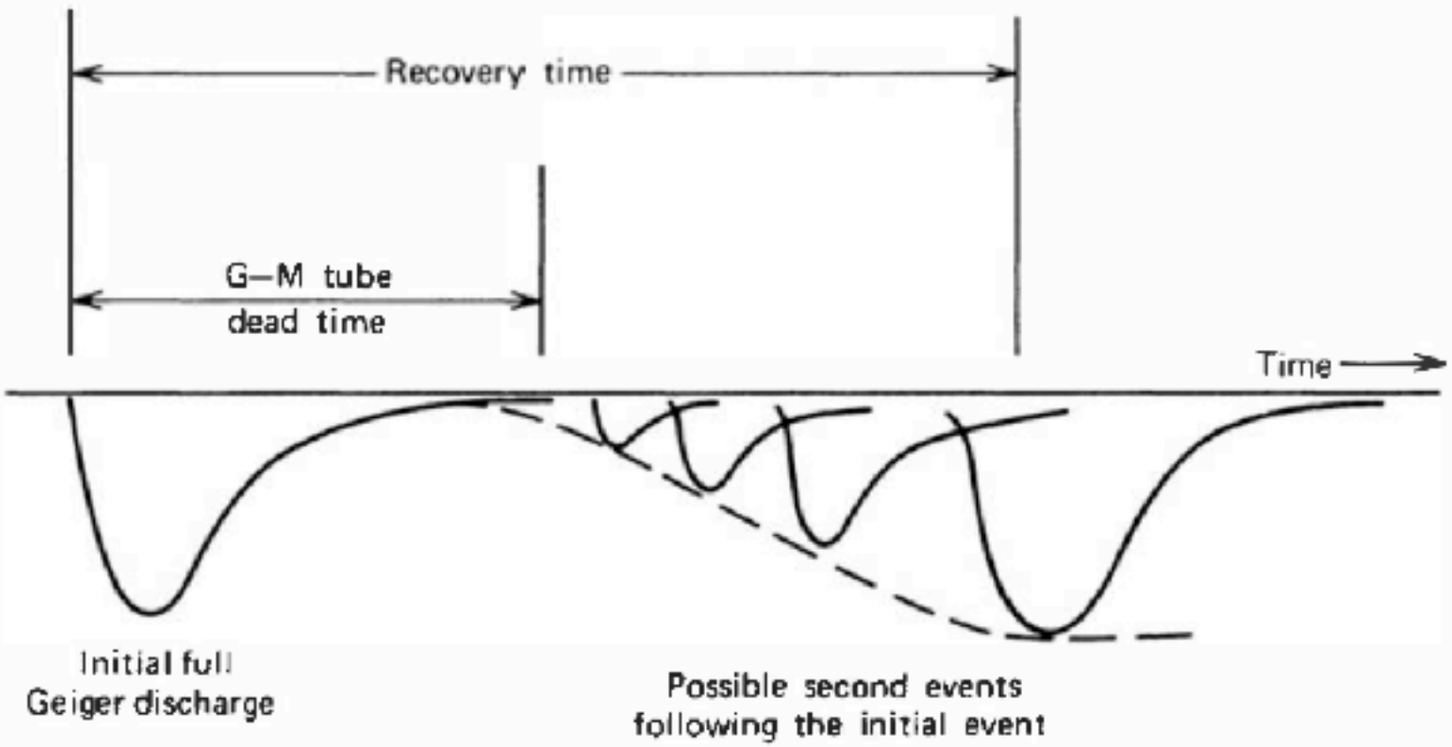

Figure 7.4 Illustration of the dead time of a G-M tube. Pulses of negative polarity conventionally observed from the detector are shown.

Geiger-Mueller Counters

Counting Plateau

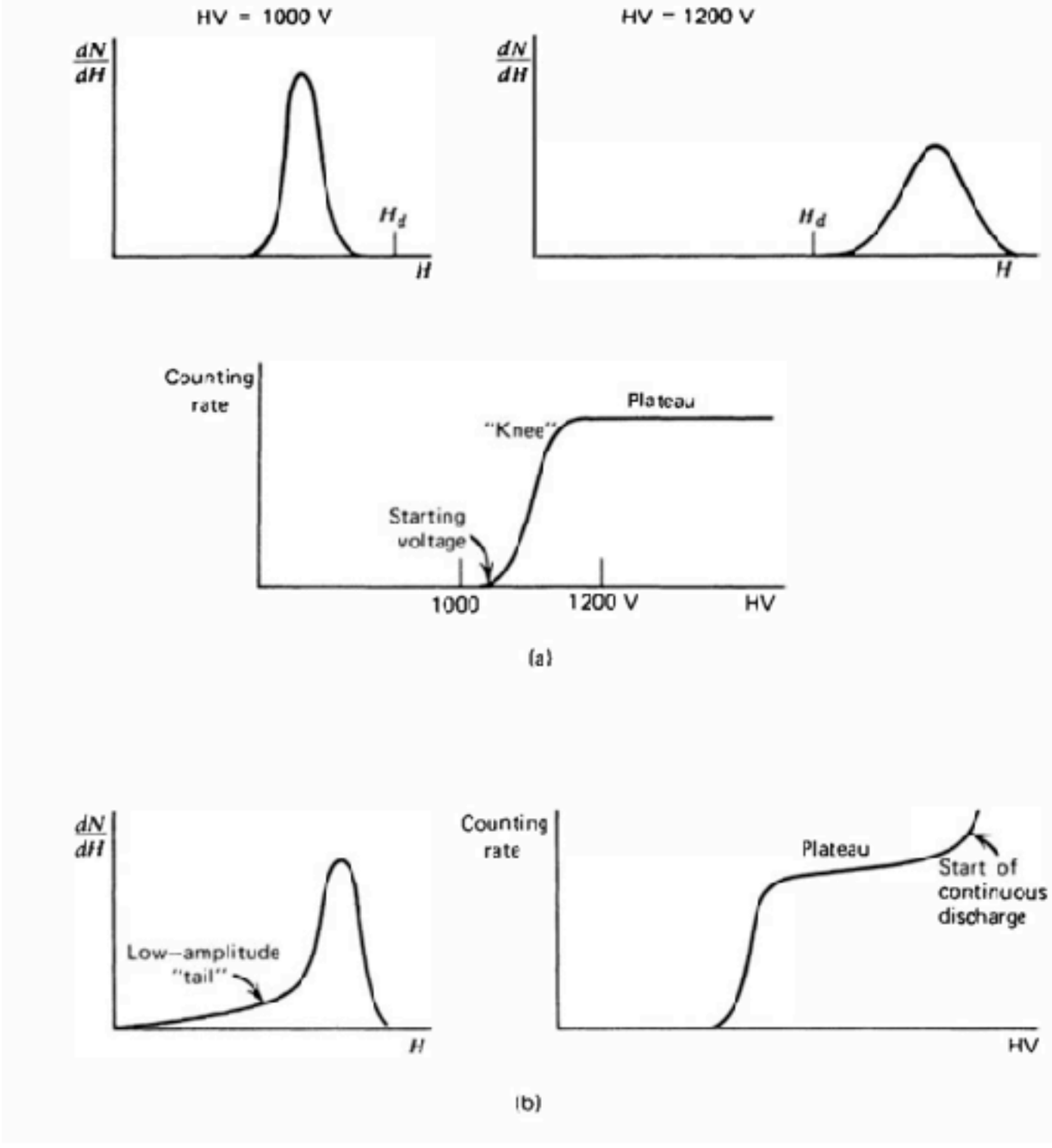

Figure 7.5 (*a*) The establishment of the counting plateau for a G-M tube. As the high voltage is varied in this example from 1000 to 1200 V, the output pulses change from falling below the counter threshold H_d to a situation in which all pulses are larger than H_d. (*b*) The low-amplitude tail on the pulse height spectrum at the left causes a finite slope of the plateau in the counting curve.

Geiger-Mueller Counters

Design

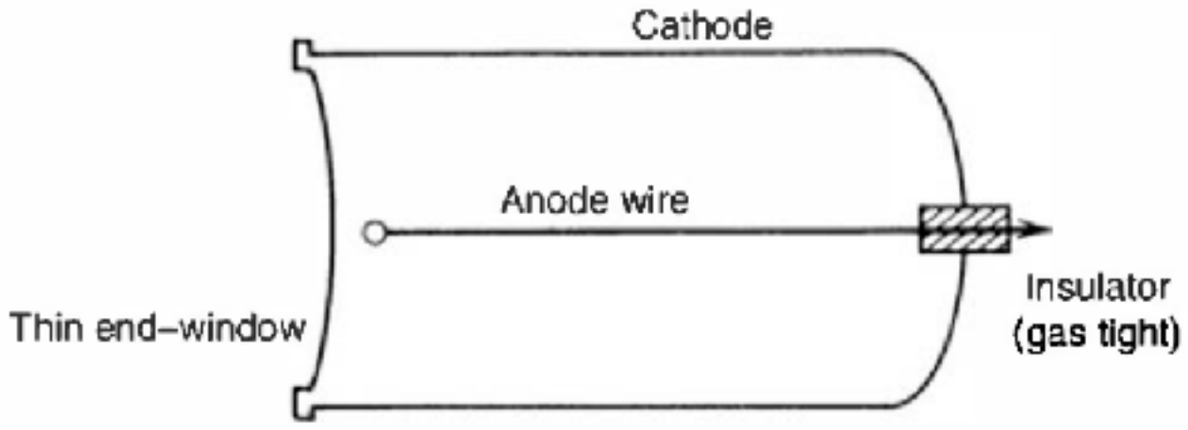

Figure 7.6 A cross section of a typical end-window Geiger tube.

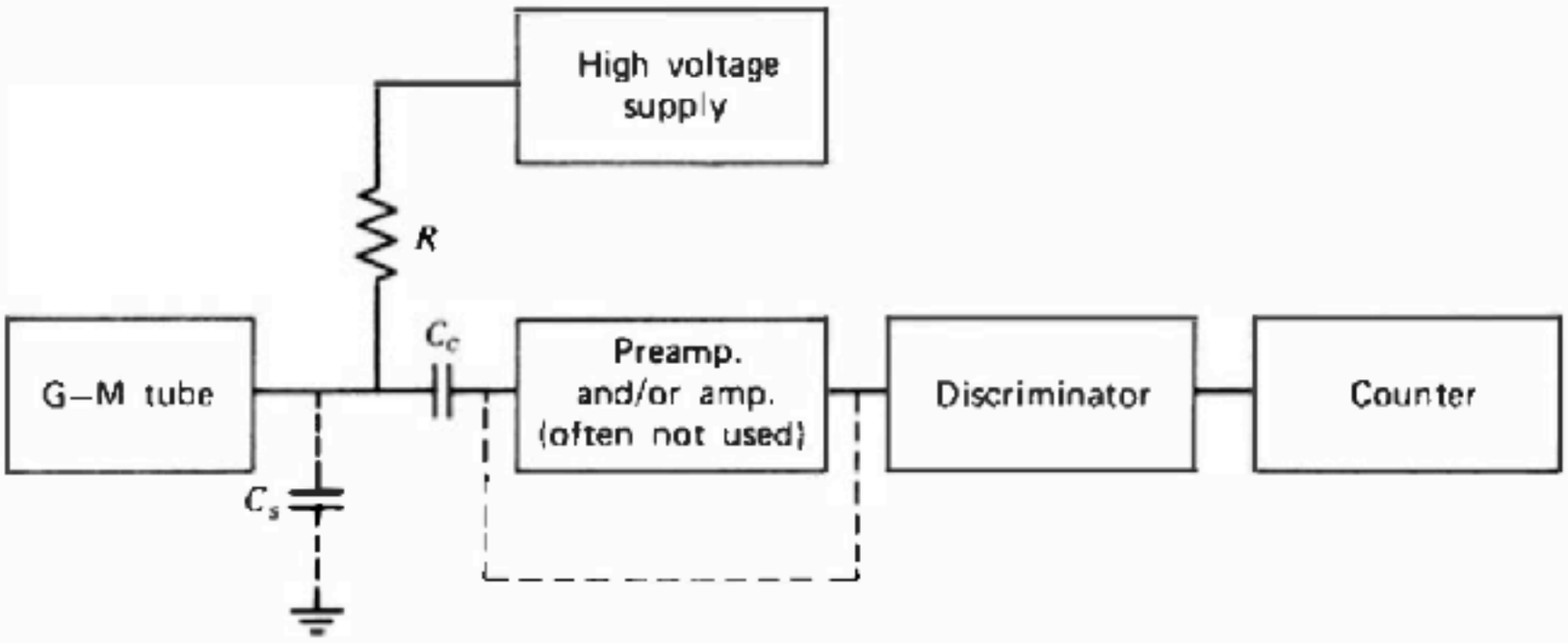

Figure 7.7 Block diagram of the counting electronics normally associated with a G-M tube.

Geiger-Mueller Counters

Time-to-first-count method

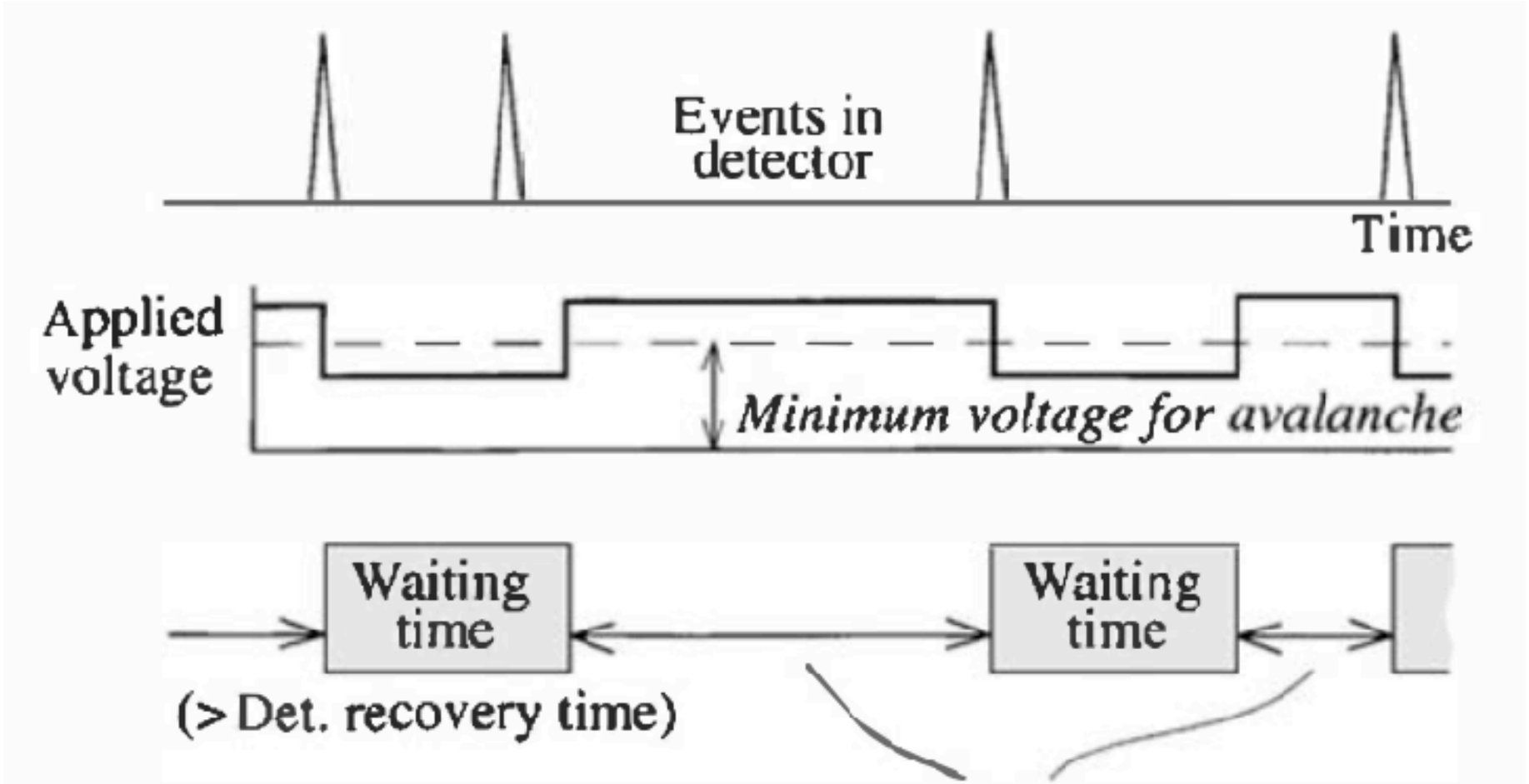

$\bar{t}$ = average time interval between detector turn-on and next event

event rate: $r = \frac{1}{\bar{t}}$

Scintillation Detector

Scintillation Detector

Properties

The ideal scintillation material should possess the following properties:

1. It should convert the kinetic energy of charged particles into detectable light with a high scintillation efficiency.
2. This conversion should be linear—the light yield should be proportional to deposited energy over as wide a range as possible.
3. The medium should be transparent to the wavelength of its own emission for good light collection.
4. The decay time of the induced luminescence should be short so that fast signal pulses can be generated.
5. The material should be of good optical quality and subject to manufacture in sizes large enough to be of interest as a practical detector.
6. Its index of refraction should be near that of glass ($\sim$1.5) to permit efficient coupling of the scintillation light to a photomultiplier tube or other light sensor.

Scintillation Detector

Scintillation mechanism in organics

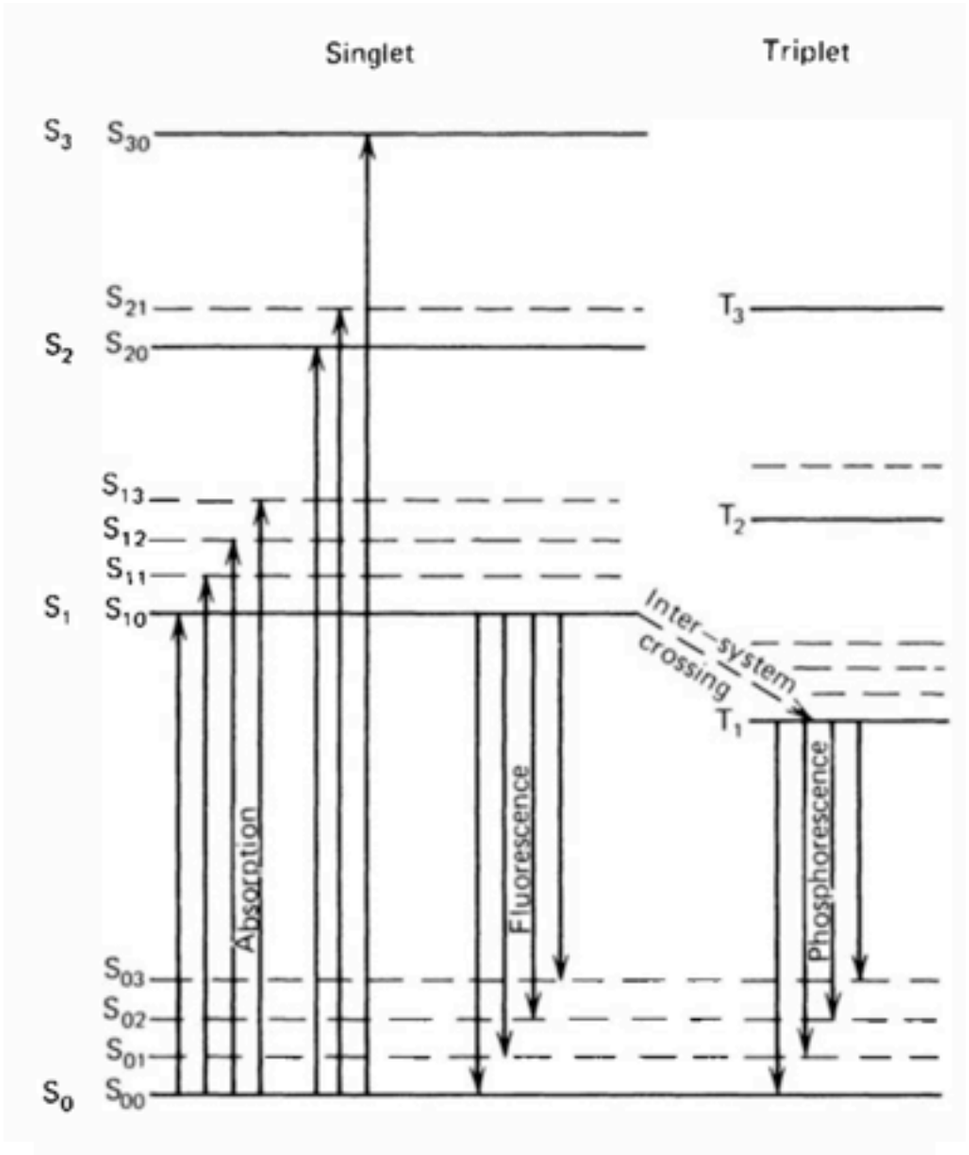

Figure 8.1 Energy levels of an organic molecule with π-electron structure. (From J. B. Birks, *The Theory and Practice of Scintillation Counting*. Copyright 1964 by Pergamon Press, Ltd. Used with permission.)

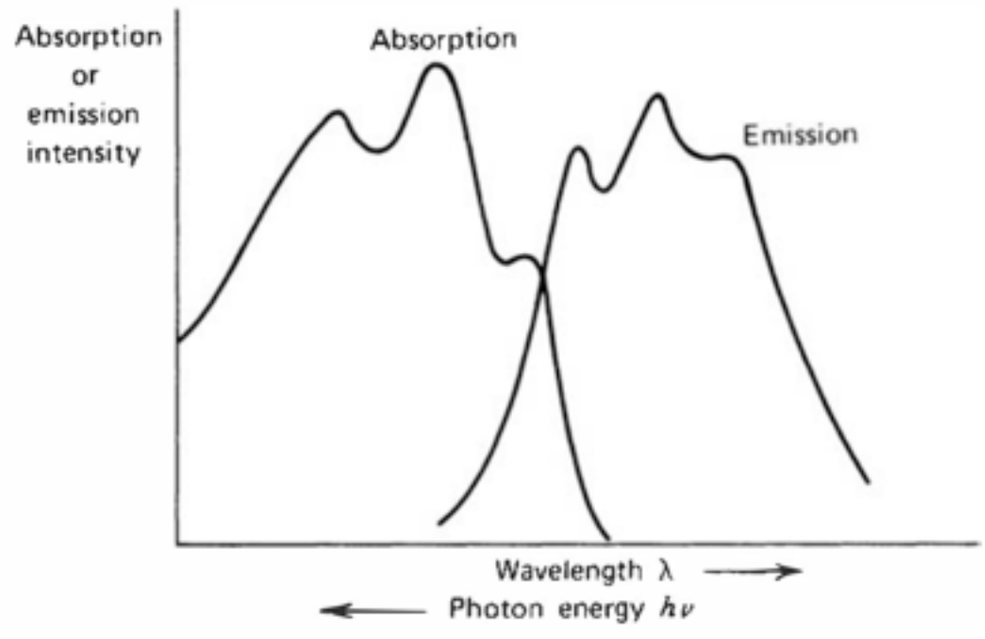

Figure 8.2 The optical absorption and emission spectra for a typical organic scintillator with the level structure shown in Fig. 8.1.

Scintillation Detector

Types of organic scintillators

1. Pure organic crystals
2. Liquid organic solutions
3. Plastic scintillators
4. Thin film scintillators
5. Loaded organic scintillators

Scintillation Detector

Light output

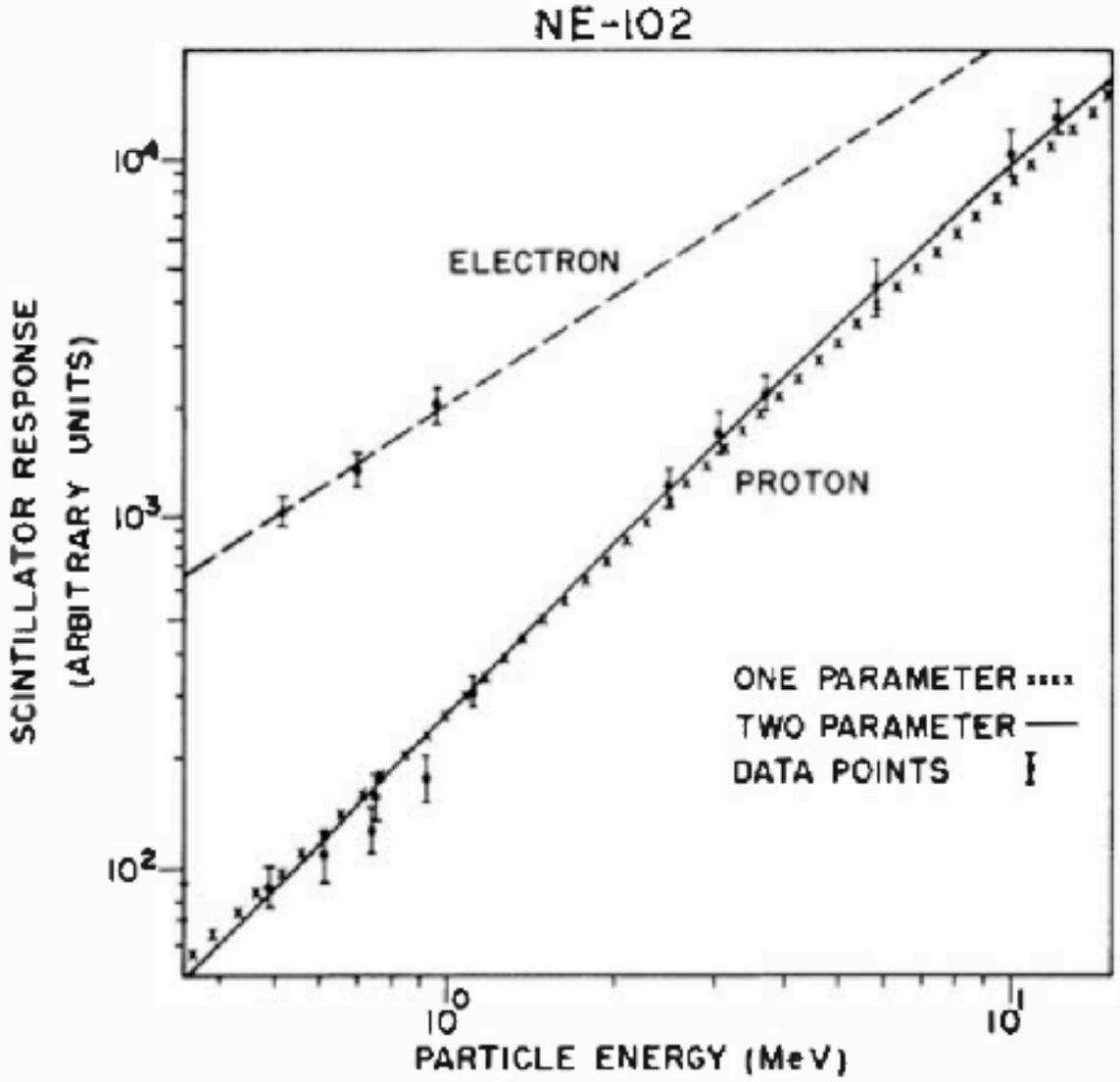

Figure 8.3 The scintillation light yield for a common plastic scintillator (NE 102) when excited by electrons and protons. The data are fit by curves from Eq. (8.3) (one parameter) and Eq. (8.9) (two parameter). (From Craun and Smith.[42])

Scintillation Detector

Time response

$$I = I_0\left(e^{-t/\tau} - e^{-t/\tau_1}\right)$$

Table 8.2 Some Timing Properties of Fast Plastic Scintillators

	Parameters for Eq. (8.10)		Parameters for Eq. (8.11)		
	τ_1 (rise)	τ (decay)	σ_{ET}	τ	Measured FWHM
NE 111	0.2 ns	1.7 ns	0.2 ns	1.7 ns	1.54 ns
Naton 136	0.4 ns	1.6 ns	0.5 ns	1.87 ns	2.3 ns
NE 102A	0.6 ns	2.4 ns	0.7 ns	2.4 ns	3.3 ns

Data from Bengtson and Moszynski.[51]

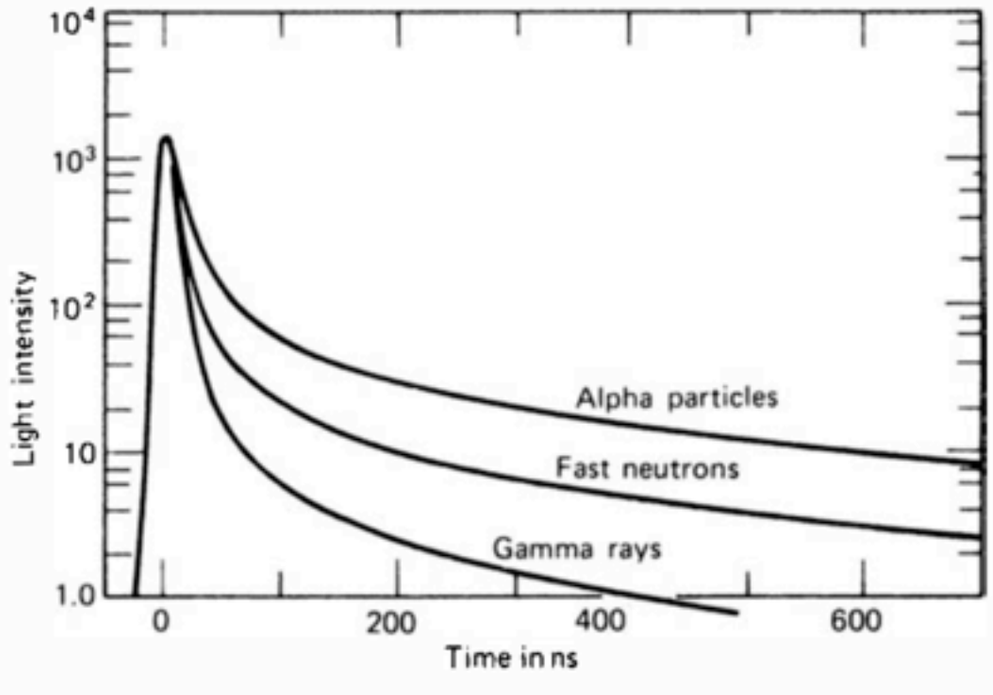

Figure 8.5 The time dependence of scintillation pulses in stilbene (equal intensity at time zero) when excited by radiations of different types. (From Bollinger and Thomas.[67])

Scintillation Detector

Inorganic scintillator

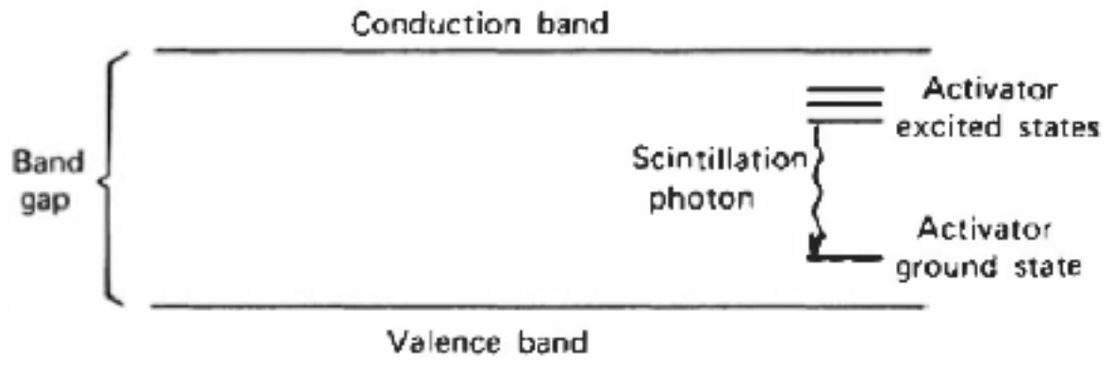

Figure 8.6 Energy band structure of an activated crystalline scintillator.

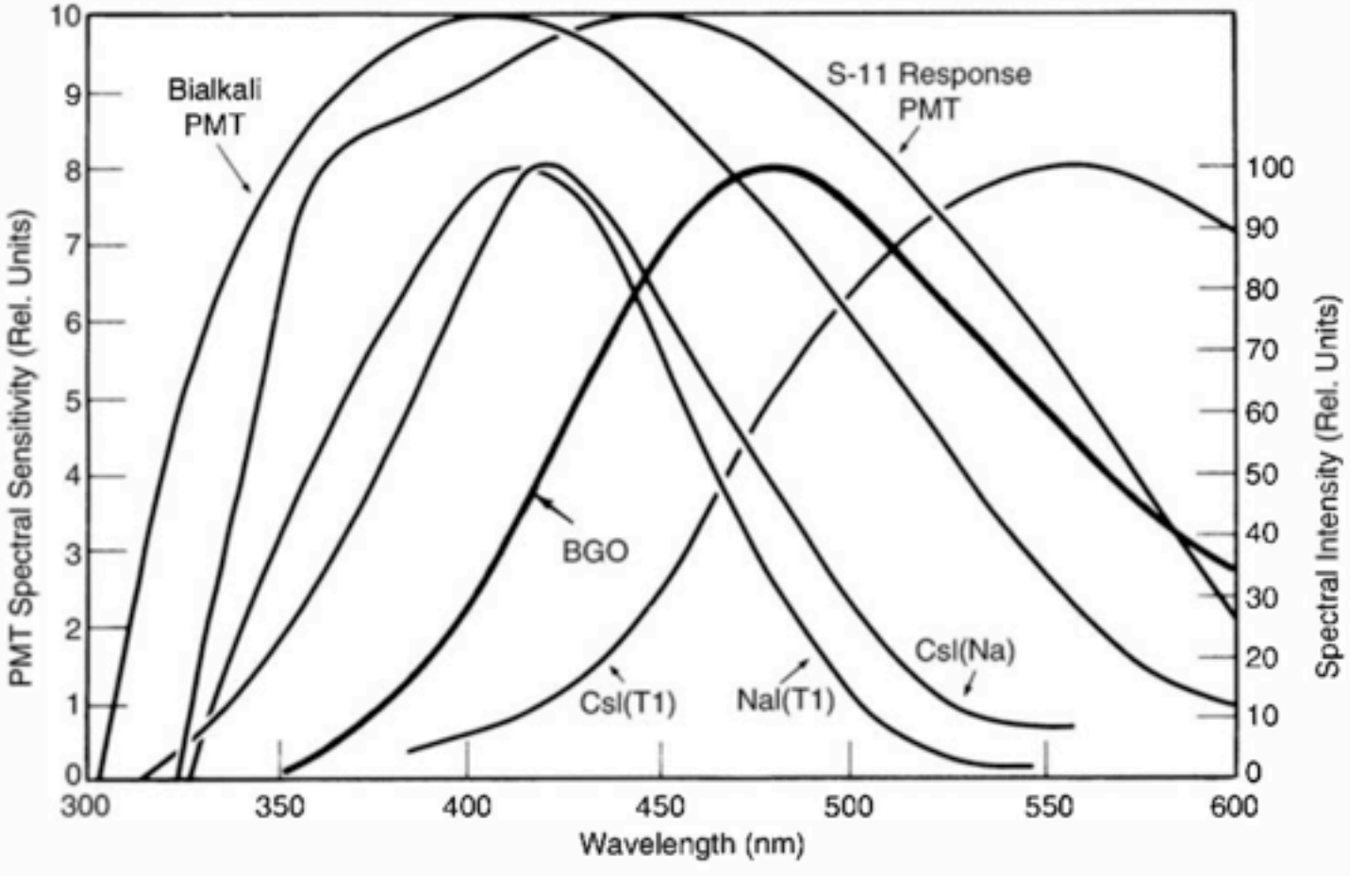

Figure 8.7 The emission spectra of several common inorganic scintillators. Also shown are the response curves for two widely used photocathodes. (Primarily from *Scintillation Phosphor Catalog*, The Harshaw Chemical Company. The emission spectrum for BGO is from Ref. 79.)

Scintillation Detector

Inorganic scintillator

1. NaI(Tl)
2. CsI(Tl) and CsI(Na)
3. LiI(Eu)
4. BGO
5. CdWO4 and CaWO4
6. Zns(Ag)
7. CaF2(Eu)
8. SrI2(Eu)
9. BaF2
10. CsI
11. Cs-Halides
12. PbWO4
13. Rare Earth Oxyorthosilicates
14. Lanthanoid Pyrosilicates
15. Rare Earth Aluminum Perovskites
16. Rare Earth Aluminum Garnets
17. Lanthanum Halides
18. Lutetium Halides
19. Elpasolites
20. Ceramics scintillators
21. Glass scintillators
22. Noble gas scinitllator

Scintillation Detector

NaI(Tl)

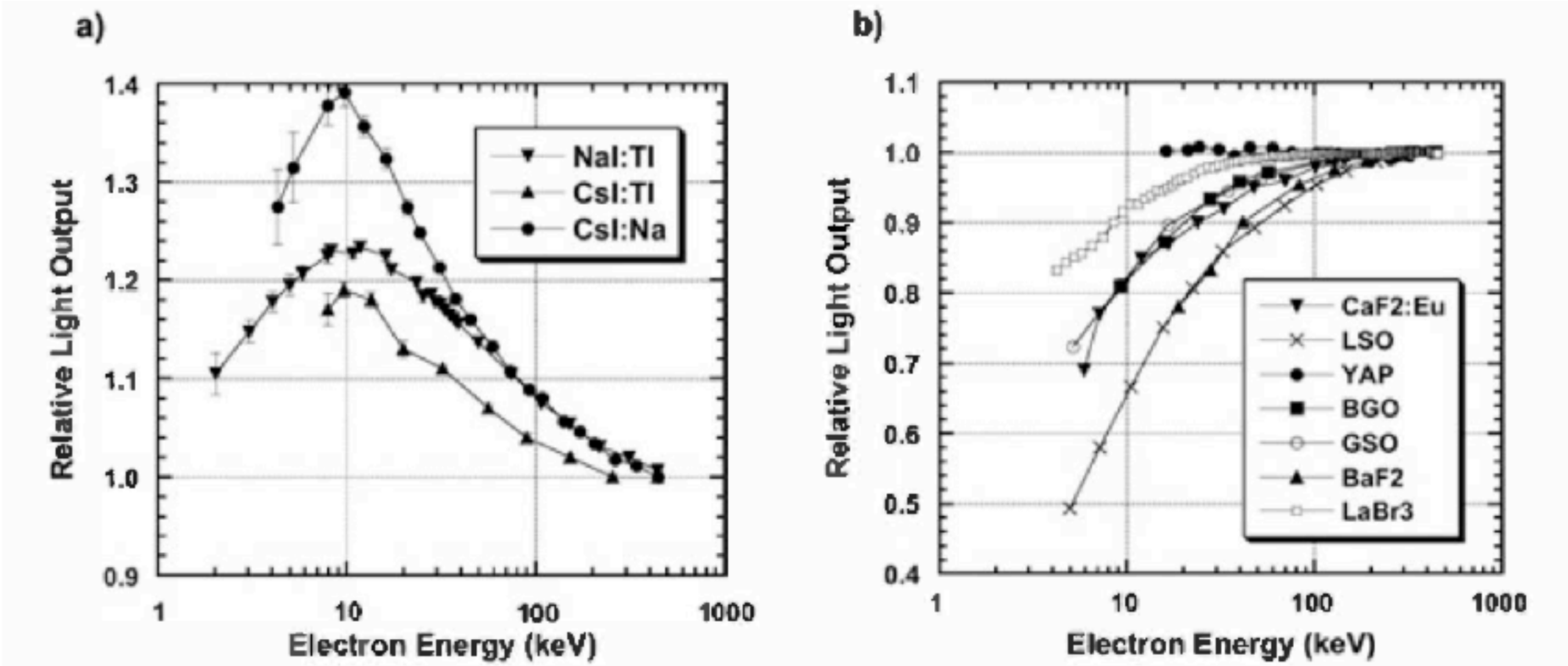

Figure 8.8 The relative scintillation response per unit energy deposited by fast electrons plotted as a function of their energy. The responses are normalized to unity at 445 keV. Perfectly proportional behavior would be a horizontal line passing through 1 on the vertical scale. The alkali halides included in part (*a*) show a peak in their response around 10 keV, whereas the scintillators plotted in part (*b*) show monotonically decreasing yield as the energy is lowered. (Plots courtesy of W. Moses of Lawrence Berkeley National Laboratory. Data derived from Ref. 87 and supplemented with prepublication data obtained using the SLYNCI facility at Lawrence Livermore National Laboratory.)

Scintillation Detector

NaI(Tl)

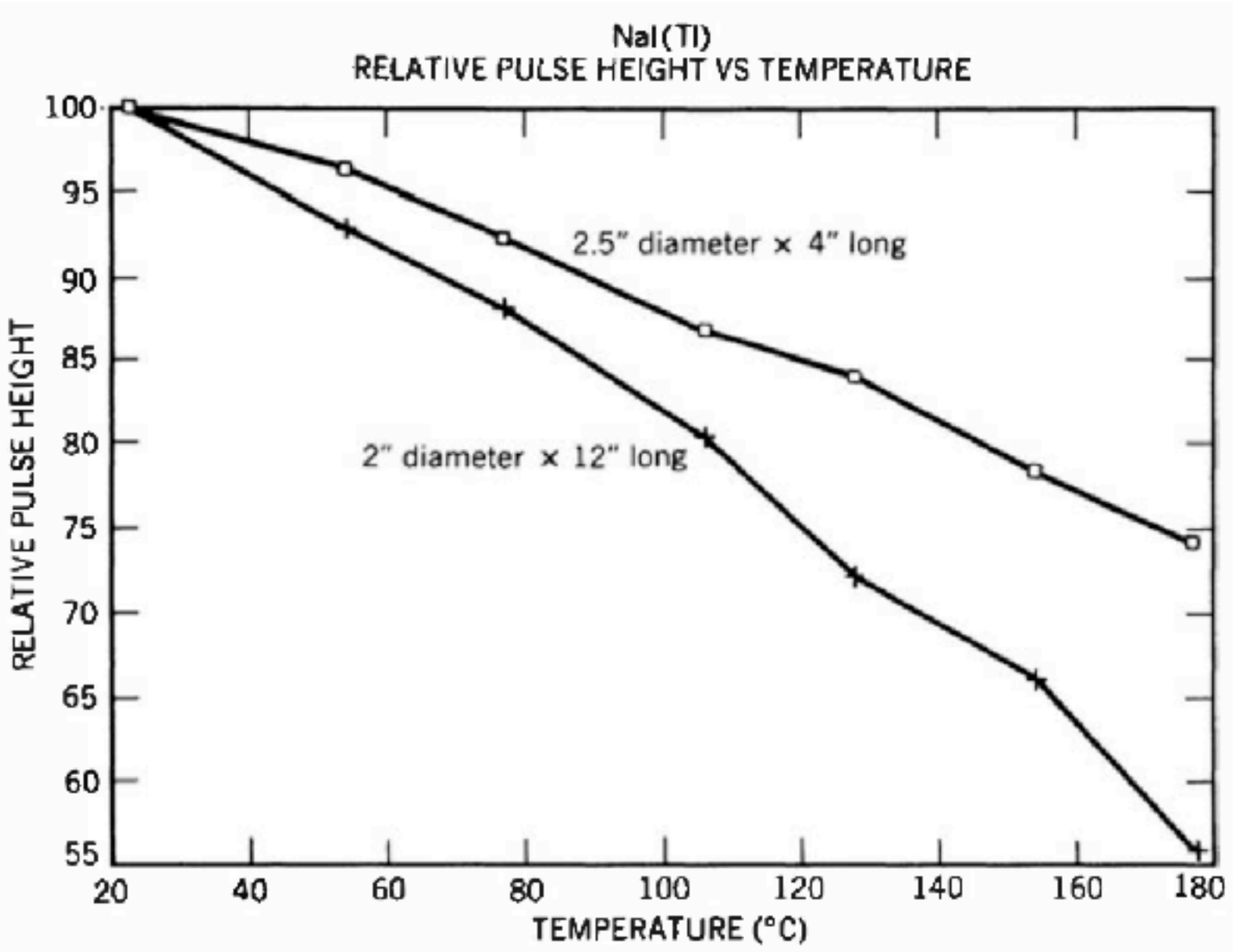

Figure 8.9 The temperature dependence of the light yield measured from two NaI(Tl) crystals. The measurements were made using an oven equipped with a light pipe, and the temperature of the photomultiplier tube was held constant. The difference in behavior between the two crystals is probably due to changes in surface reflectivity. (Data courtesy R. Dayton, Bicron Corporation, Newbury, Ohio.)

Scintillation Detector

NaI(Tl)

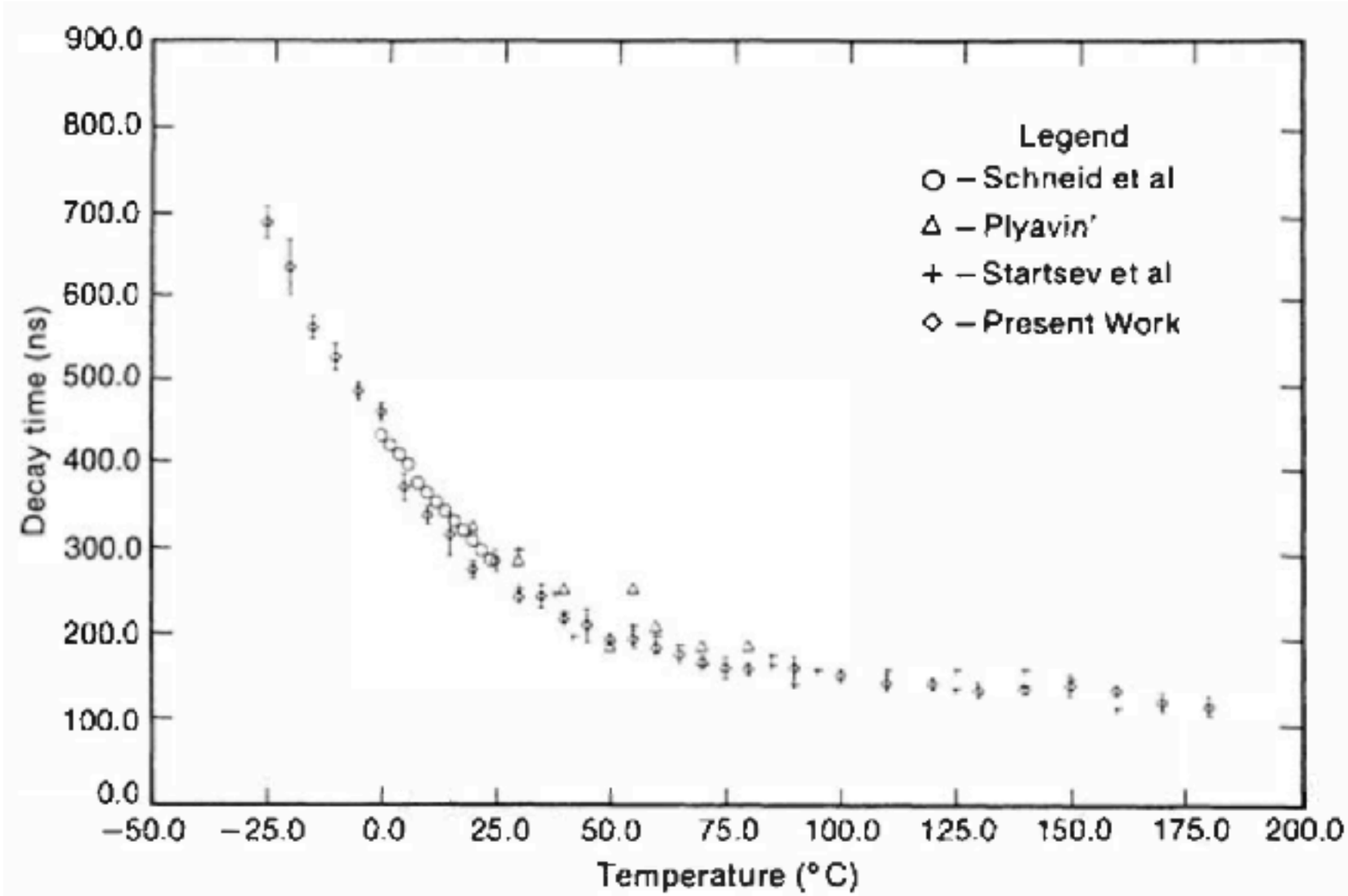

Figure 8.10 Temperature dependence of the scintillation decay time in NaI(Tl). (From Schweitzer and Ziehl.[95])

Scintillation Detector

Bismuth Germinate (BGO)

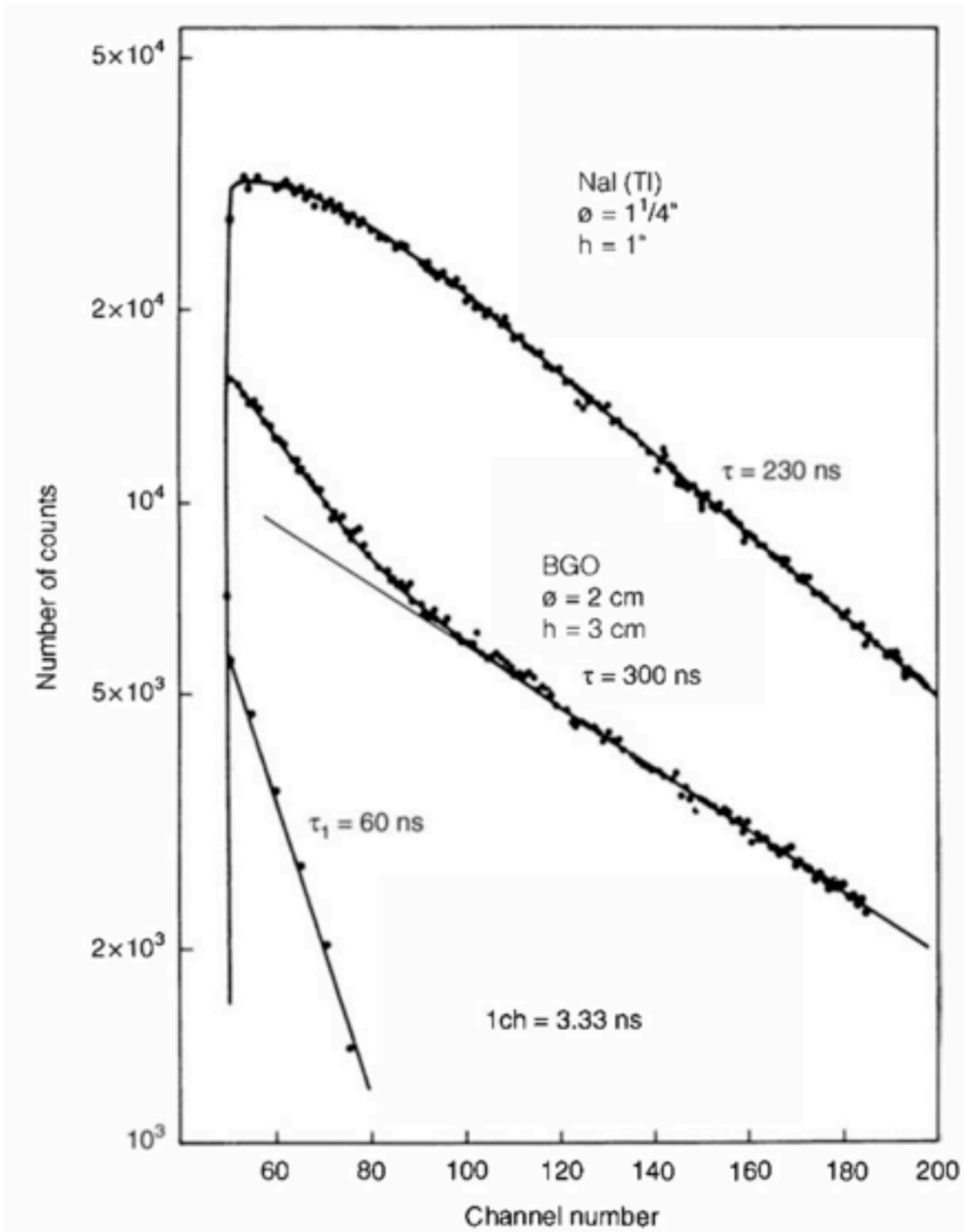

Figure 8.11 Measurements of the light pulse shapes from BGO and NaI(Tl). The abscissa represents time, the ordinate the relative light output. The BGO yield is represented as the sum of separate decay components with 60 and 300 ns decay times. (From Moszynski et al.[114])

Scintillation Detector

Bismuth Germinate (BGO)

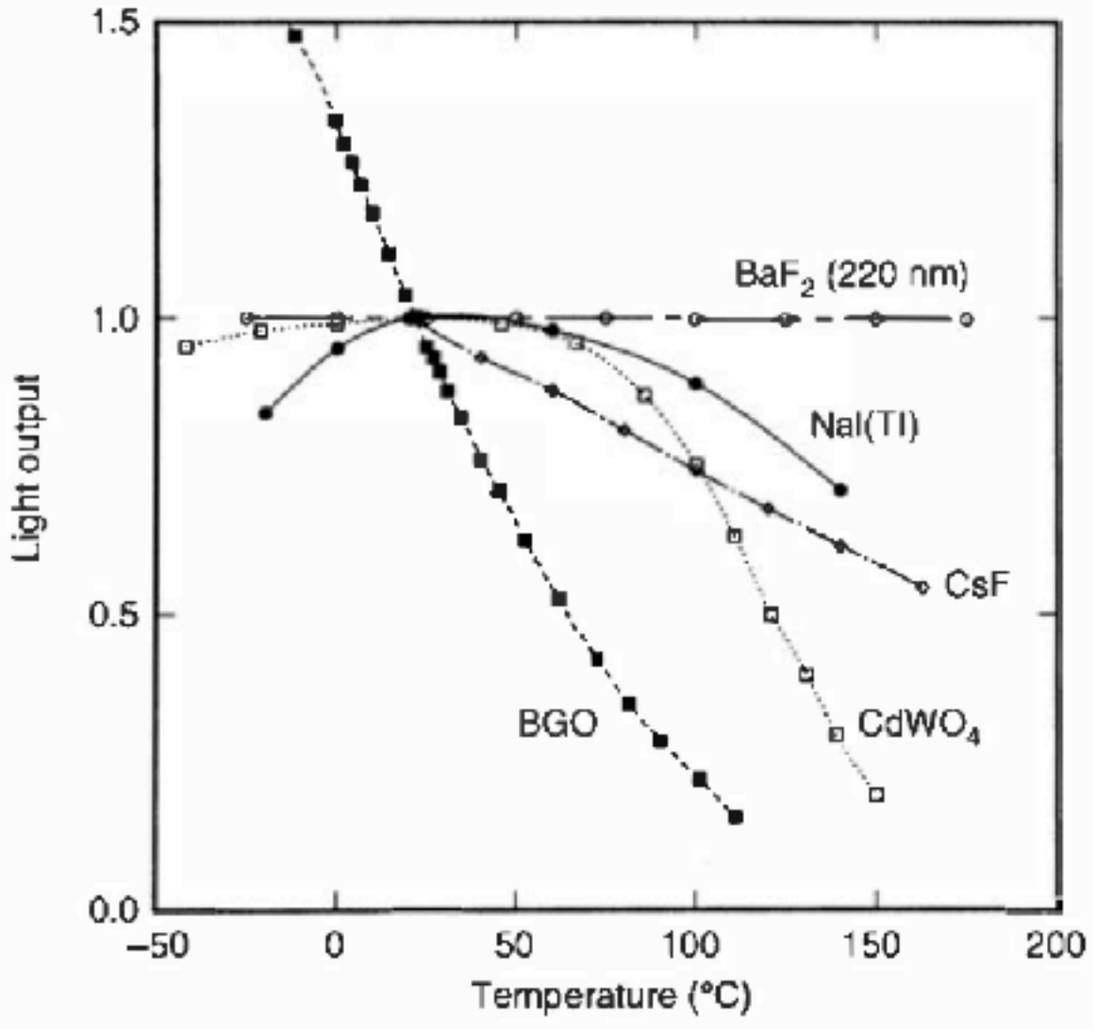

Figure 8.12 The dependence of the light output of some common scintillators as a function of temperature. Only the fast (220 nm) component from BaF_2 is included. (From Melcher.[118])

Scintillation Detector

Barium Fluoride (BaF2)

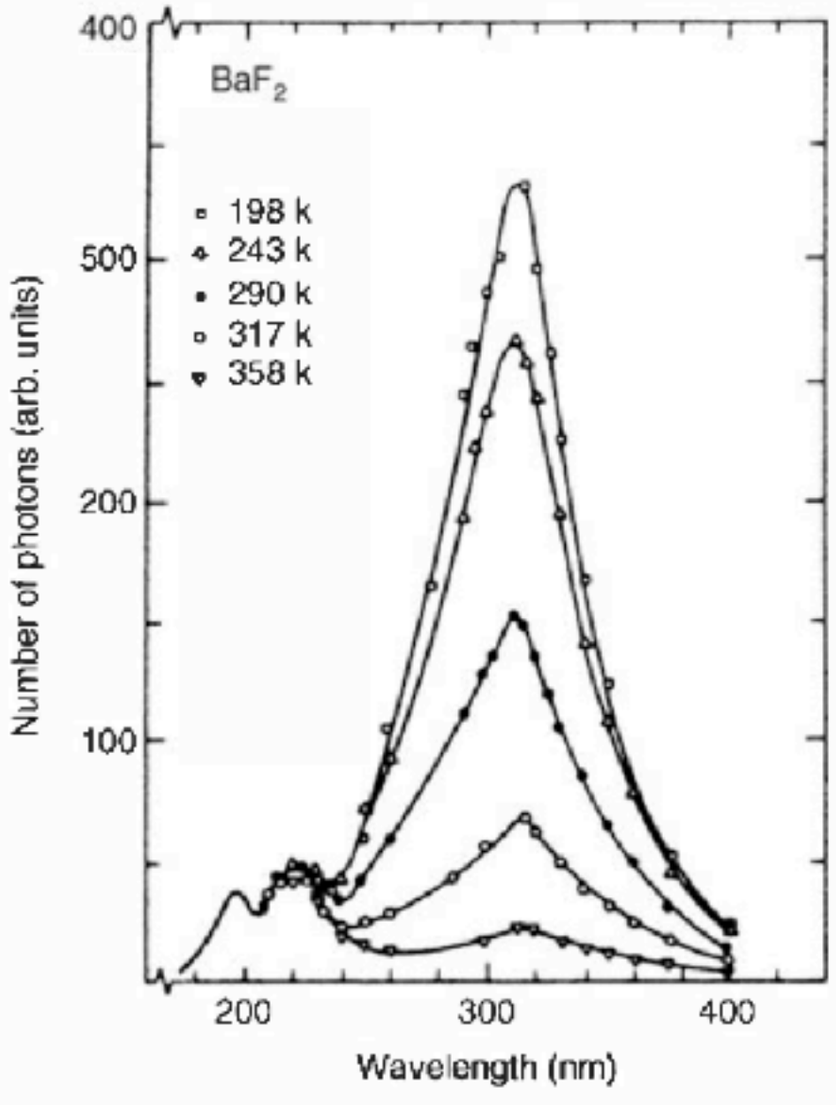

Figure 8.13 The scintillation emission spectra from BaF_2 measured at various temperatures. The fast component (corresponding to the two small peaks at the left) does not display the strong temperature dependence of the slow component. (From Schotanus et al.[133,134])

Scintillation Detector

Noble gas scintillators

Table 8.4 Properties of Gas Scintillators at Atmospheric Pressure

Gas	Mean Wavelength of Emission	Number of Photons with $\lambda > 200$ nm per 4.7 MeV Alpha Particle
Xenon	325 nm	3700
Krypton	318 nm	2100
Argon	250 nm	1100
Helium	390 nm	1100
Nitrogen	390 nm	800
NaI(Tl) (for comparison)	415 nm	41,000

Source: J. B. Birks, *The Theory and Practice of Scintillation Counting.* Copyright 1964 by Pergamon Press, Ltd. Used with permission.

Scintillation Detector

Light collection

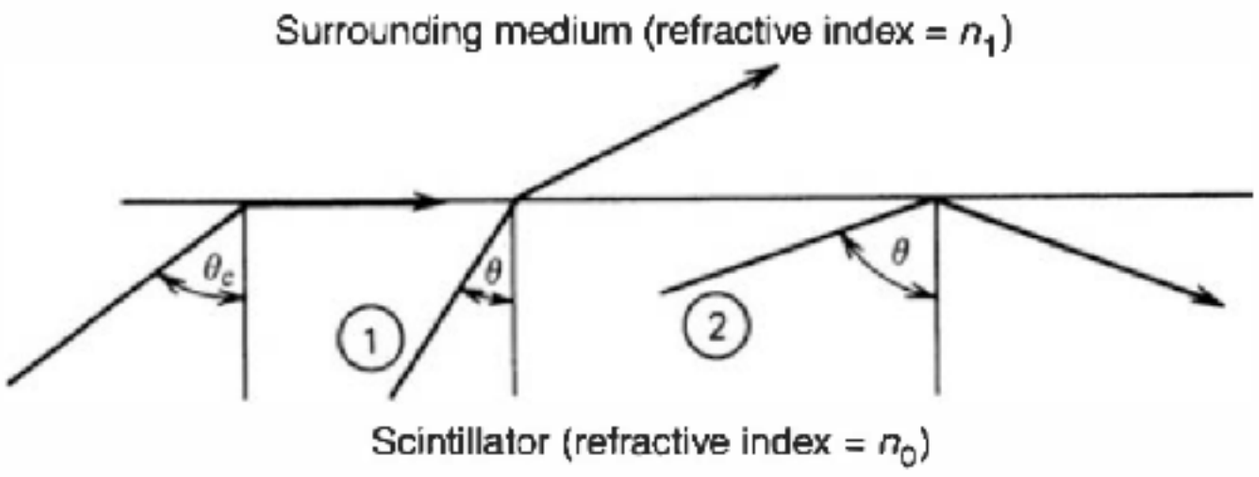

Figure 8.16 Conditions at the interface of dissimilar optical media ($n_0 > n_1$). Ray ① may escape, but ray ② will be internally reflected at the surface.

$$\theta_c = \sin^{-1} \frac{n_1}{n_0}$$

Scintillation Detector

Light pipes

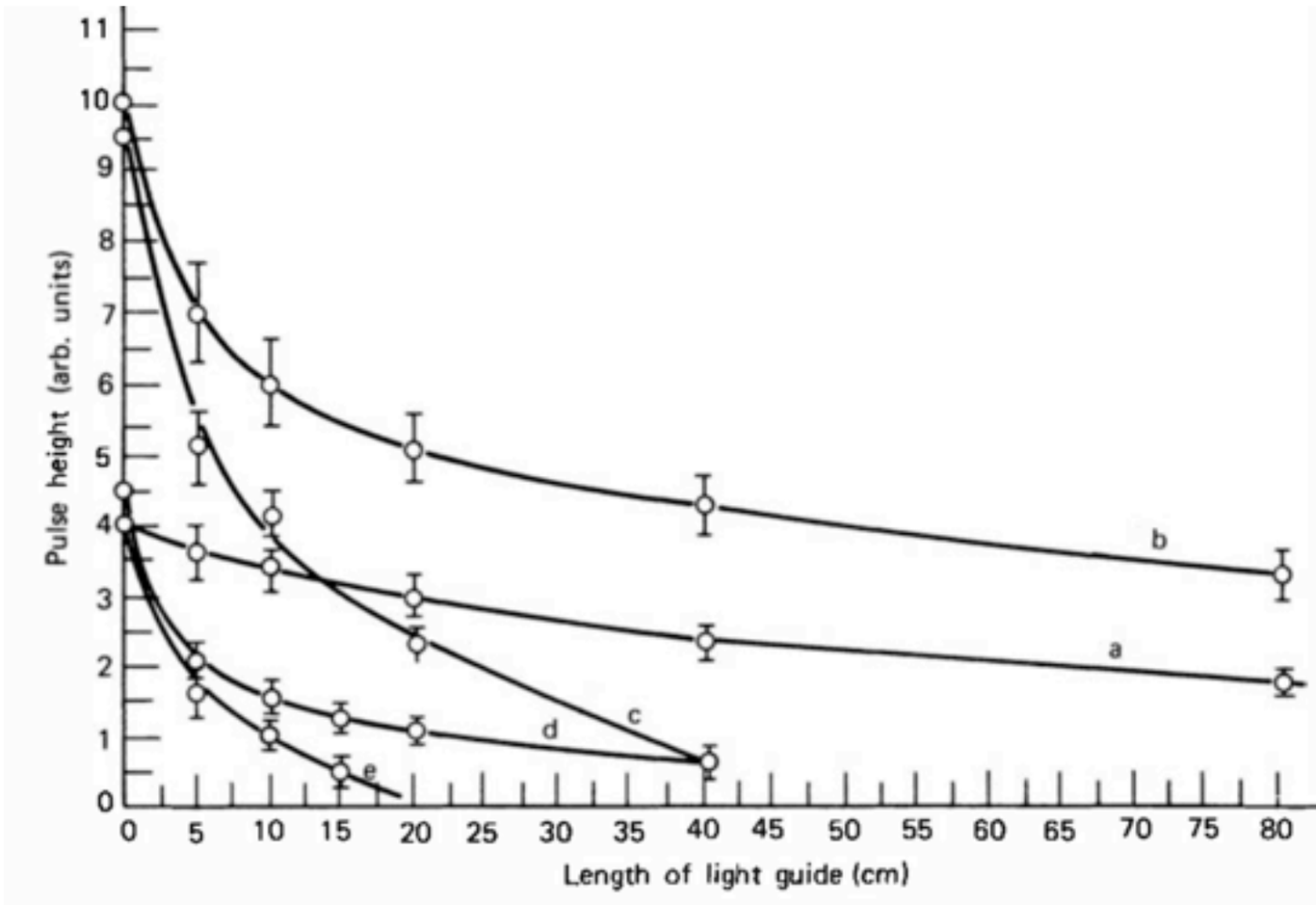

Figure 8.17 Variation of pulse height with length of light guide for various reflective wrappings. (*a*) Total internal reflection only, (*b*) total internal reflection with reflective covering, (*c*) surface of light guide painted with NE 560 reflector paint, (*d*) specular reflector without light guide, (*e*) diffuse reflector without light guide. (From Kilvington et al.[281])

Scintillation Detector

Light pipes

fractional solid angle subtended by this angle ϕ_c is calculated as

$$F = \frac{\Omega}{4\pi} = \frac{1}{4\pi}\int_{\phi=0}^{\phi=\phi_c} d\Omega = \frac{1}{4\pi}\int_0^{\phi_c} 2\pi \sin\phi \, d\phi$$
$$= \frac{1}{2}(1 - \cos\phi_c) = \frac{1}{2}(1 - \sin\theta_c)$$
$$= \frac{1}{2}(1 - n_1/n_0)$$

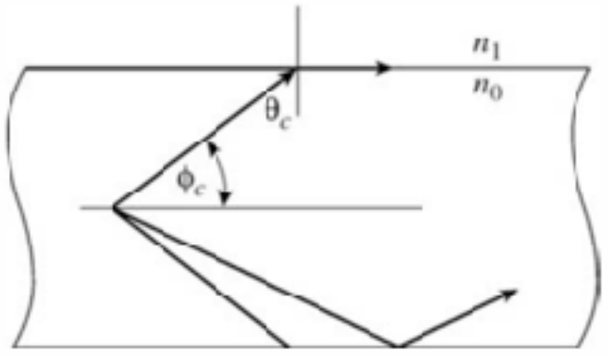

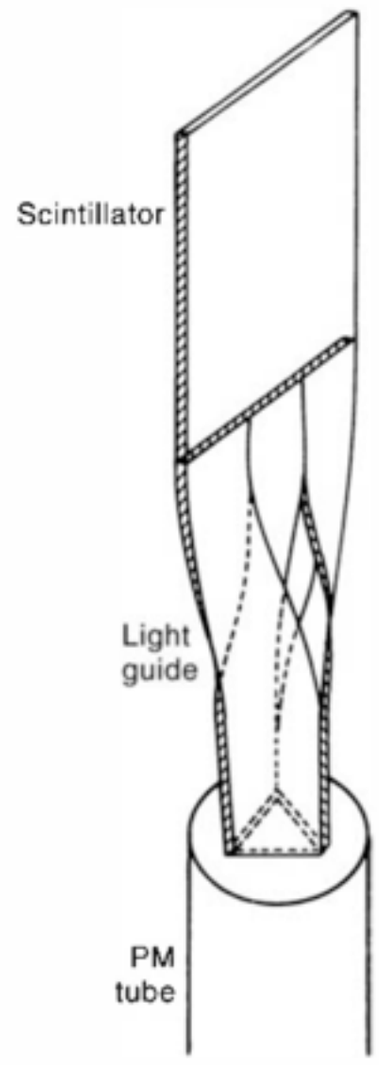

to the slab surfaces, and a vertex angle of θ_c. The total escaping fraction of light is thus given by

$$E = 2 \cdot \frac{\Omega}{4\pi} = \frac{1}{2\pi}\int_{\theta=0}^{\theta=\theta_c} d\Omega = \frac{1}{2\pi}\int_0^{\theta_c} 2\pi \sin\theta \, d\theta$$
$$= 1 - \cos\theta_c = 1 - \sqrt{1 - \left(\frac{n_1}{n_0}\right)^2}$$

The fraction of light trapped in the slab is therefore

$$F = 1 - E = \sqrt{1 - \left(\frac{n_1}{n_0}\right)^2} \qquad (8.15)$$

Scintillation Detector

Fiber scintillators

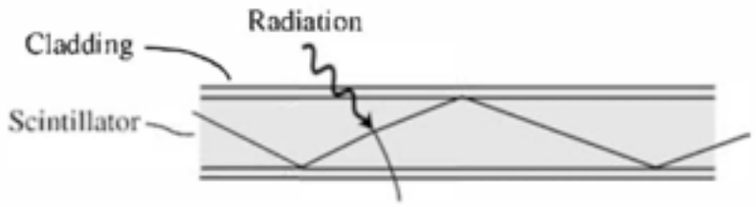

Figure 8.19 Cross section of a typical fiber scintillator. Some fraction of the emitted light is trapped by total internal reflection at the core-cladding interface.

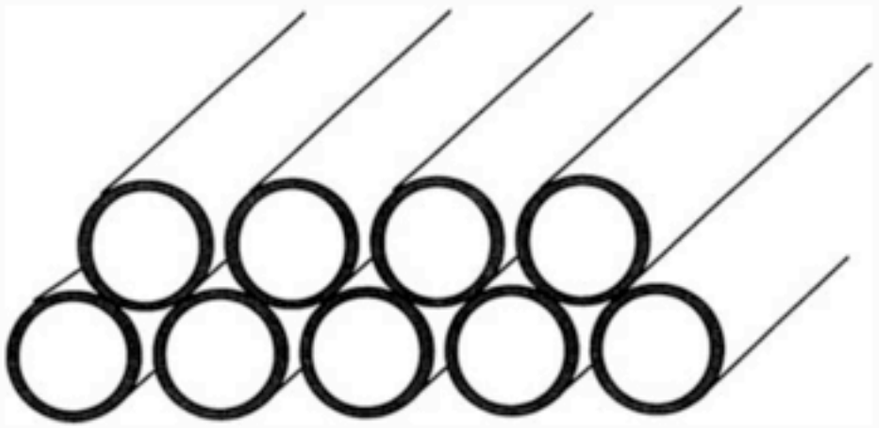

Figure 8.20 A double-layer ribbon made up of fiber scintillators. (From Baumbaugh et al.[229])

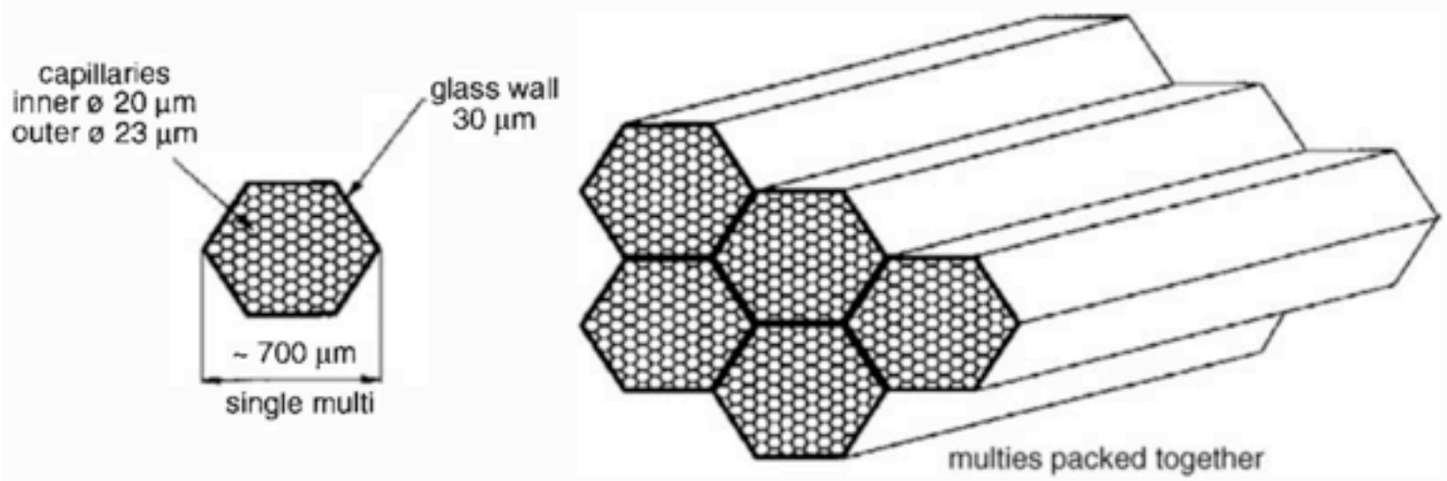

Figure 8.21 Glass capillaries fused into bundles (or "multies") and operated filled with liquid scintillator. (From Ferroni and Martellotti.[300])

Scintillation Detector

Light yield and propagation

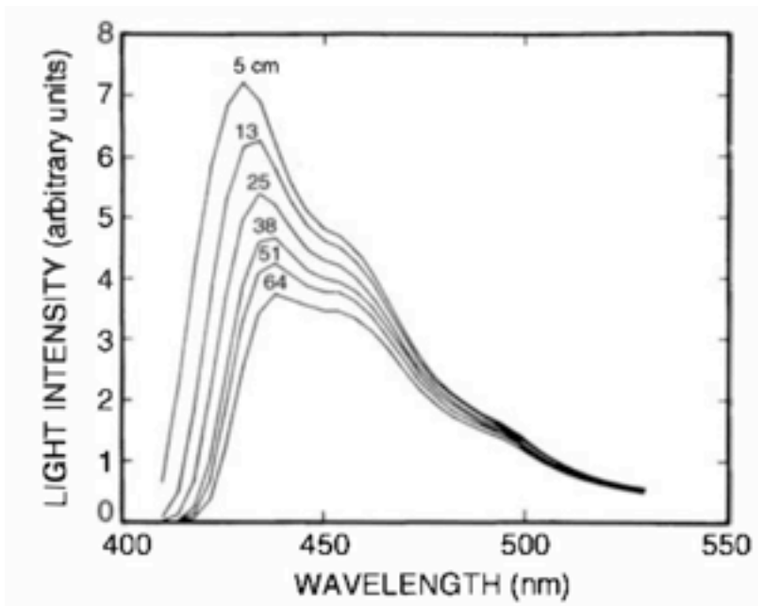

Table 8.5 Typical Light Yield for Fiber Scintillators (for low dE/dx particles, in all directions, will be reduced by light capture fraction)

Core Material	Photons/keV	λ_{peak} (nm)
Glass scintillator	3–5	400
Plastic scintillator	8–10	420
Liquid scintillator	11–13	420
For comparison:		
NaI(Tl)	38	415

Figure 8.23 The spectrum of scintillation light after transmission through various lengths of fiber scintillator, showing the preferential absorption of the shorter wavelengths. (From Davis et al.[311])

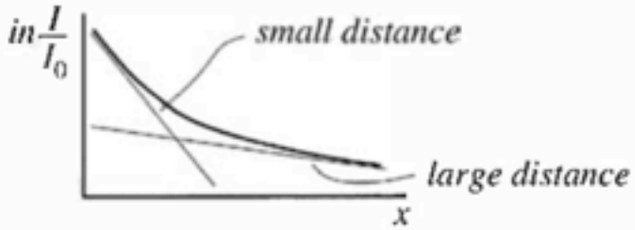

Figure 8.24 The total light transmitted by a fiber as a function of its length. The attenuation length is related to the slope of this plot, and the preferential absorption of the short wavelengths leads to smaller attenuation length for short fibers compared with longer ones.

Photomultiplier Tubes and Photodiodes

Photomultiplier Tubes and Photodiodes

Photomultiplier Tubes

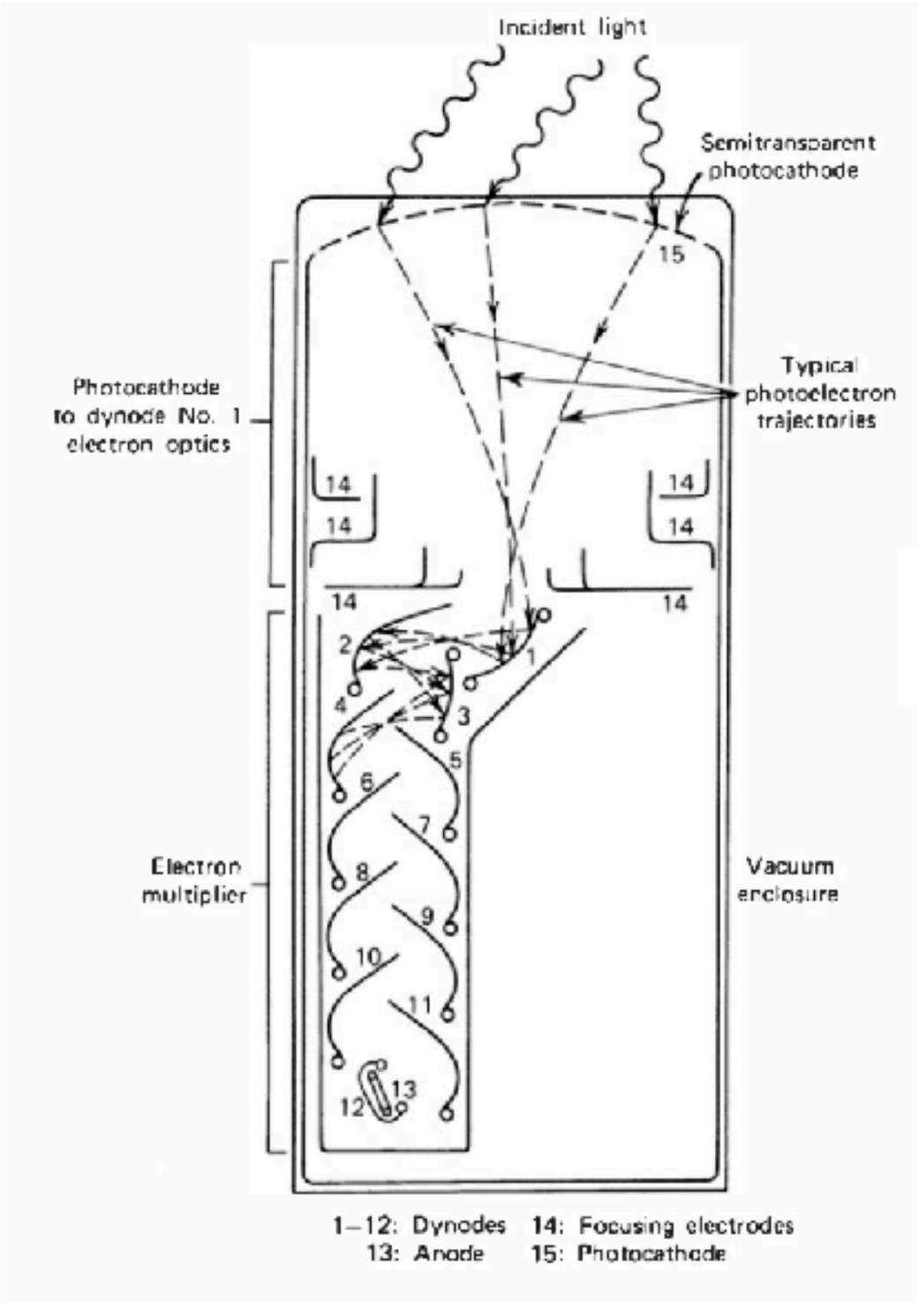

$$\mathrm{QE} = \frac{\text{number of photoelectrons emitted}}{\text{number of incident photons}}$$

Photomultiplier Tubes and Photodiodes

Photocathode

1.Photoemission Process
2.Spontaneous Electron Emission
3.Fabrication of Photocathodes
4.Quantum Efficiency and Spectral Response

Photomultiplier Tubes and Photodiodes

Electron multiplication

1.Secondary Electron Emission
2.Negative Electron Affinity Materials
3.Multiple Stage Multiplication
4.Statistics of Electron Multiplication

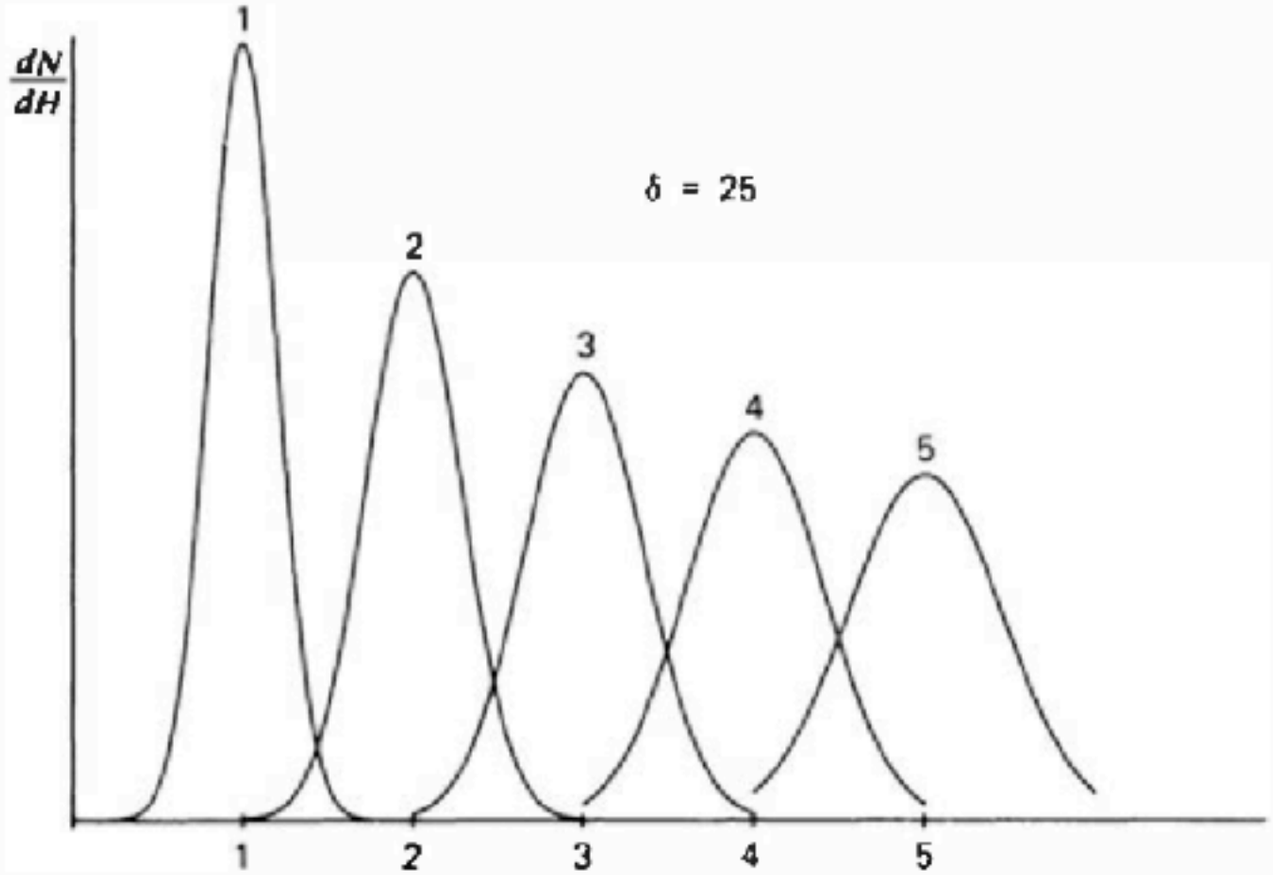

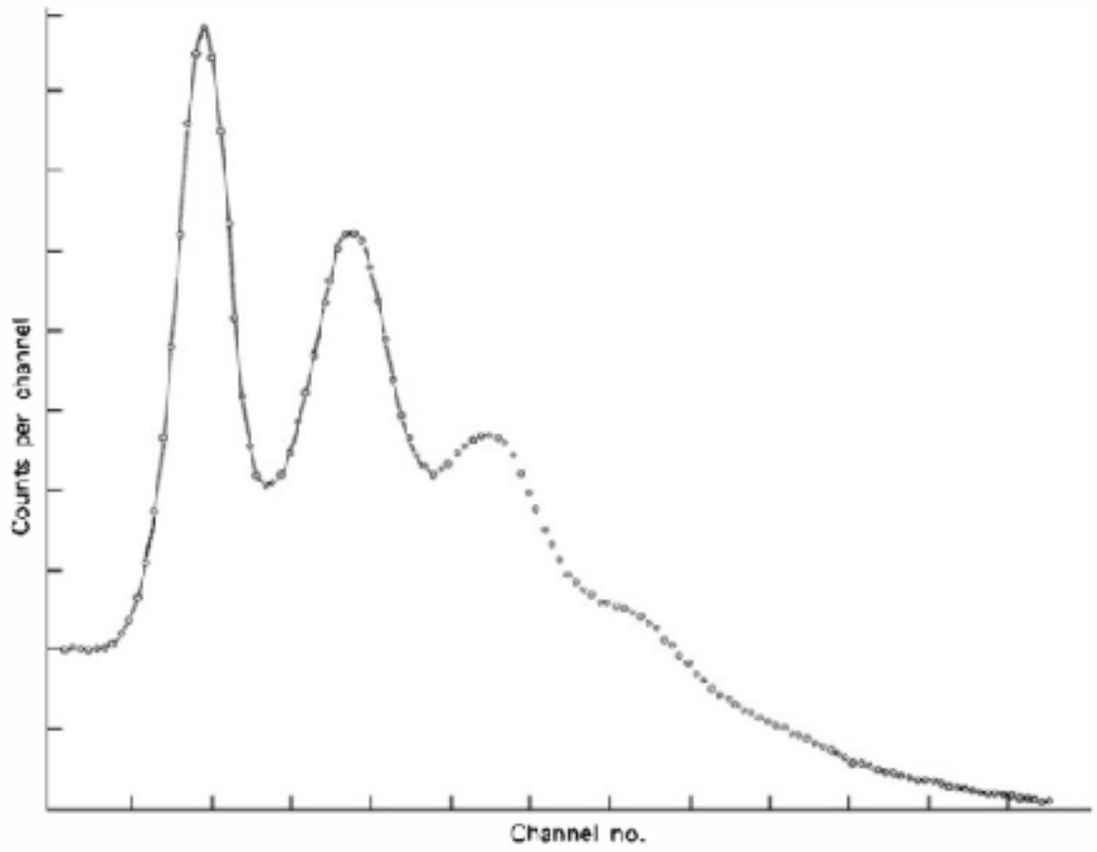

Photomultiplier Tubes and Photodiodes

Structural Differences

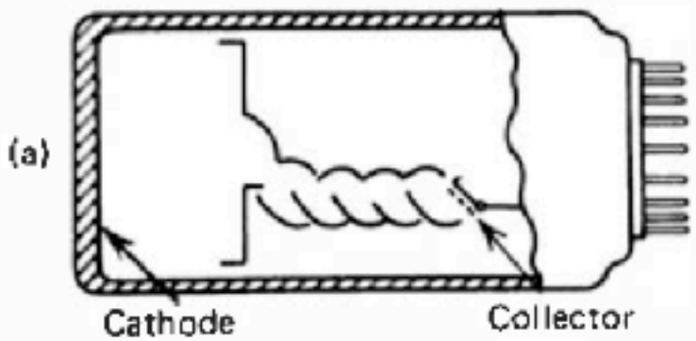

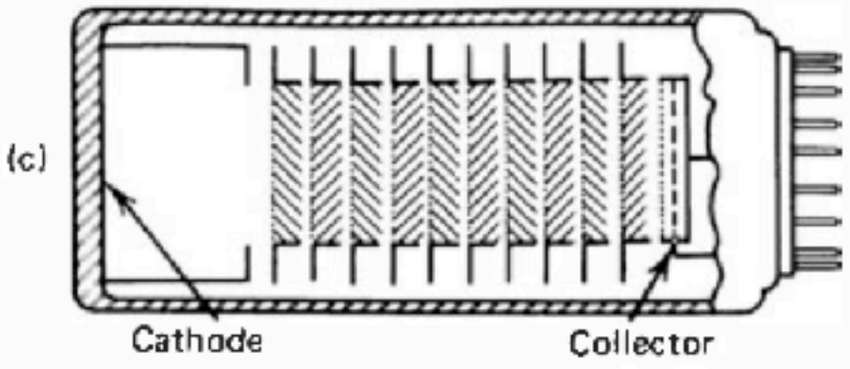

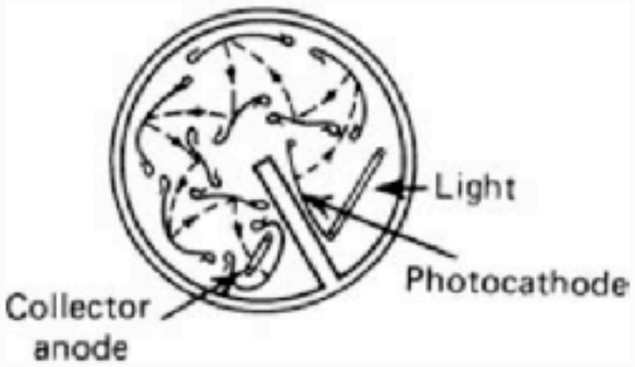

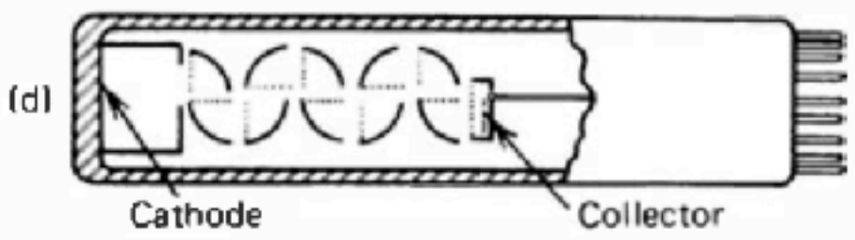

Figure 9.7 Configurations of some common types of PM tubes. (*a*) Focused linear structure. (*b*) Circular grid. (*c*) Venetian blind. (*d*) Box-and-grid. (Courtesy of EMI GENCOM Inc., Plainview, NY.)

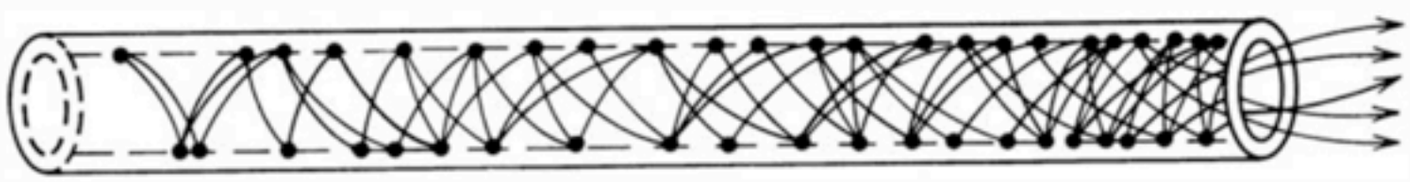

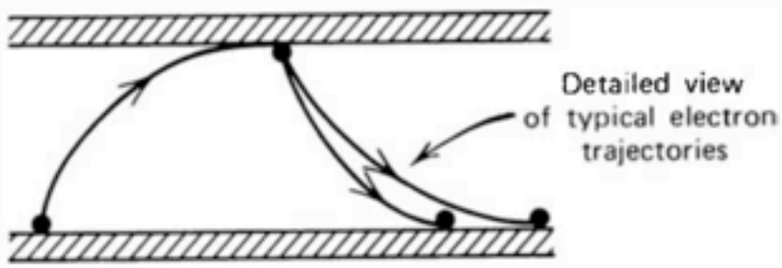

Figure 9.8 Continuous channel electron multiplier.

Photomultiplier Tubes and Photodiodes

Structural Differences

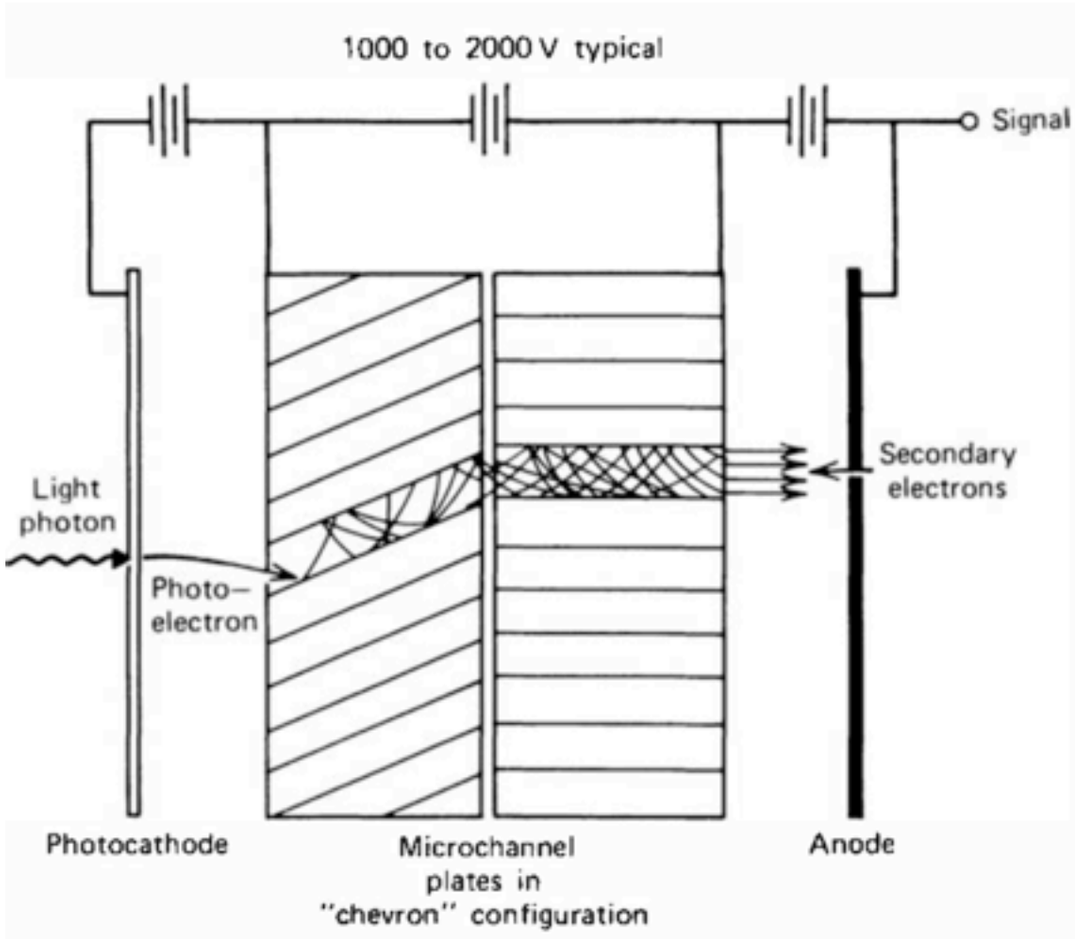

Figure 9.9 Elements of a PM tube based on microchannel plate electron multiplication.

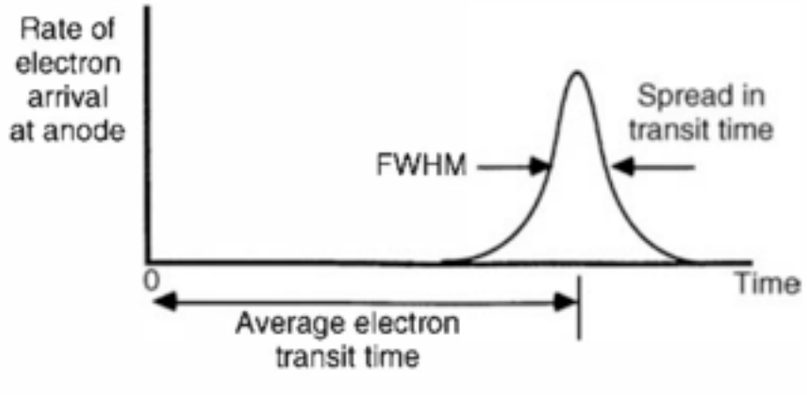

Figure 9.10 The response of a PM tube to a short pulse of light on the photocathode.

Radiation Spectroscopy with Scintillators

Radiation Spectroscopy with Scintillators

Gamma-ray interactions

Photoelectric Effect

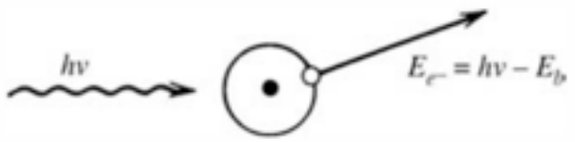

Compton Scattering

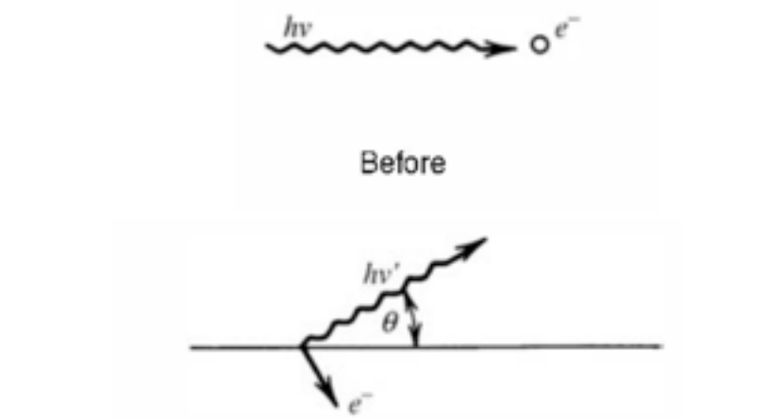

$$h\nu' = \frac{h\nu}{1 + (h\nu/m_0c^2)(1 - \cos\theta)}$$

$$E_{e^-} = h\nu - h\nu' = h\nu\left(\frac{(h\nu/m_0c^2)(1 - \cos\theta)}{1 + (h\nu/m_0c^2)(1 - \cos\theta)}\right)$$

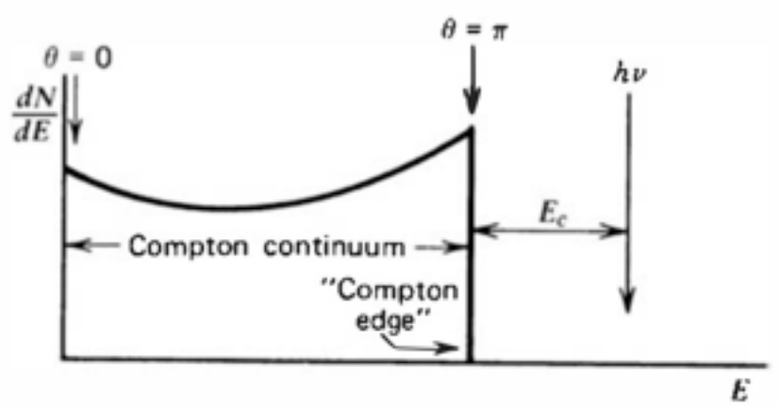

Pair Production

$$E_{e^-} + E_{e^+} = h\nu - 2m_0c^2$$

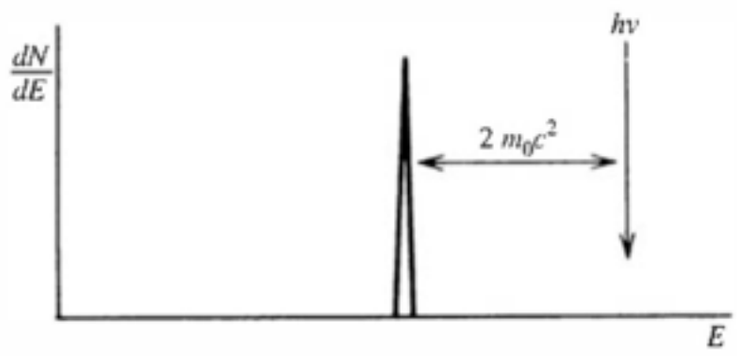

Radiation Spectroscopy with Scintillators

Small detector

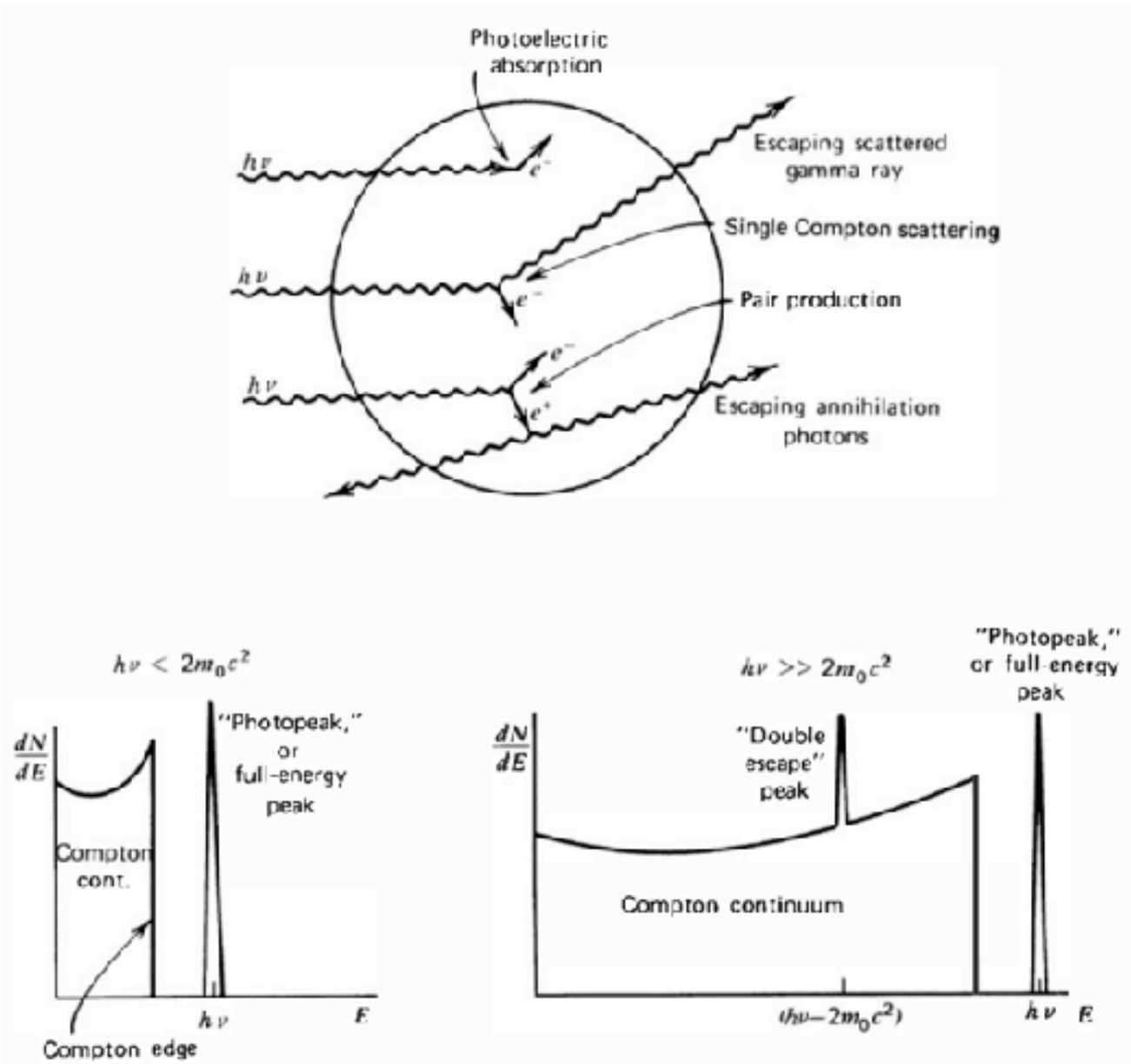

Large detector

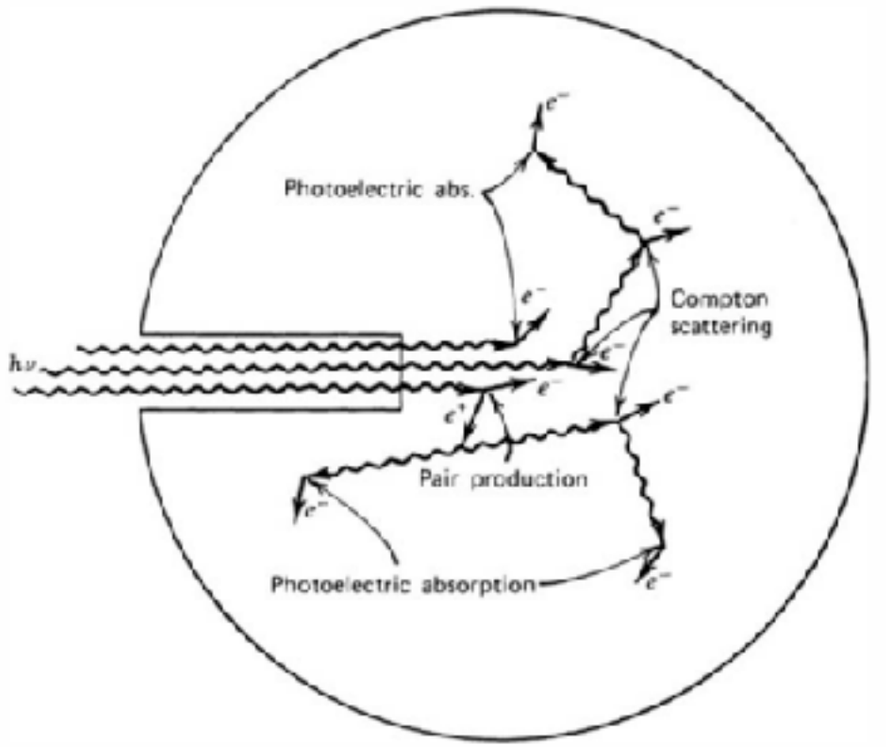

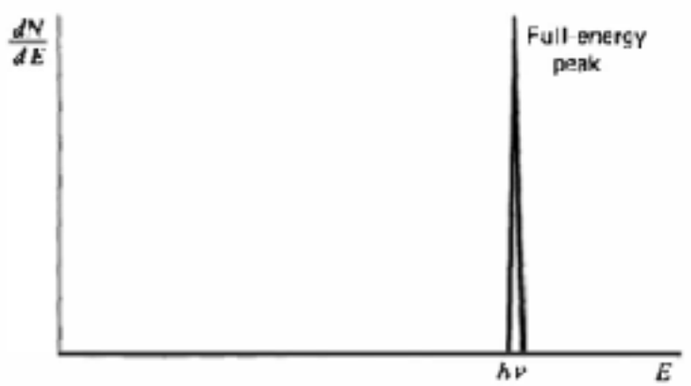

Radiation Spectroscopy with Scintillators

Effect of surrounding materials

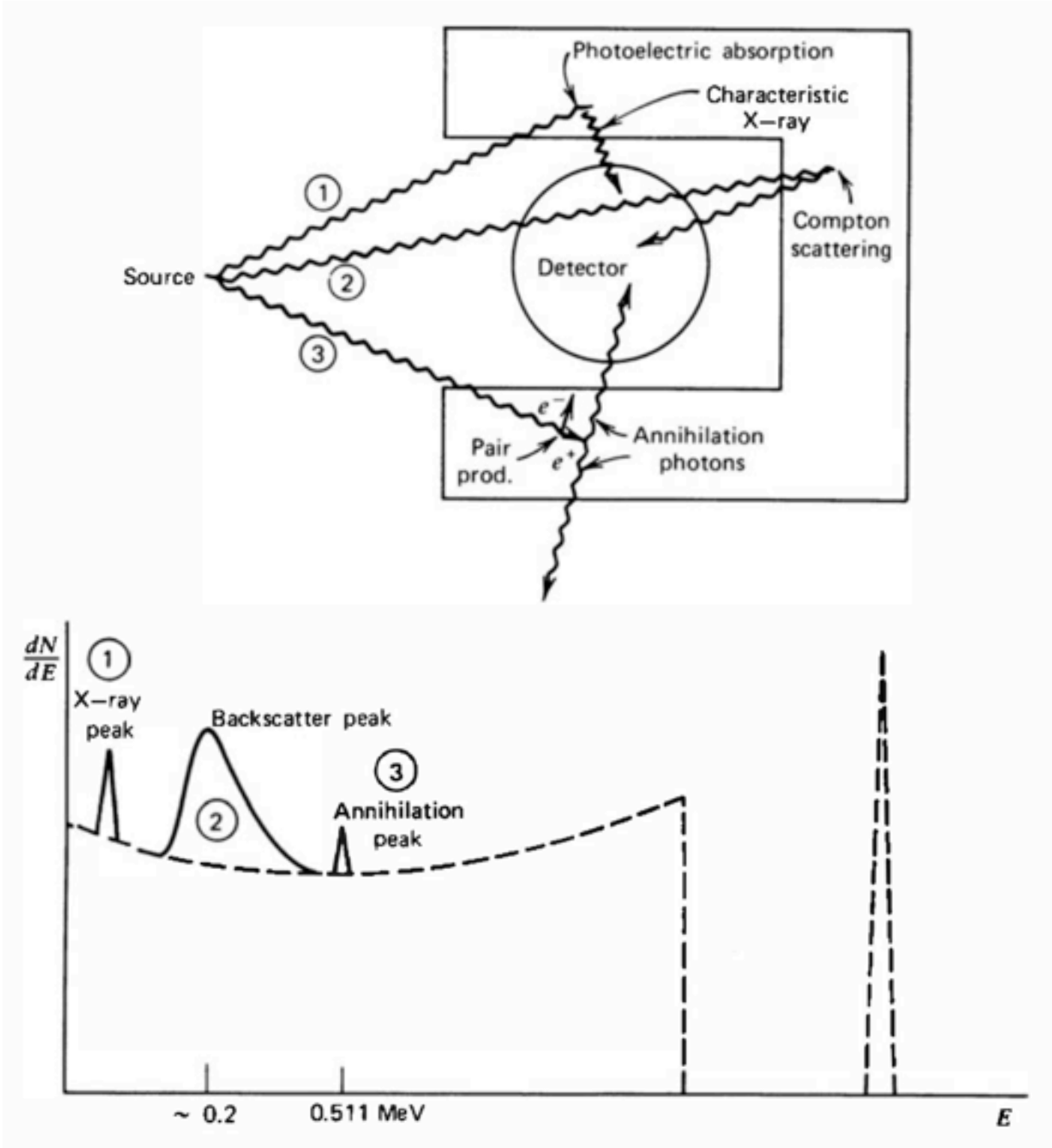

Semiconductor Diode Detectors

Semiconductor Diode Detectors

Charge Carriers

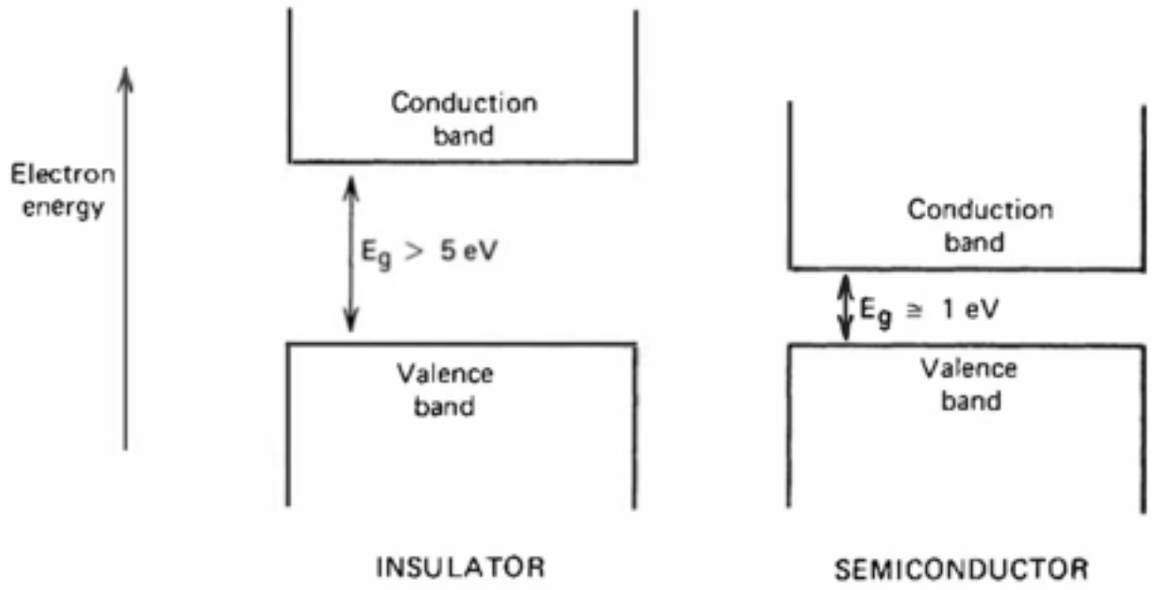

Figure 11.1 Band structure for electron energies in insulators and semiconductors.

The probability per unit time that an electron–hole pair is thermally generated is given by

$$p(T) = CT^{3/2} \exp\left(-\frac{E_g}{2kT}\right) \tag{11.1}$$

where
T = absolute temperature
E_g = bandgap energy
k = Boltmann constant
C = proportionality constant characteristic of the material

Semiconductor Diode Detectors

N and P-type semiconductor

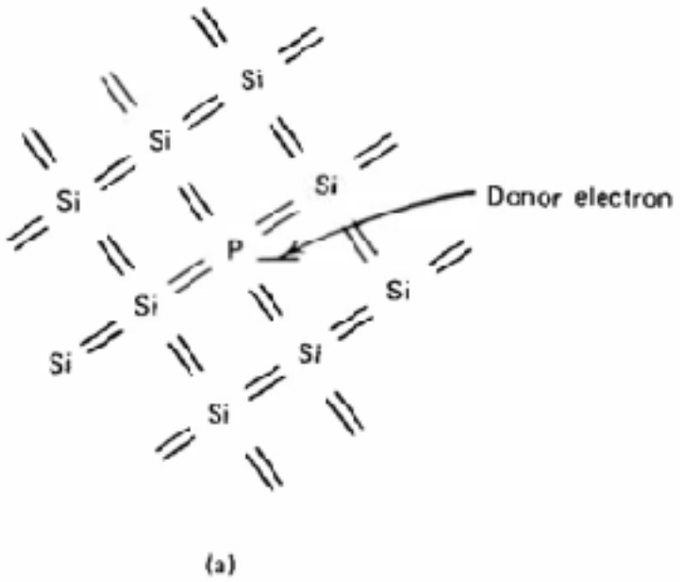

(a)

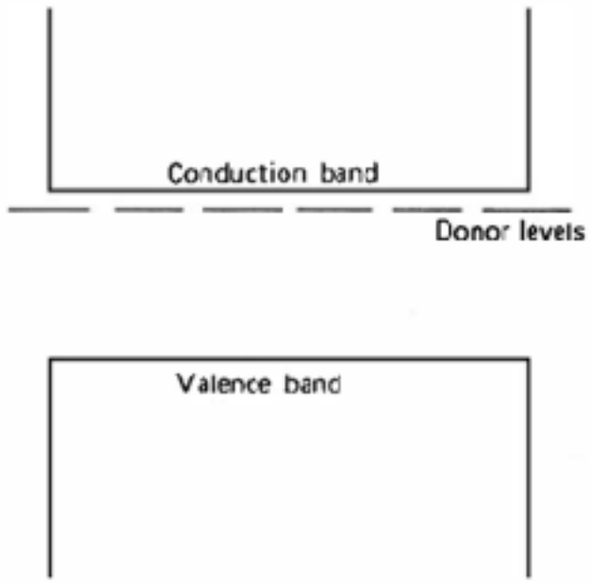

(b)

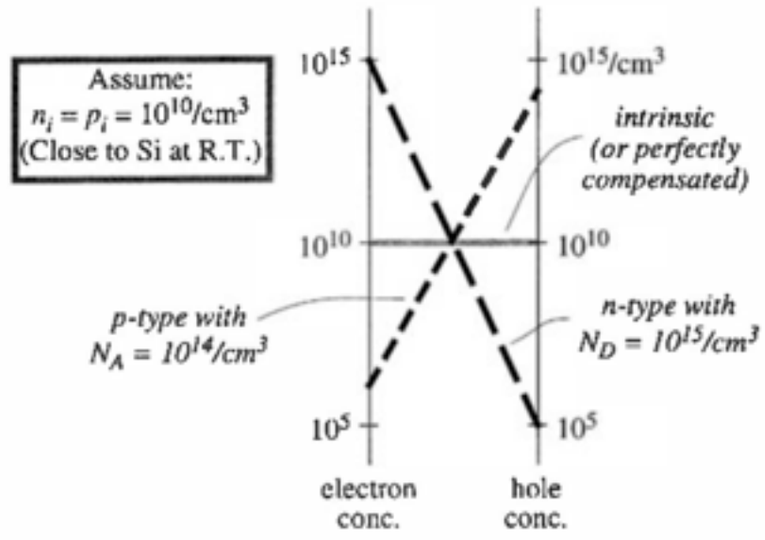

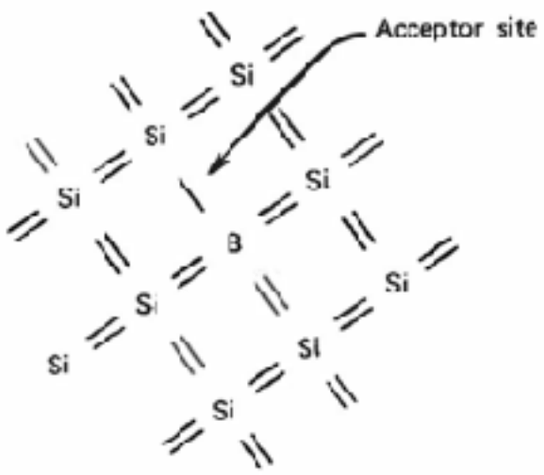

(a)

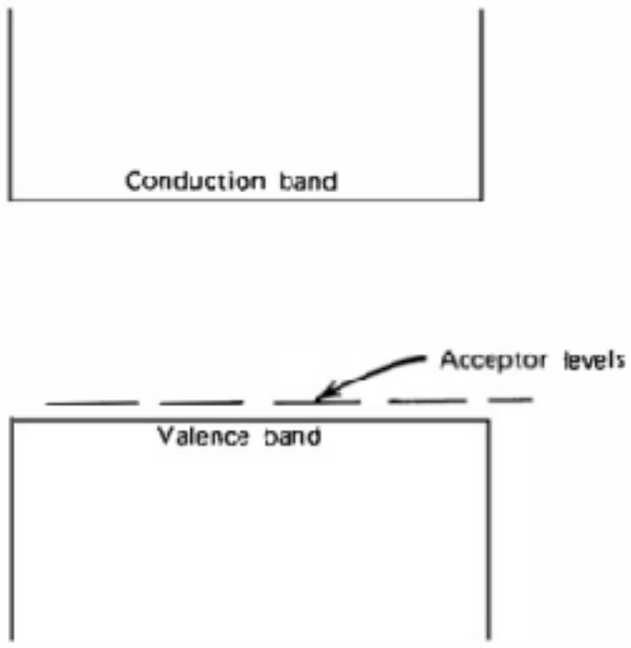

(b)

Germanium Gamma-Ray Detectors

Germanium Gamma-Ray Detectors

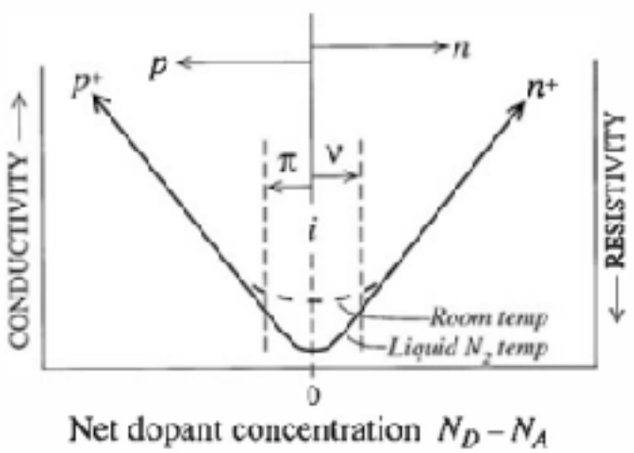

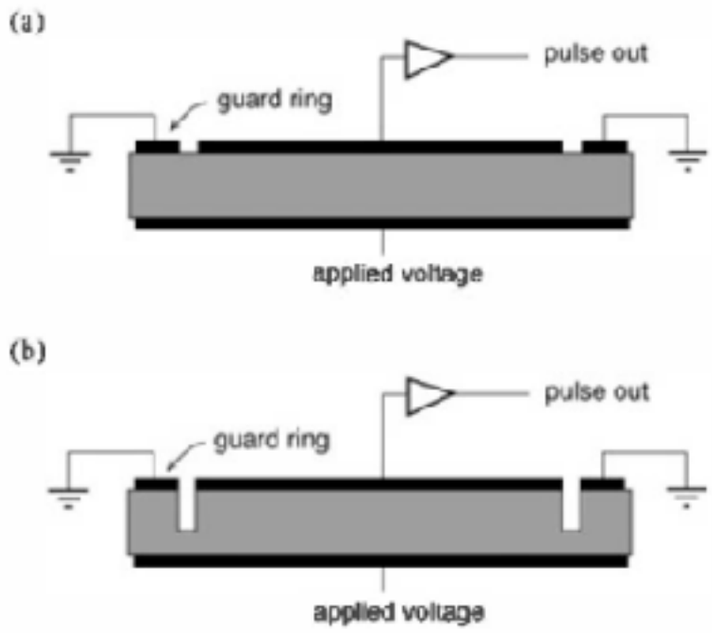

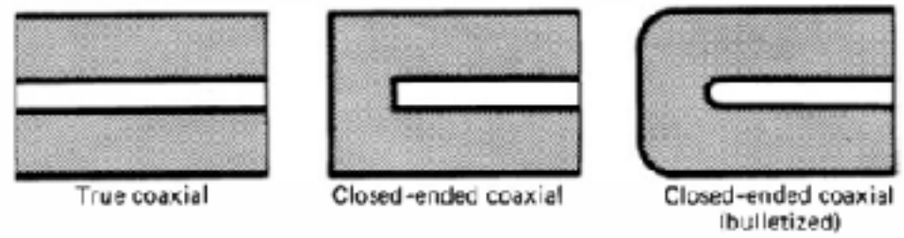

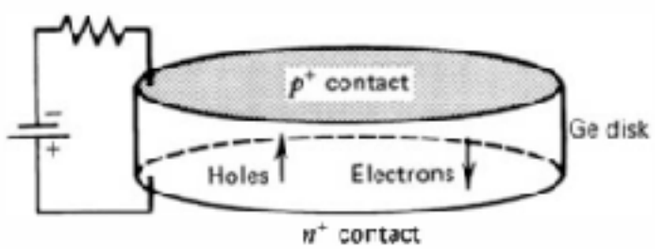

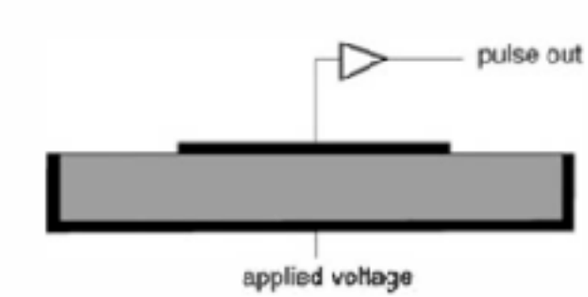

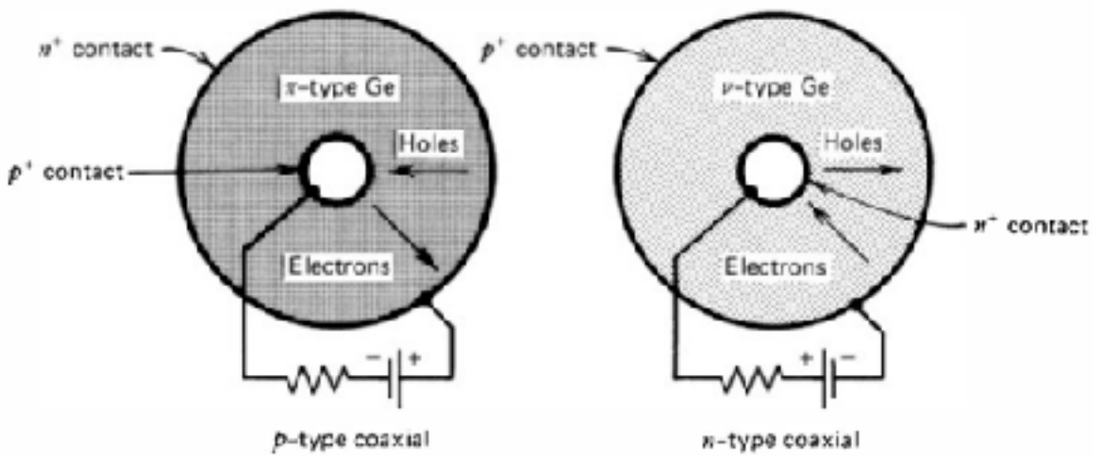

Germanium Gamma-Ray Detectors

Detector crystal dewar

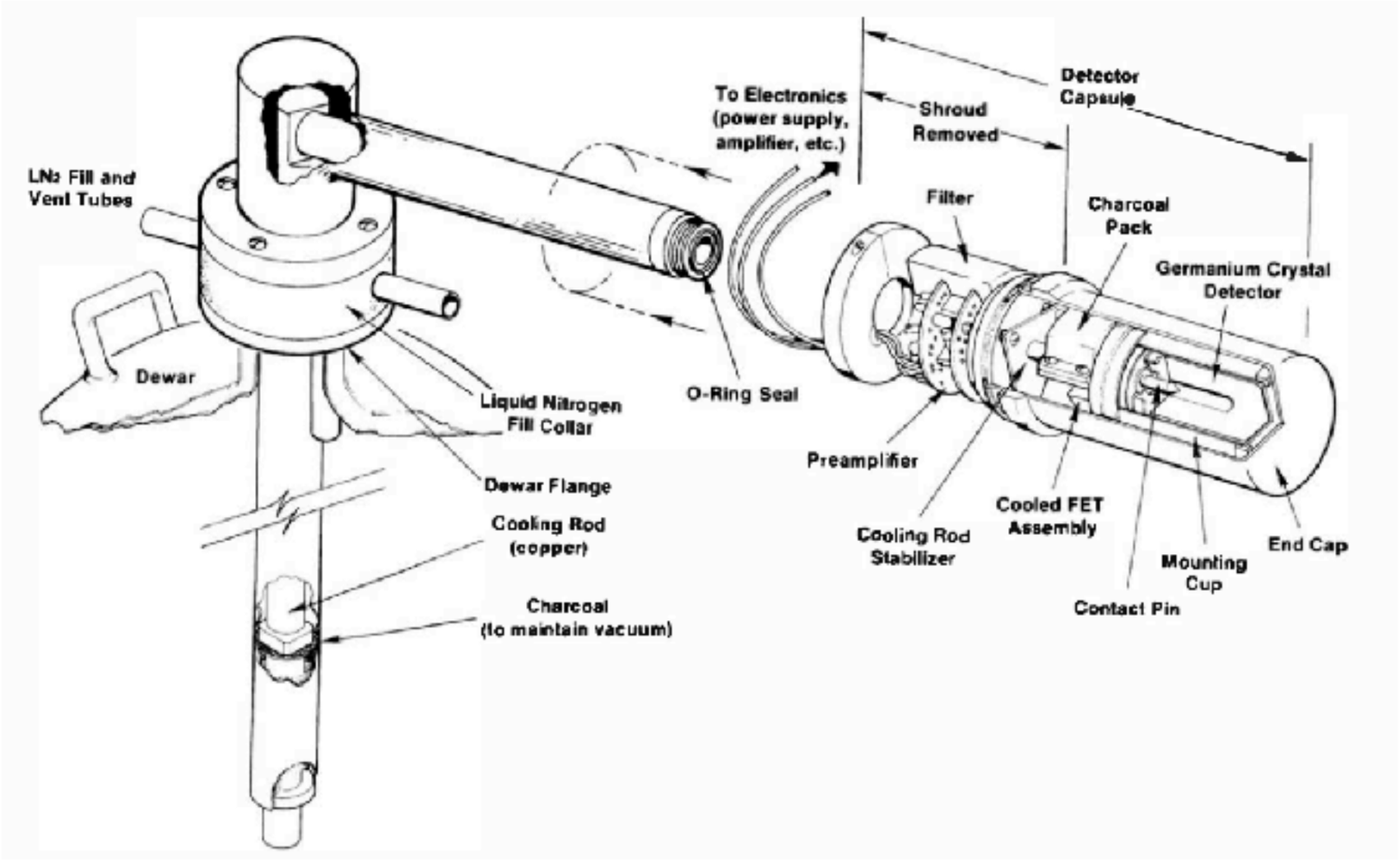

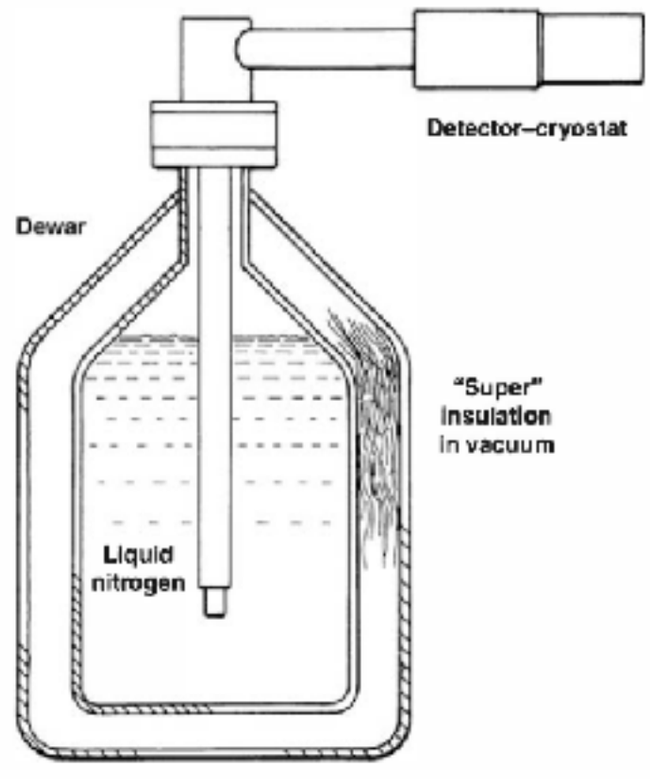

Germanium Gamma-Ray Detectors

Energy resolution

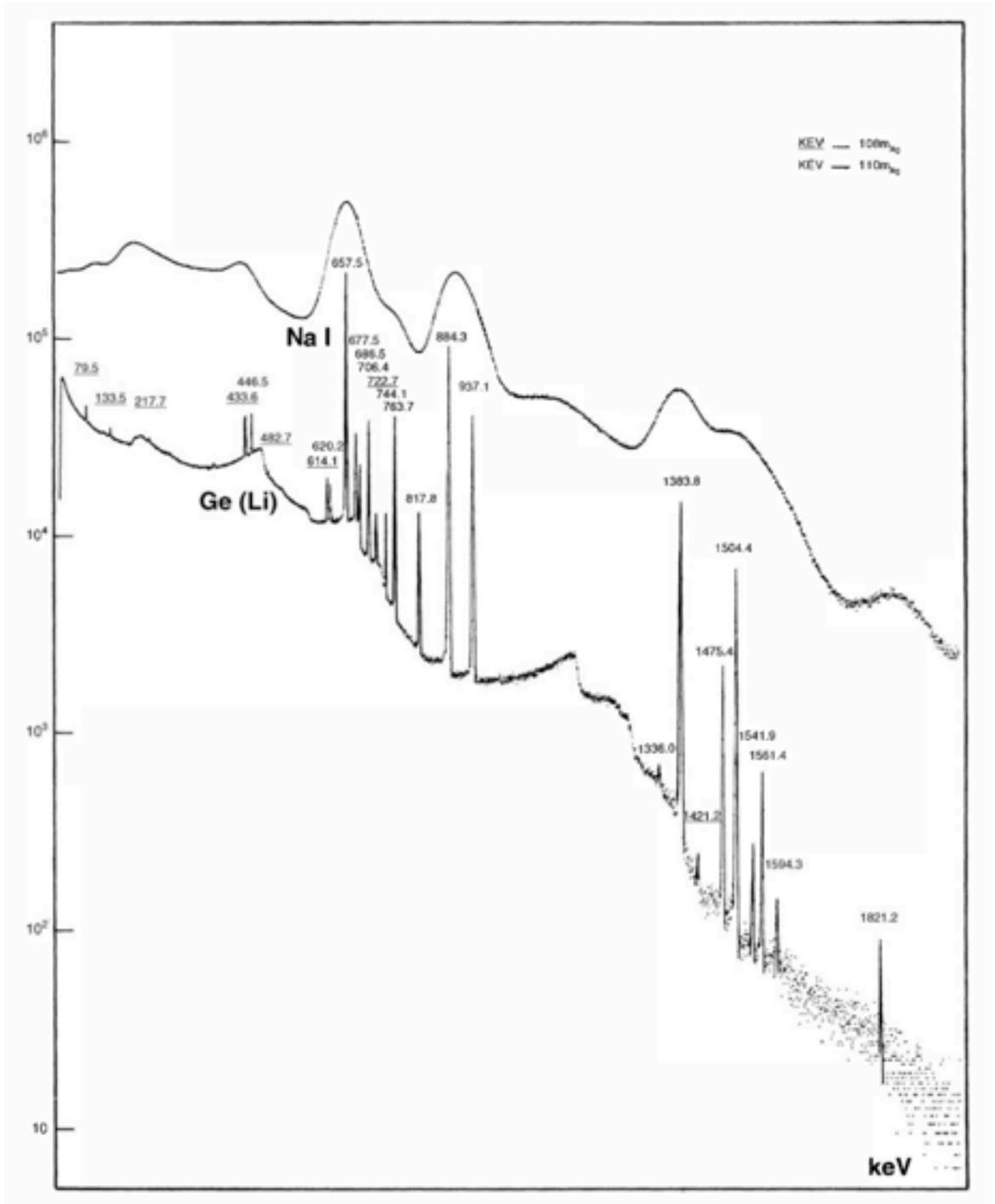

Neutron Detectors

Neutron Detectors

Nuclear reaction

$$\text{target nucleus} + \text{neutron} \rightarrow \begin{cases} \text{recoil nucleus} \\ \text{proton} \\ \text{alpha particle} \\ \text{fission fragments} \end{cases}$$

Neutron Detectors

Boron : ^{10}B(n,alpha)

$$^{10}_{5}\mathrm{B} + ^{1}_{0}\mathrm{n} \rightarrow \begin{cases} ^{7}_{3}\mathrm{Li} + ^{4}_{2}\alpha & 2.792\,\mathrm{MeV\ (ground\ state)} \\ ^{7}_{3}\mathrm{Li}^{*} + ^{4}_{2}\alpha & 2.310\,\mathrm{MeV\ (excited\ state)} \end{cases}$$

(Q-value)

Lithium : ^{6}Li(n,alpha)

$$^{6}_{3}\mathrm{Li} + ^{1}_{0}\mathrm{n} \rightarrow ^{3}_{1}\mathrm{H} + ^{4}_{2}\alpha \qquad \frac{Q\text{-value}}{4.78\,\mathrm{MeV}}$$

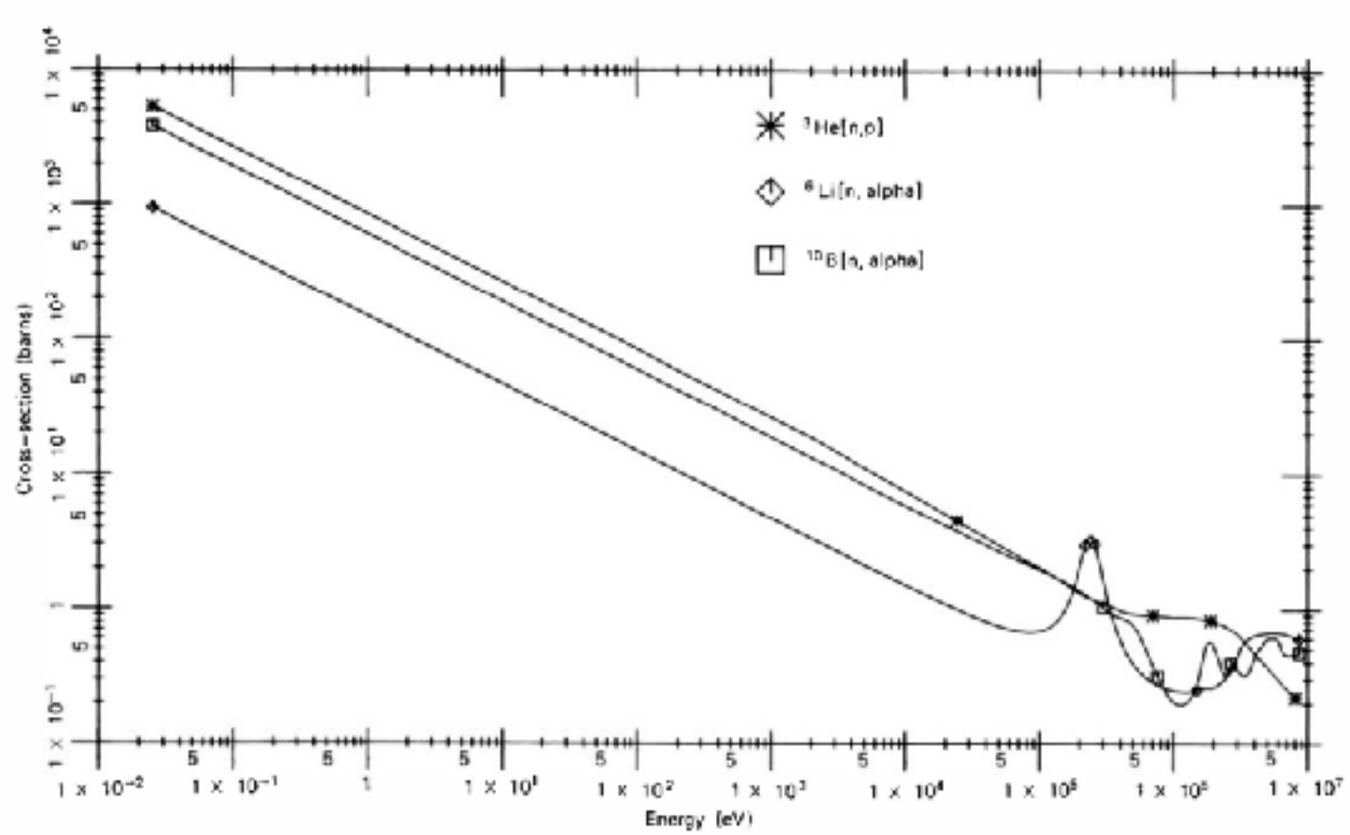

Figure 14.1 Cross section versus neutron energy for some reactions of interest in neutron detection.

Helium : ^{3}He(n,p)

$$^{3}_{2}\mathrm{He} + ^{1}_{0}\mathrm{n} \rightarrow ^{3}_{1}\mathrm{H} + ^{1}_{1}\mathrm{p} \qquad \frac{Q\text{-value}}{0.764\,\mathrm{MeV}}$$

Gadolinium Neutron Capture

Neutron-Induced Fission

Neutron Detectors

Fission cross sections

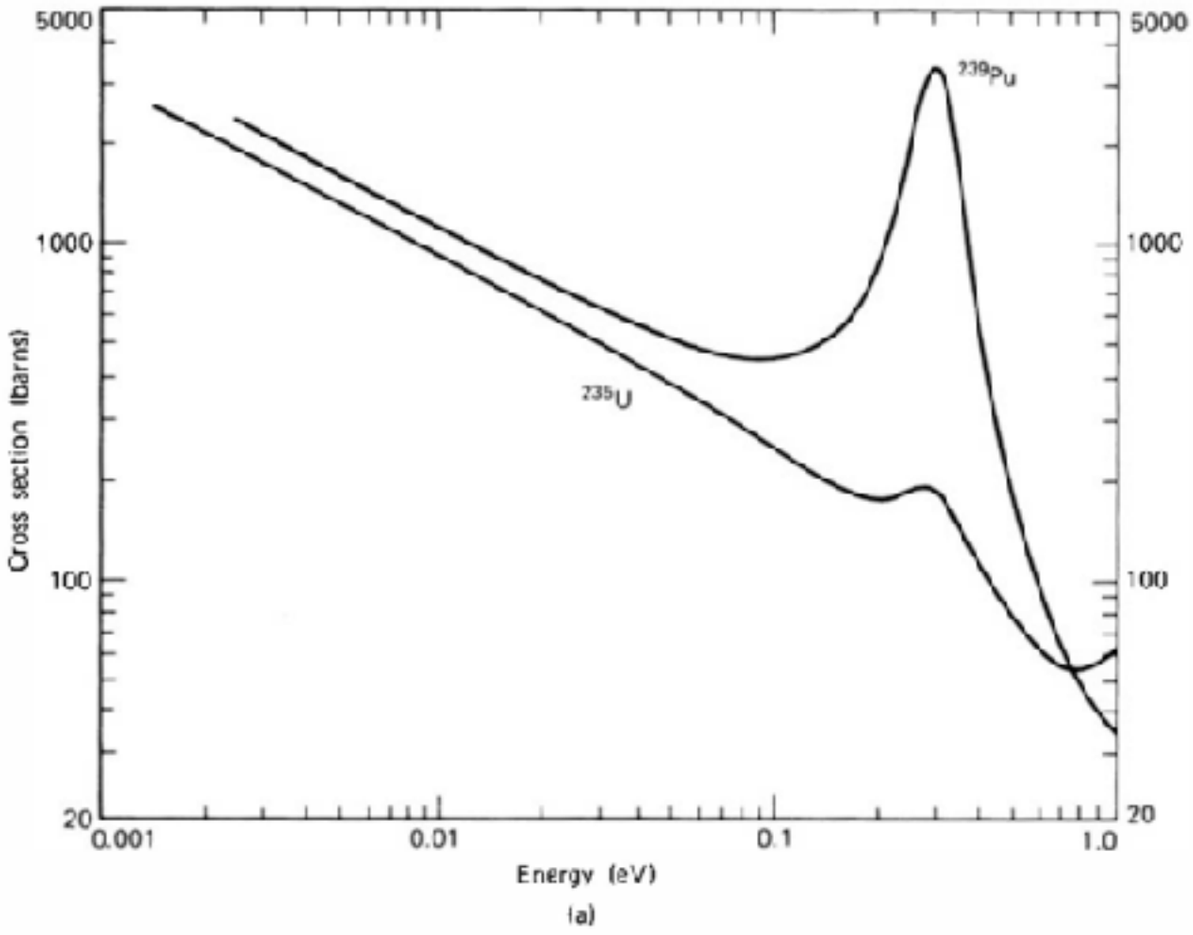

(a)

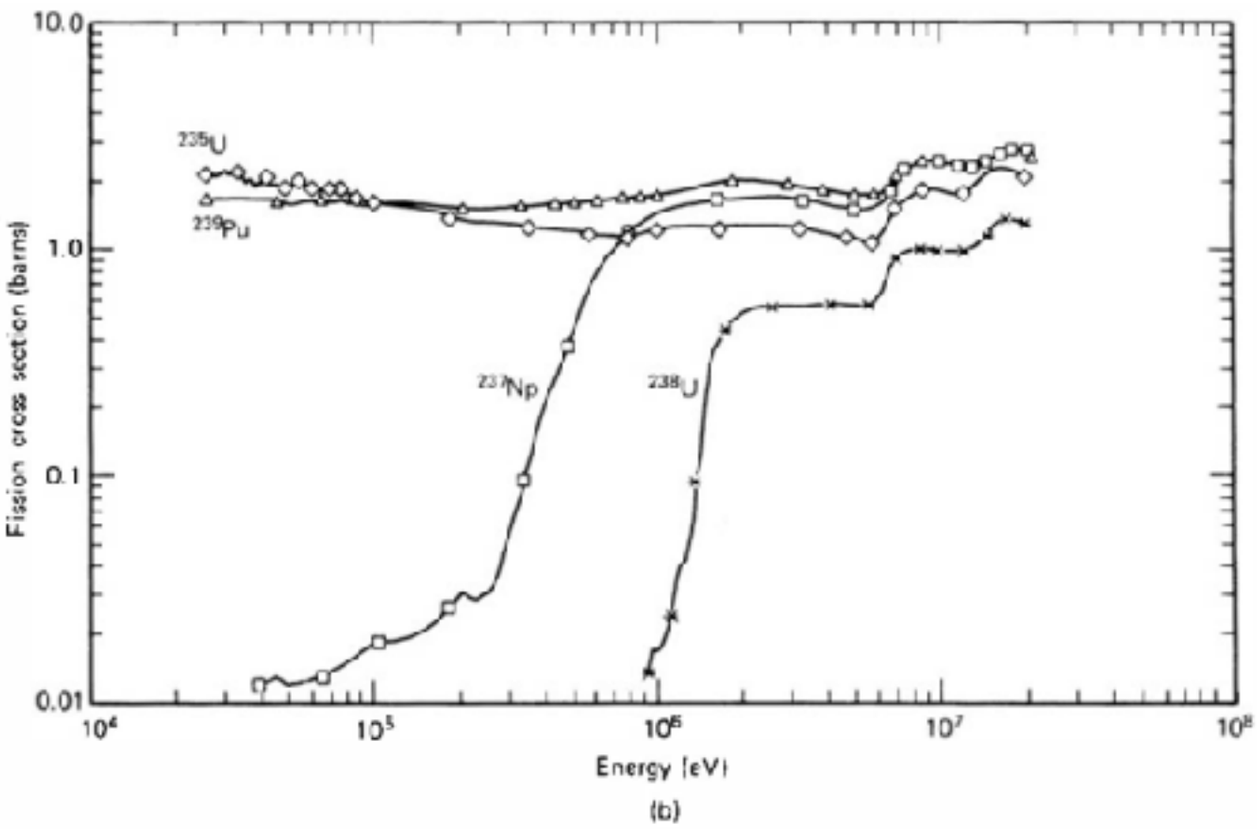

(b)

Neutron Detectors

Detectors based on other conversion reactions

1. Lithium-Containing Slow Neutron Detectors
2. He3 Proportional Counters
3. Fission Counters
4. Silicon Carbide Detectors

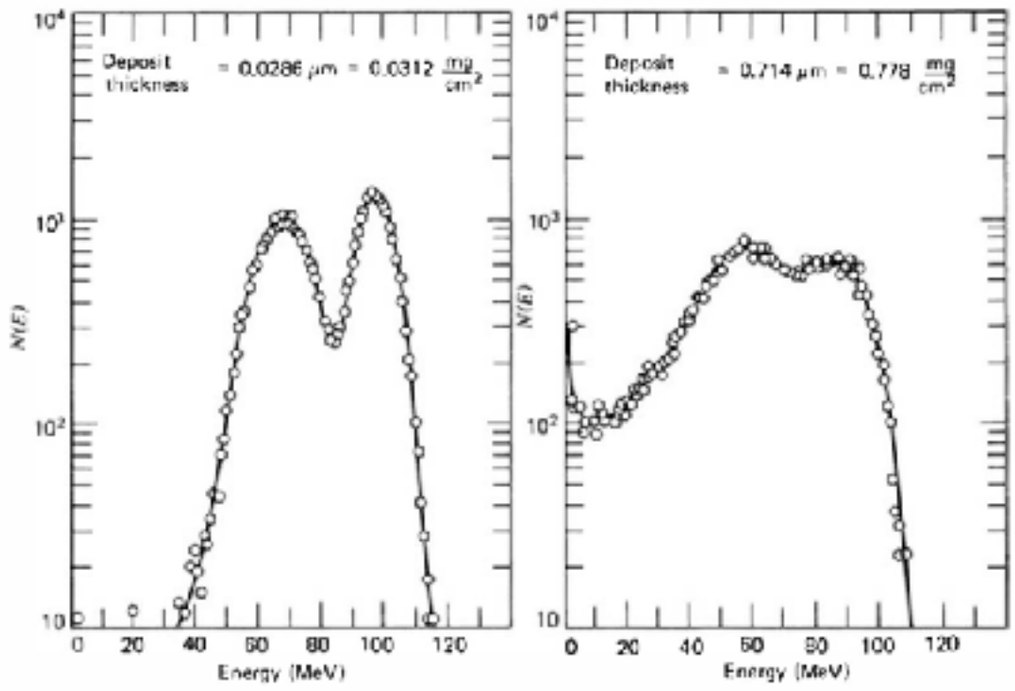

Figure 14.8 Energy spectra of fission fragments emerging from flat UO_2 deposits of two different thicknesses. A 2π detector is assumed that responds to fragments emitted in all directions from one surface of the deposit. (From Kahn et al.[58])

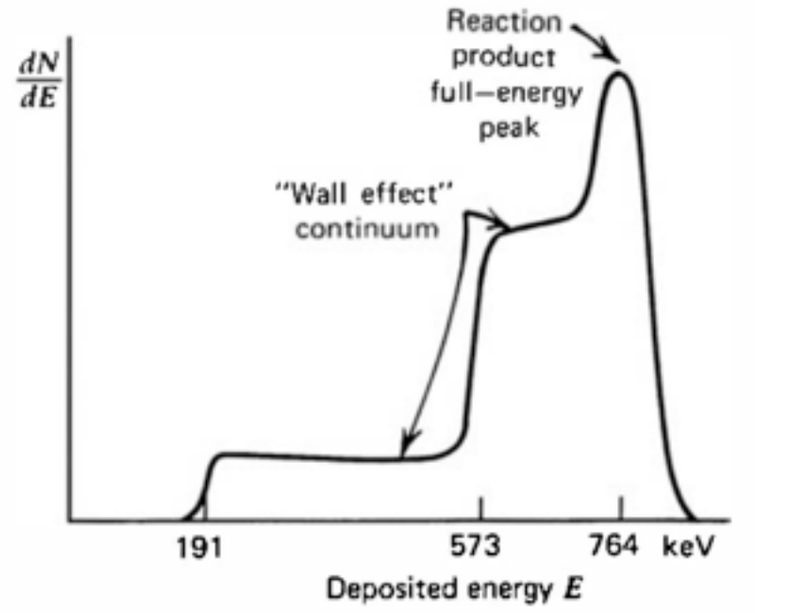

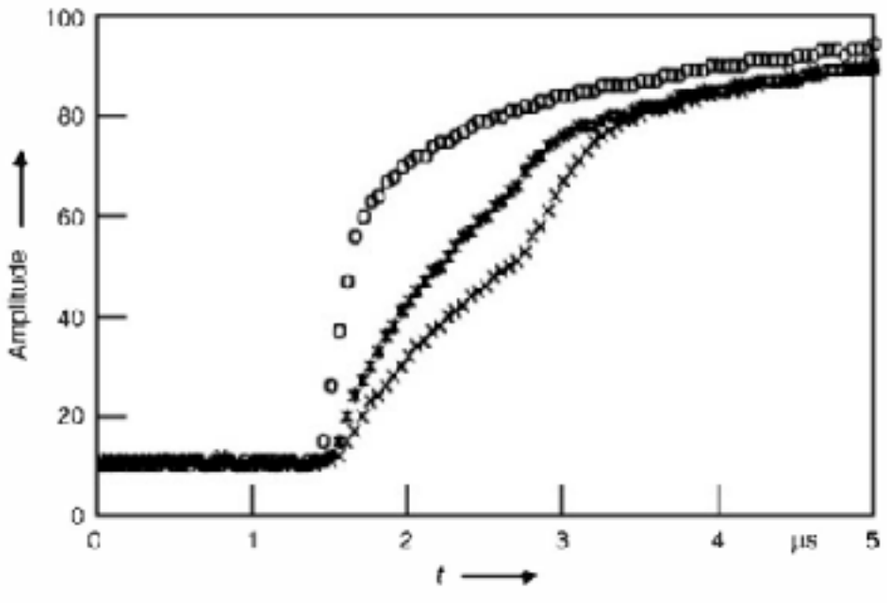

Neutron Detectors

The spherical neutron dosimeter

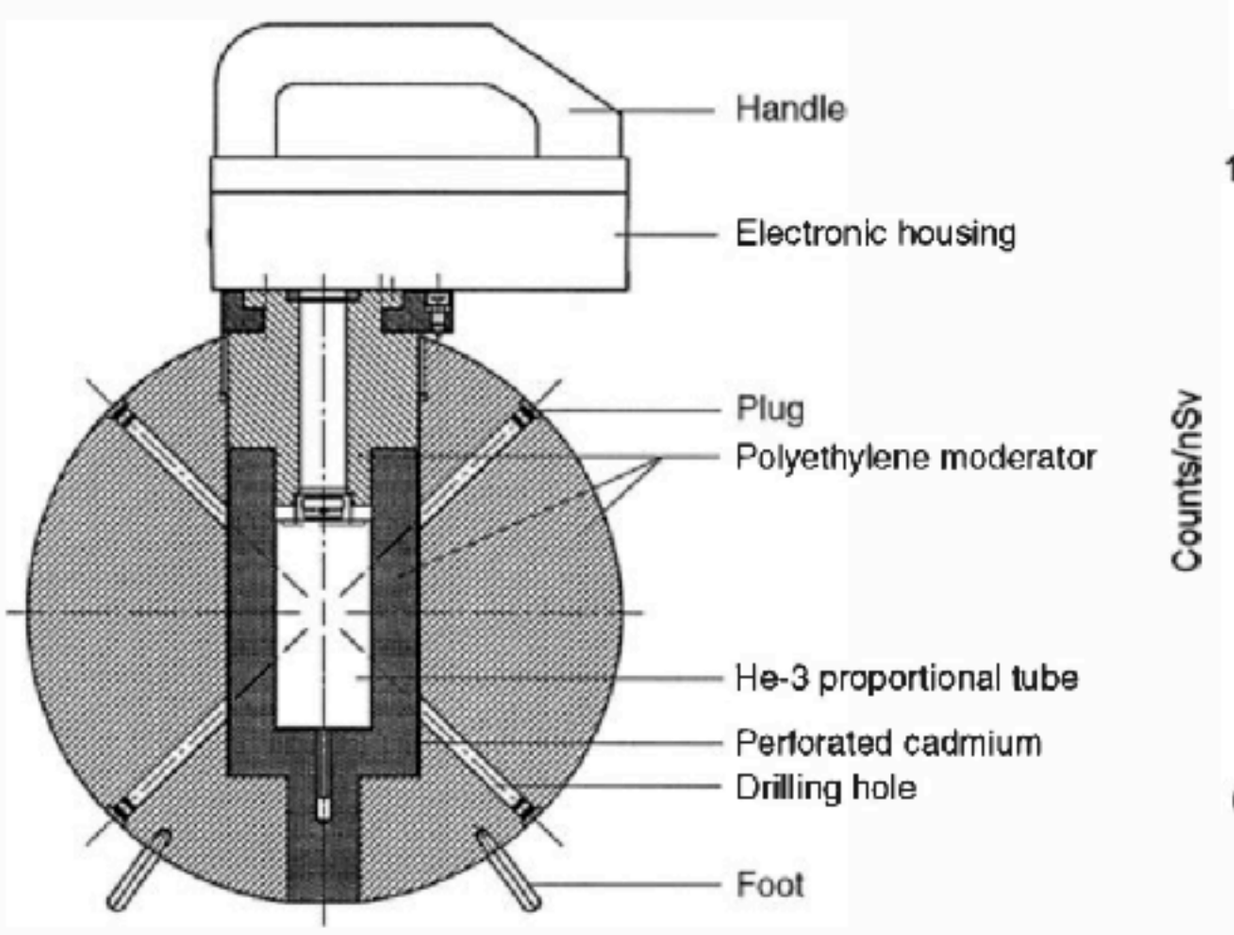

(a)

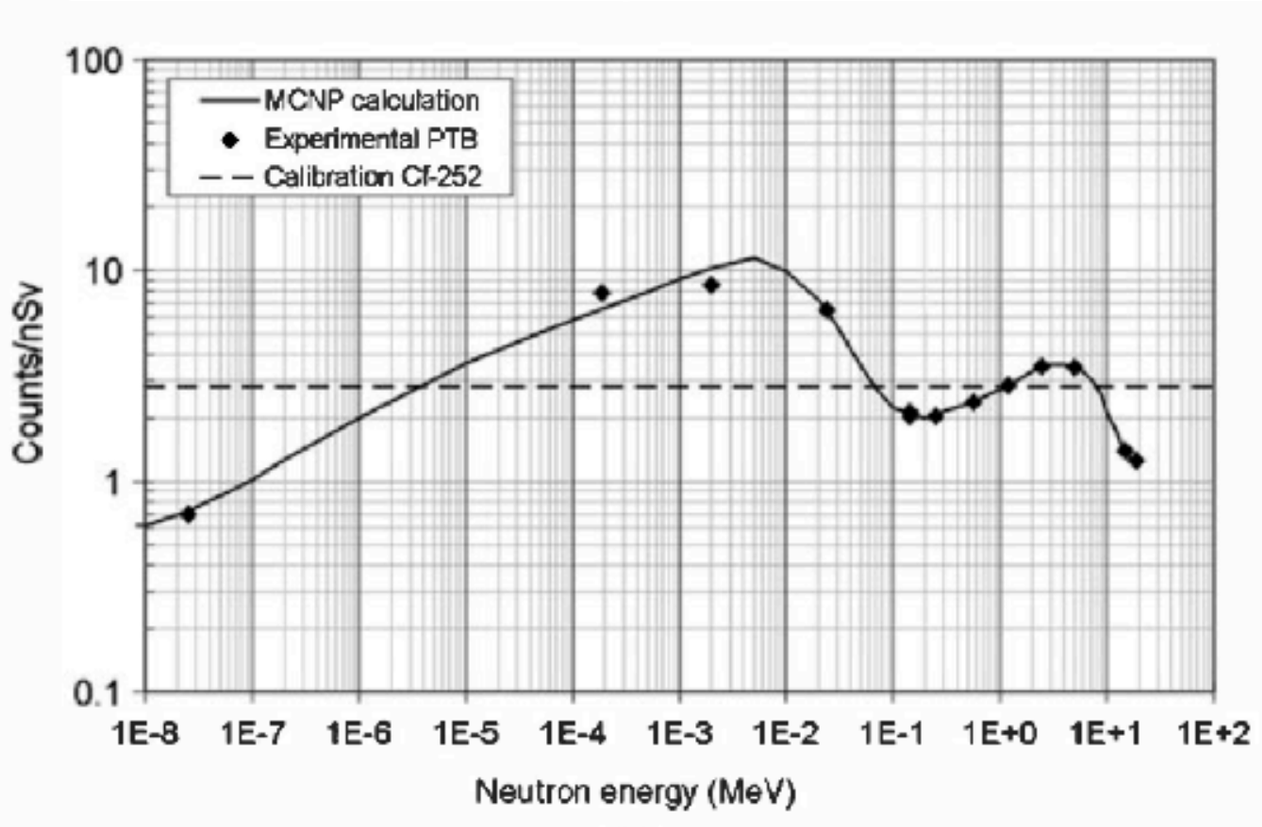

(b)

Neutron Detectors

The long counter

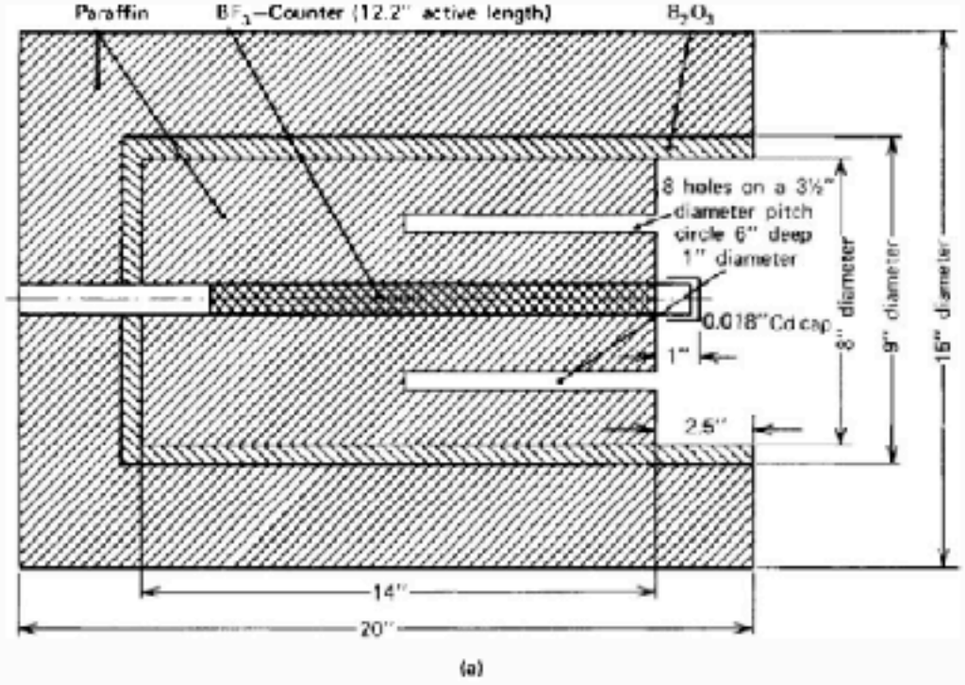

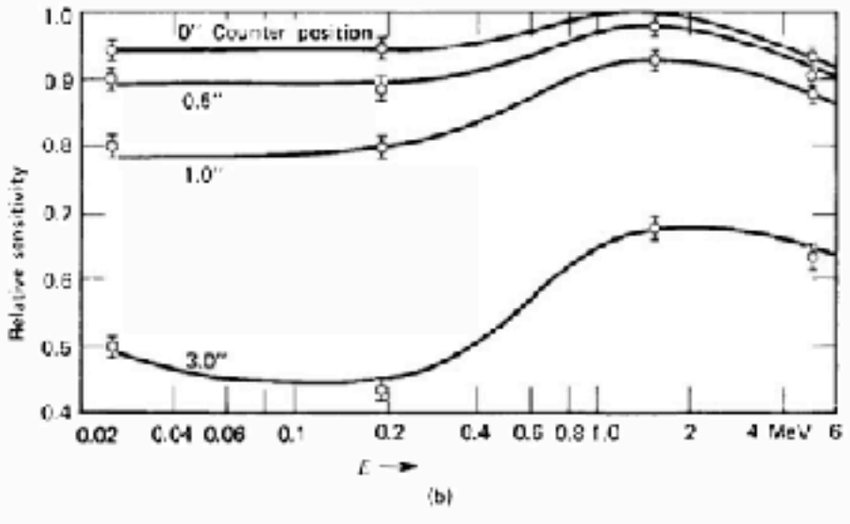

Figure 15.6 (*a*) Cross-section of the long counter developed by McTaggart. (*b*) Relative sensitivity of McTaggart long counter versus neutron energy. The parameter varied for the different curves is the distance the end of the BF_3 tube is shifted in from the front of the moderator face. The flattest response occurs when the tube is flush with the front face. (From K. H. Beckurts and K. Wirtz, *Neutron Physics*. Copyright 1964 by Springer-Verlag, Inc. Used with permission.)

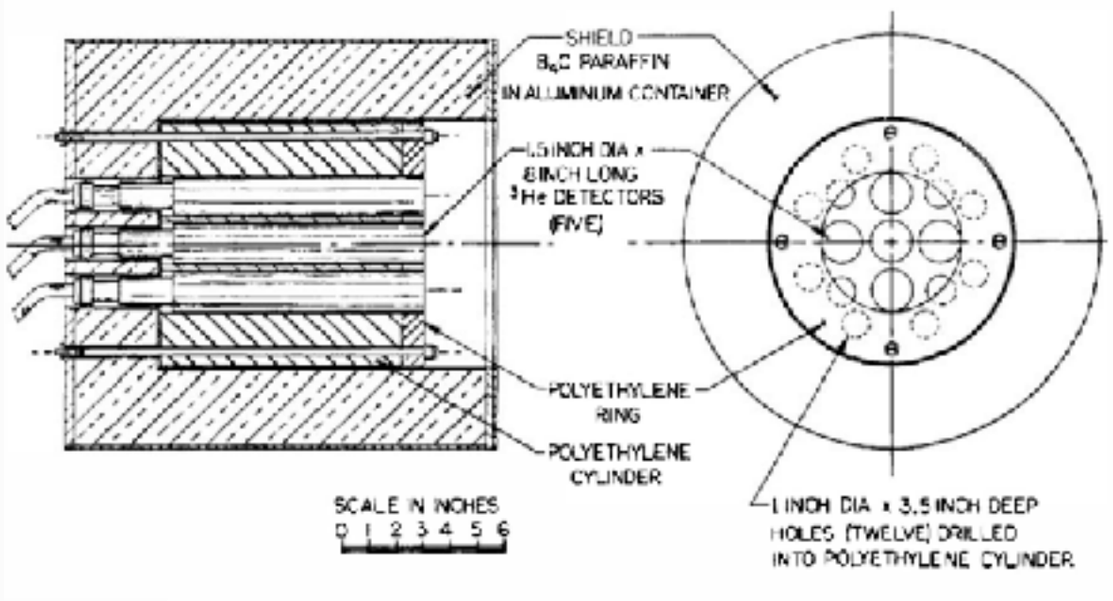

Figure 15.7 A high-efficiency long counter utilizing multiple ^3He tubes. (From East and Walton.[38])

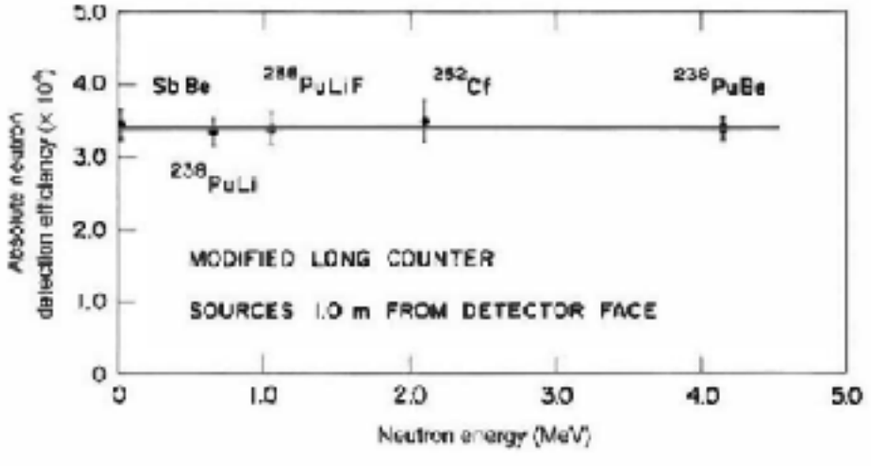

Figure 15.8 Efficiency of the long counter shown in Fig. 15.7 versus the average energy of some neutron sources. The efficiency figures are for a point source located 1 m from the detector face. (From East and Walton.[38])